

**ÇUKUROVA UNIVERSITY
INSTITUTE OF NATURAL AND APPLIED SCIENCES**

MSc THESIS

Ayşe Nur ACAR

**INVESTIGATING THE STRUCTURAL AND PHYSICAL PROPERTIES
FOR AL-7000 SERIES PREPARED ON DIFFERENT TEMPERATURES
AND PRESSURES**

DEPARTMENT OF MECHANICAL ENGINEERING

ADANA, 2014

ÇUKUROVA UNIVERSITY
INSTITUTE OF NATURAL AND APPLIED SCIENCES

SEARCHING OF STRUCTURAL AND PHYSICAL PROPERTIES OF AL-7000 SERIES PREPARED ON DIFFERENT TEMPERATURES AND PRESSURES

Ayşe Nur ACAR

MSc THESIS

DEPARTMENT OF MECHANICAL ENGINEERING

We certify that the thesis titled above was reviewed and approved for the award of degree of the Master of Science by the board of jury on //2014.

.....
Prof. Dr. Abdul Kadir EKŞİ
SUPERVISOR

.....
Assoc. Prof. Dr. Ahmet EKİCİBİL
MEMBER

.....
Asst. Prof. Dr. D. Ali BİRCAN
MEMBER

This MSc Thesis is written at the Department of Institute of Natural And Applied Sciences of Çukurova University.

Registration Number:

Prof. Dr. Mustafa GÖK
Director
Institute of Natural and Applied Sciences

Not: The usage of the presented specific declarations, tables, figures, and photographs either in this thesis or in any other reference without citation is subject to "The law of Arts and Intellectual Products" number of 5846 of Turkish Republic

ABSTRACT

MSc. THESIS

INVESTIGATING THE STRUCTURAL AND PHYSICAL PROPERTIES FOR AL-7000 SERIES PREPARED ON DIFFERENT TEMPERATURES AND PRESSURES

Ayşe Nur ACAR

ÇUKUROVA UNIVERSITY
INSTITUTE OF NATURAL AND APPLIED SCIENCES
DEPARTMENT OF MECHANICAL ENGINEERING

Supervisor : Prof. Dr. Abdul Kadir Ekşi

Year: 2014, Page: 101

Jury : Prof. Dr. Abdul Kadir EKŞİ

: Assoc. Prof. Dr. Ahmet EKİCİBİ

: Asst. Prof. Dr. Durmuş Ali BİRCAN

Thermoelectricity is referred to convert from waste heat generated from many sources such as radiation, automobile exhaust gases to electricity. Via conversion of waste heat to electricity by TEP(Thermoelectric Power) of solids without generating greenhouse gas emissions , thermoelectric generators could be significant role and also TE coolers are used to make refrigerators and other cooling systems.

The main aim of this study is to investigate the structural and thermoelectric properties of Alumix 431 (Al-5.5Zn-2.5Mg-1.5Cu) material which is the Al7xxx series alloy and prepared utilizing the traditional press and sintering process in various pressure and temperatures. Due to the goal, the structural properties of materials were investigated on the optical, SEM figures and hardness testing measurement results; the thermoelectric properties were measured on the PPMS (Physical Property Measurement System) Machine at temperature range 5-300K. The obtained experimental results show that at temperature range of 285-295 K, the maximum electrical resistivity and electrical conductivity were acquired 0.161Ωm and 24.96W/Km respectively, and the Seebeck Coefficient values changed mostly negative sign to positive sign due to dominate from carriers. Also, it was determined as 5.65×10^{-6} of the maximum figure of merit at 300K temperature.

Key Words: Al 7xxx alloys, Alumix 431, Structural and Thermoelectric Properties

ÖZ

YÜKSEK LİSANS TEZİ

FARKLI SICAKLIK VE BASINÇLARDA HAZIRLANAN Al 7_{xxx} SERİLERİNİN YAPISAL VE FİZİKSEL ÖZELLİKLERİNİN ARAŞTIRILMASI

Ayşe Nur ACAR

ÇUKUROVA ÜNİVERSİTESİ FEN BİLİMLERİ ENSTİTÜSÜ MAKİNA MÜHENDİSLİĞİ ANABİLİM DALI

Danışman : Prof. Dr. Abdul Kadir EKŞİ
Yıl: 2014, Sayfa: 101

Jüri : Prof. Dr. Abdul Kadir EKŞİ
: Doç. Dr. Ahmet EKİCİBİL
: Yrd. Doç. Dr. Durmuş Ali BİRCAN

Termoelektriklik, radyasyon, otomobil egzoz gazı gibi kaynaklardan oluşan atık ısıyı elektriğe çevrilmesi olarak tanımlanır. Seragazı gaz emisyonları olmadan, katılardaki TEP(termoelektrik güç) aracılığıyla, atık ısının elektriğe çevrilmesiyle, termoelektrik jeneratörler önemli bir rol oynar ve ayrıca termoelektrik soğutucular, buzdolabı ve diğer soğutucu sistemlerin yapımında kullanılır.

Bu çalışmanın asıl amacı, Al 7_{xxx} serisi alaşımı ve farklı basınç ve sıcaklıklarda geleneksel pres ve sinterleme prosesi sonucu üretilen Alumix 431 alaşımının yapısal ve termoelektrik özellikleri incelemektir. Yapısal özellikler; optik, SEM resimlerinde ve sertlik test ölçüm sonuçlarında incelenmiş, termoelektrik özellikler 5-300K sıcaklık aralığında PPMS(Fiziksel Özellik Ölçüm Sistemi) cihazında ölçülmüştür. Elde edilen deneysel sonuçlar; 285-295K sıcaklık aralığında maksimum elektriksel direnç ve iletkenlik sırasıyla 0.161Ωm and 24.96W/Km olarak elde edildiğini, Seebeck katsayısının taşıyıcılardan dolayı çoğunlukla negatif değerden pozitif değere değiştiğini göstermiştir. Ayrıca, maksimum performans katsayısı 300 K sıcaklıkta 5.65×10^{-6} olarak saptanmıştır.

Anahtar Kelimeler: Al 7_{xxx} alaşımları, Alumix 431, Yapısal ve Termoelektrik Özellikler

ACKNOWLEDGEMENTS

Firstly, my thanks go to my advisor, Prof. Dr. Abdul Kadir EKŞİ for his great guidance, support and encouragement. He has been a great source of motivation, both personal and technical.

I would like to thank Prof. Dr. Bekir Özçelik and Assoc. Dr. Ahmet EKİCİBİL for their continues support, help and encouragements. Knowing and feeling their support during my MSc. thesis helped me a lot.

Also, I would like to thank Prof.Dr. M. Eyyüphan YAKINCI head of Scientific and Technological Center at İnönü Üniversitesi in Malatya,Turkey for opening, helping and supporting to his laboratory for my thesis study

My thanks goes to Res. Assit. Gökhan KIRAT at İnönü University for helping to give my experimental results from PPMS machine.

My heartfelt thanks go to Res.Assits. Erhan FIRAT for helping to learn to graph program and continuous moral support, help and excellent friendship

Many thanks go to my friends Res., Asst. Çağrı UZAY, Hulusi DELİBAŞ Res. Asst. Mete Han BOZTEPE, Res. Asst. Veli ÖZBOLAT, Res. Asst. Sefa YILDIRIM Res. Asst Harun ZONTUL for their moral support, help and excellent friendship.

In addition, I would like to thank all the staff of Department of Mechanical Engineering at Çukurova University

Last but not least, I would like to thank my father Mehmet ACAR, my mother Fatma ACAR, and my sister Ahsen ACAR for their patience and trust.

CONTENTS	PAGE
ABSTRACT	I
ÖZ.....	II
ACKNOWLEDGEMENTS	III
CONTENTS	IV
LIST OF TABLES	VI
LIST OF FIGURES	VIII
LIST OF ABBREVIATIONS	XII
1. INTRODUCTION	1
1.1. The Basic Principle of Thermoelectricity	1
1.1.1. The Electrical Conductivity	4
1.1.2. The Electrical Resistivity	5
1.1.3. The Thermal Conductivity	6
1.1.4. The Seebeck Coefficient	7
1.1.5. The Figure of Merit.....	8
1.2. The Wiedemann-Franz Law.....	11
1.3. The Hall Effect	15
1.4. Thermoelectric Materials And Manufacturing Methods.....	17
2. PREVIOUS STUDY	21
2.1. The Thermoelectric Properties of Materials Produced By Powder Metallurgy	21
2.2. Previous Studies on Thermoelectric Properties of Al-Zn Mg-Cu Materials... 31	31
2.2.1. Searching of the Electrical –Thermal Conductivities of Al-7xxx Series Alloys	37
2.2.2. Searching of the Electrical Resistivity of Al-7xxx Series Alloys	40
3. MATERIAL AND METHOD	45
3.1. Material	45
3.2. Method	46
3.2.1. Manufacturing Methods of Specimens	46
3.2.2. Characterization Methods of Specimens of Alumix (431) Specimens .	48

3.2.2.1. Optical Microscope and Scanning Electron Microscope (SEM) Characterization Methods	48
3.2.2.2. Density Measurements of Alumix 431 Specimens	49
3.2.2.3. Measurement of Thermal-Transport Properties Of Alumix 431 Specimens Via The Physical Measurement System (PPMS)	50
4. RESULTS AND DISCUSSIONS	59
4.1. Analysis of Optical Micrographic Figures of Alumix 431 for 1, 2, 3, 4, 5, 6 Specimens	60
4.2. Analysis of SEM Figures of Alumix 431 for 1, 2, 3, 4, 5, 6 Specimens.....	63
4.3. Density Measurements of Alumix 431 Specimens	65
4.4. Analysis of Electrical Resistivity of Alumix 431 for 1, 2, 3, 4, 5, 6 Specimens	67
4.5. Analysis of Thermal Conductivity Results of Alumix 431 for 1, 2, 3, 4, 5, 6 Specimens	72
4.6. Analysis of Seebeck Coefficient Results of Alumix 431 for 1, 2, 3, 4,5, 6 Specimens	78
4.7. Analysis of Figure Of Merits Results of Alumix 431 for 1, 2, 3, 4,5, 6 Specimens	83
5. CONCLUSION	87
REFERENCES.....	88
CURRICULUM VITAE	100

LIST OF TABLES	PAGE
Table 1.1. Comparison of Thermoelectric Properties of metals, semiconductors and insulators	9
Table 1.2. Examples of THE Required device ZT	14
Table 3.1. Typical chemical composition and physical characteristics of Alumix 431 Material.....	45
Table 3.2. System Requirements for the Thermal Transport System	56
Table 3.3. Thermal Transport System Parameters.....	56

LIST OF FIGURES	PAGE
Figure 1.1. Various energy conversion applications of thermoelectric materials.....	2
Figure 1.2. For different values of ZT, thermoelectric conversion efficiencies as a function of temperature differentials	3
Figure 1.3. An illustration of TE effect.....	4
Figure 1.4. Bar chart of room temperature electrical conductivity ranges for metals ceramics, polymers and semiconducting materials (Callister and Retwisch, 2012).....	5
Figure 1.5. Schematic representation pf the apparatus used to measure electrical resistivity(Callister and Retwisch, 2012)	6
Figure 1.6. Seebeck coefficient S , electrical conductivity σ , $S^2 \sigma$ and electronic (κ_e) and lattice (κ_l) thermal conductivity as a function of free-charge carrier concentration n (Zheng et al., 2008).....	10
Figure 1.7. A Hall Voltage generated from current flow in the semiconductor material(Rohm).....	16
Figure 1.8. Temperature dependent on the Figure Of merit (ZT) curves of p-type and n-type materials(Snyder and Toberer,2008)	18
Figure 2.1. Schematic of the powder metallurgy processing steps.	21
Figure 2.2. Temperature dependences of (a) the electrical conductivity,(b) the Seebeck coefficient (c) the thermal conductivity (d) ZT value. of the $\text{Bi}_{0.5}\text{Sb}_{1.5}\text{Te}_3$ bulk samples (Shen et al., 2011).....	23
Figure 2.3. x (molar fraction) dependence of the Electrical resistivity and thermal conductivity of $(\text{Bi}_2\text{Te}_3)_x(\text{Sb}_2\text{Te}_3)_{1-x}$ (Yang et al., 2000).	25
Figure. 2.4. x (molar fraction) dependence of figures of merit for $(\text{Bi}_2\text{Te}_3)_x(\text{Sb}_2\text{Te}_3)_{1-x}$ produced via different methods.(Yang et al., 2000)....	25
Figure. 2.5. Fundamental procedure for preparing the high performance thermoelectric materials by Powder Metallurgy (Katsuyama et al., 2004)	26

Figure. 2.6. Ideal microscopic structure for the low κ ph. (Katsuyama et al., 2004).	27
Figure 2.7. (a)A sketch of the break-down from micron to millimicron throughout the CG process. (b) Milling time related to average particle size of the CG samples as compared with that of the HEBM sample.....	27
Figure 2.8. Temperature based on (a) thermopower S and (b) resistivity ρ for the nanoparticle compacts and single crystals (Wang and Fan, 2011).	28
Figure 2.9. Temperature dependences of thermal conductivity κ for the nanoparticle compacts and single crystals (Wang and Fan, 2011).	29
Figure. 2.10. Temperature-dependence of (a)Seebeck coefficient (b) electrical conductivity (c) thermal conductivity for PbTe samples prepared by different cryomilling times and sintered at 573 K (Kuo et al., 2011)	30
Figure 2.11. Variation of conductivity after different RRA treatments: (a) Retrogression; (b) Pre-aging; (c) Re-aging (Feng et al., 2006)	36
Figure 2.12. Evolution of ageing temperature on hardness (a) and conductivity (b) of studied alloy (Zang et al., 2012).	38
Figure 2.13. Changing variation of electrical conductivity during retrogression (open diamonds) and reaging (solid diamonds) treatments of the alloy (Liu et al., 2014).	39
Figure 2.14. Isothermal pre-aging curves of the relative resistivity ρ_e at various temperatures for samples of 7012 alloy quenched at 470 °C.	40
Figure 2.15. Changing of the resistivity throughout isothermal holdings then interrupted quenching from the solutionizing temperature (Archambault and Godard, 2000).	42
Figure 2.16. Temperature based on precipitation kinetics obtained between 475 and 200°C by DSC and resistivity measurement for the 10°C/mn cooling (Archambault and Godard, 2000).	43
Figure 3.1. Compacted aluminium alloy used in this study.	47

Figure 3.2.	The cracked samples for measuring thermoelectric properties	47
Figure 3.3.	Specimen preparation steps for Optical Microscopy and SEM (Dilek, 2006).....	48
Figure 3.5.	The PPMS of Model 6000 PPMS Machine.....	50
Figure 3.6.	The Model 6000 Controller of Model 6000 PPMS Machine.	51
Figure 3.7.	The NMR Apparatus and PPMS head of Model 6000 PPMS machine.....	51
Figure 3.8.	Samples prepared to examine the thermal-transport properties.....	52
Figure 3.9.	Sample-holder of PPMS machine.....	52
Figure 3.10.	The upper part of the NMR probe head (Gafner, 2006).	53
Figure 3.11.	The bottom part of NMR probe head (Gafner, 2006).....	53
Figure 3.12.	The NMR probe head (Gafner, 2006).....	54
Figure 3.13.	The sample holder, plateau, thermal sensor and noise-blocking capacitor (Gafner, 2006).	55
Figure 4.1.	Optical microscope image of alumix (431) sample (50 μ m).....	61
Figure 4.2.	Optical microscope image of alumix (431) sample (20 μ m).....	61
Figure 4.3.	Optical microscope image of alumix (431) sample with transactions (10 μ m).	62
Figure 4.4.	Optical microscope image of alumix (431) sample with materials (20 μ m).	62
Figure 4.5.	SEM image of Alumix (431) sample prepared under the 180MPa and 80° conditions(10 μ m).	64
Figure 4.6.	SEM image of Alumix (431) sample prepared under the 180MPa and 80° C conditions (20 μ m).....	64
Figure 4.7.	The gren density(g/cm-3) changes of Alumix 431 samples related to compressionpressure(MPa)(iynen,2009).....	65
Figure 4.8.	Relationship between the compaction pressure and green strength of the samples Prepared in three various compaction temperatures (İynen, 2009).....	66
Figure 4.9.	The Resistivity –Temperature graph of alumix(431) 1	67
Figure4.10.	The Resistivity –Temperature graph of alumix(431) 3	69

Figure 4.11. The Resistivity –Temperature graph of alumix(431) 4	69
Figure 4.12. The Resistivity –Temperature graph of alumix(431) 6	70
Figure 4.13. The Resistivity –Temperature graph of alumix(431) 2	70
Figure 4.14. The Resistivity –Temperature graph of alumix(431) 5	71
Figure 4.15. The thermal conductivity –Temperature graph of alumix(431) 5	74
Figure 4.16. The thermal conductivity –Temperature graph of alumix(431) 6	75
Figure 4.17. The Thermal Conductivity –Temperature graph of alumix(431) 2 ..	76
Figure 4.18. The Thermal Conductivity –Temperature graph of alumix(431) 3 ...	76
Figure 4.19. The Thermal Conductivity –Temperature graph of alumix(431) 4 ...	77
Figure 4.20. The Thermal Conductivity –Temperature graph of alumix(431) 1 ...	77
Figure 4.21. The Seebeck Coefficient –Temperature graph of alumix(431) 1	78
Figure 4.22. The Seebeck Coefficient –Temperature graph of alumix(431) 2	79
Figure 4.23. The Seebeck Coefficient –Temperature graph of alumix(431) 3	80
Figure 4.24. The Seebeck Coefficient –Temperature graph of alumix(431) 6	80
Figure 4.25. The Seebeck Coefficient –Temperature graph of alumix(431) 4	81
Figure 4.26. The Seebeck Coefficient –Temperature graph of alumix(431) 5	81
Figure 4.27. The ZT –Temperature graph of alumix(431) 3.....	83
Figure 4.28. The ZT –Temperature graph of alumix(431) 3.....	84
Figure 4.29. The ZT –Temperature graph of alumix(431) 3.....	84
Figure 4.30. The ZT –Temperature graph of alumix(431) 2.....	85
Figure 4.31. The ZT –Temperature graph of alumix(431) 4.....	86
Figure 4.32. The ZT –Temperature graph of alumix(431) 6.....	86

LIST OF ABBREVIATIONS

S	:	Seebeck coefficient
α	:	Seebeck coefficient
ΔV	:	Variance of thermoelectric voltage
ΔT	:	Variation of temperature range
T	:	Temperature
ρ	:	Electrical resistivity
σ	:	Electrical conductivity
κ_{total}	:	Total thermal conductivity
κ_e	:	Electronic thermal contribution
κ_l	:	Lattice thermal contribution
κ_{bipolar}	:	Bipolar thermal contribution
ZT	:	Dimensionless figure of merit
Z	:	Figure of merit
P	:	Thermoelectric power
k_B	:	Botzmann constant
e	:	Charge of electron
n	:	Carrier concentration
μ	:	Charge carrier mobility
L	:	Lorenz factor
L_{ph}	:	Phonon mean free path
v	:	Electron velocity
v_F	:	Fermi velocity
v_S	:	Sound velocity
c_v	:	Heat capacity at constant value
Λ	:	Electron mean free path
r	:	Scattering factor
m	:	Carrier effective mass
E_F	:	Fermi energy
E	:	Carrier energy

l	:	Free path length of the scattering
s	:	Scattering mechanism constant
μ_H	:	Temperature dependence of the electron Hall mobility
R_H	:	Hall coefficient
$\rho_{M(t)}$:	The resistivity of the matrix phase
ρ_i	:	The initial resistivity value after quenching
ρ_s	:	The maximum resistivity value
$\rho(t)$:	The measured instantaneous resistivity value
ρ_o	:	The resistivity of the alloy
$\sigma_{M(t)}$:	The conductivity of the matrix phase
$\chi_{Zn(t)}$:	The concentrations of the Zn Element in the matrix phase
$\chi_{Mg(t)}$:	The concentrations of the Mg Element in the matrix phase
t	:	Ageing time
t_c	:	Diffusion condition

1. INTRODUCTION

Powder Metallurgy is a method by which fine powdered materials are mixed, pressed into a desired shape (compacted) and then sintered in a controlled atmosphere to bond the conducting particles and to constitute wanted particles (Black and Kosher, 2008).

Powder metallurgy is related to manufacturing of metal powders and conversion of them to useful shape (Ramakrishnan, 1983). In this method, mechanical and thermoelectric properties are exceedingly related to the microstructures of materials and microstructure formation. In this method, it is acquired an improved mechanical property such as high strength and hardness (Lim et al., 2006) (Yang et al., 2009). Manufacturing of materials via powder metallurgy methods also achieves the increase of figure of merit because of grain purification as well as higher compressive strength (Bhuiyan, 2011).

1.1. The Basic Principle Of Thermoelectricity

Conversion of different types of ‘subgrade’ heat such as industrial waste heat, the vehicle exhaust gas heat, solar and geothermal energies is happening more significant owing to environmental interests (Xu et al., 2012; Rubi et al., 2014). Thermoelectric materials and devices are suitable for this conversion. These materials and devices convert waste heat into electricity via the thermoelectric power of solids (Tritt et al., 2006). Thermoelectric generators can be applied to transforming heat produced by sources such as exhaust gases to electricity using the Seebeck effect. This effect is the transformation of temperature varied directly electricity. As a generator is operated, one side of the tool is heated to a temperature greater than the other side, then all a different in a voltage will increase between the two sides. These thermoelectric generators are also defined Seebeck generators. In contrast thermoelectric coolers can be utilized to make refrigerators and other cooling systems. These devices operate using the Peltier effect and produce heat flow

between linking of two different types of material. These coolers are also defined Peltier coolers. The Seebeck and Peltier effects will be explained below.

Owing to their reliability, operation the unattended in hostile environments and environmental friendly, thermoelectric materials and devices are used in infrared sensors and satellites. The disadvantage of these materials is the operating of low efficiency limited applications.

In the below fig. 1.1 presents that the various energy applications of thermoelectric materials.

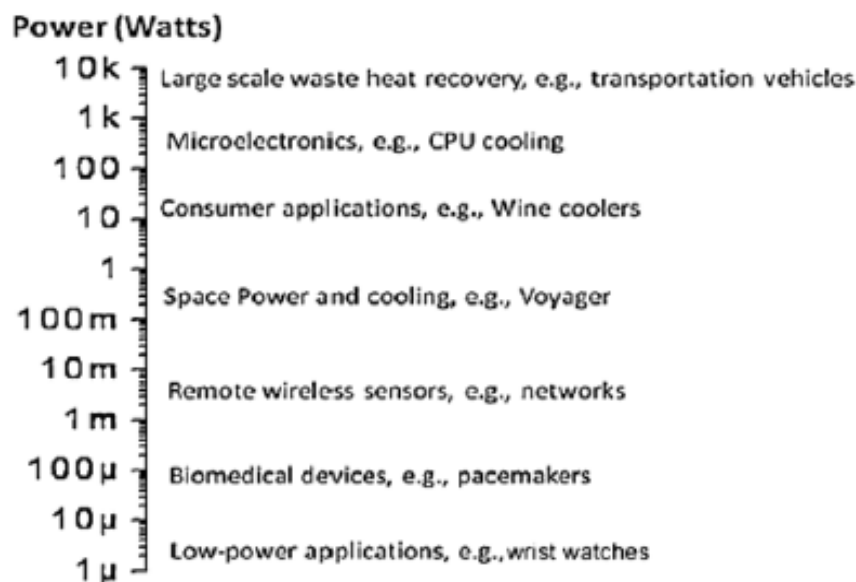


Figure. 1.1. Various energy conversion applications of thermoelectric materials (Radousky and Liang,2012)

In waste heat recovery, There are issues in the way of automobiles or other transportation vehicles, besides utilize in oil refineries while other issues consist of heat distribution e.g. in microelectronics- where leakage currents in transistors exponentially increase with temperature. These are based on the both energy conservation and generation. Spite of this situation, because of their low efficacy, the utilization of thermoelectric materials is not as wide as hoped. Via thermoelectric and thermionic materials, The energy conversion between thermal and electrical forms is to be more efficient in materials consisting materials and

successful application of nanostructured thermoelectrics, the materials are hoped to applied a wide range of implementations.

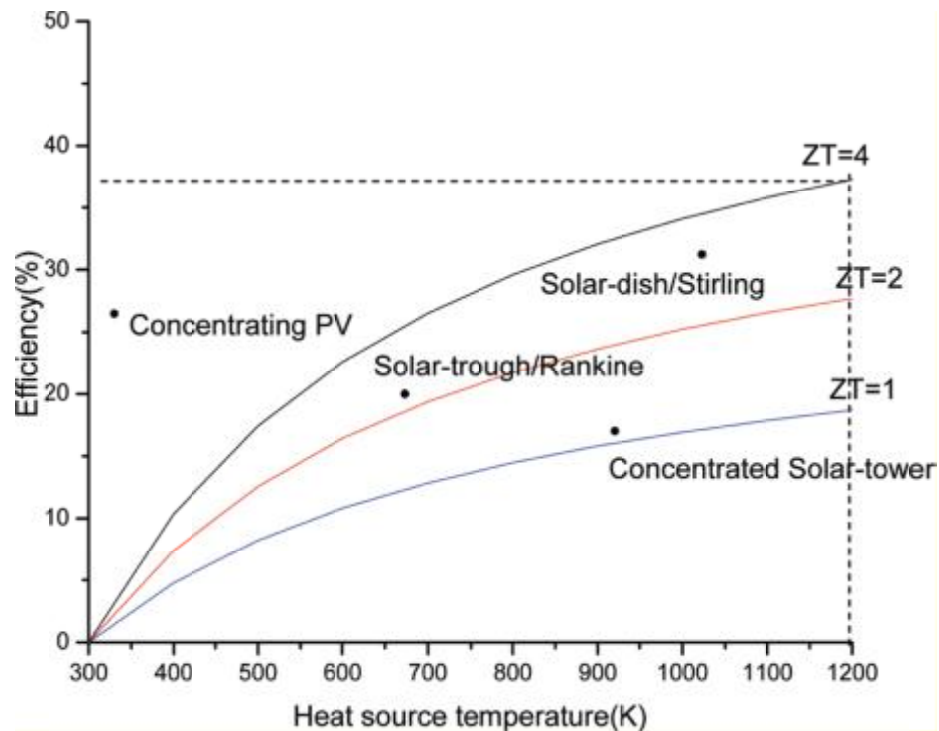


Figure.1.2. For different values of ZT , thermoelectric conversion efficiencies related to function of temperature differentials (Xie and Gruen, 2010)

Figure 1.2. indicates the manner in which conversion efficiencies of thermoelectric materials related to ZT when plotted as a function of heat source temperatures, under the assumption that the temperature of the cold side is maintained at 300 K. The conversion efficiency of thermoelectric materials must be 30%-40% in order to compete with state-of-the-art solar-thermal technologies related to on the electromagnetic induction method. Between the hot and cold ends of a thermopile, this needs $ZT = 4$ and a large temperature differential. (Xie and Gruen, 2010).

There are three fundamental effects of thermoelectric materials: the Seebeck effect, the Peltier effect, the Thomson effect. As described above Seebeck effect which discovered by Johann Seebeck in 1821 defines the phenomena that a conductor creates a voltage as related to temperature variance.

$$V = \alpha \Delta T \quad \rightarrow \quad \alpha = S = \frac{\Delta V}{\Delta T} \quad (1.1.)$$

Where S, α is defined to Seebeck coefficient, ΔV and ΔT is variance of thermoelectric voltage and temperature range respectively.

The Peltier effect refers to the temperature variations induced by voltage gradience. Due to this property of Peltier effect, it is reversal effect of Seebeck effect. The Thomson effect depends on both the reversible thermal gradient and electric field in a uniform conductor.(Figure 1.3.)

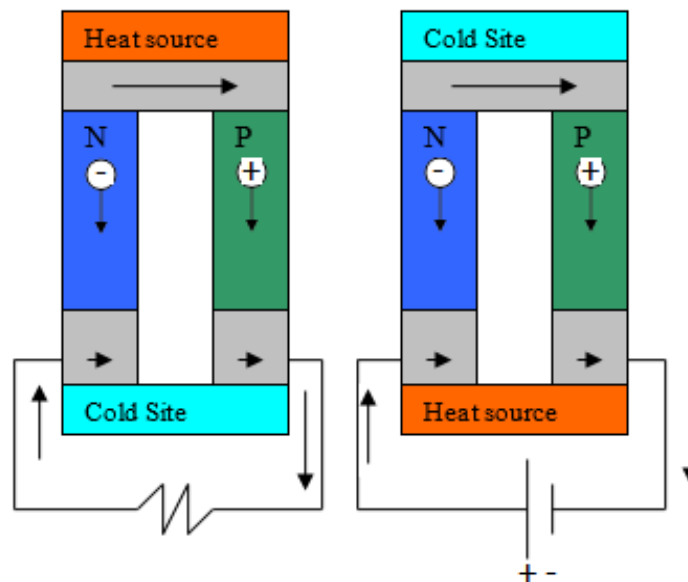


Figure 1.3. An illustration of TE effect

1.1.1. The Electrical Conductivity

Electrical conductivity is utilized to quantify the electrical character of material. It is simply the reciprocal relationship between electrical conductivity and resistivity;

$$\sigma = \frac{1}{\rho} \quad (1.2.)$$

and is indicative of the simple with which a material is capable of conducting an electric current. The units for σ are reciprocal ohm meters (Ωm) or mho/m.

Solid materials show an surprising range of electrical conductivities. Materials are good conductivities, typically having conductivities on the order of $10^7(\Omega\text{m})^{-1}$, insulators have very low conductivities ranging between 10^{-10} and $10^{-12}(\Omega\text{m})^{-1}$. Materials with intermediate conductivities, usually from 10^{-6} to $10^4(\Omega\text{m})^{-1}$ are referred as semiconductors (Callister and Retwisch, 2012).

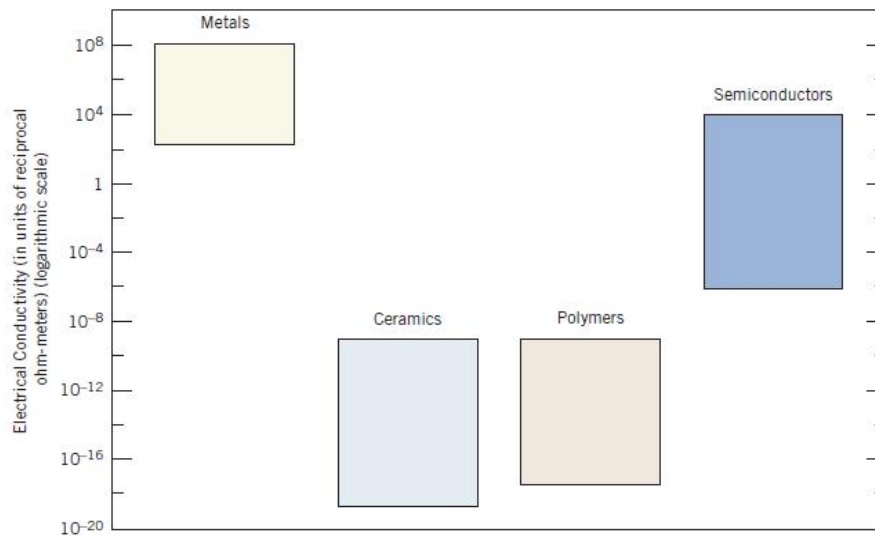


Figure 1.4 Bar chart of room temperature electrical conductivity ranges for metals, ceramics, polymers, and semiconducting materials (Callister and Retwisch, 2012)

1.1.2. Electrical Resistivity

One of the most significant electrical characteristics of a solid material is the simple with which it transmits an electric current. Ohm's law depends on the current I - or time rate of charge passage to the applied voltage $V(V=IR$, where R is the resistance of the material through which the current is passing.) R is affected by specimen configuration and for many materials in independent of current (Callister and Retwisch, 2012) .

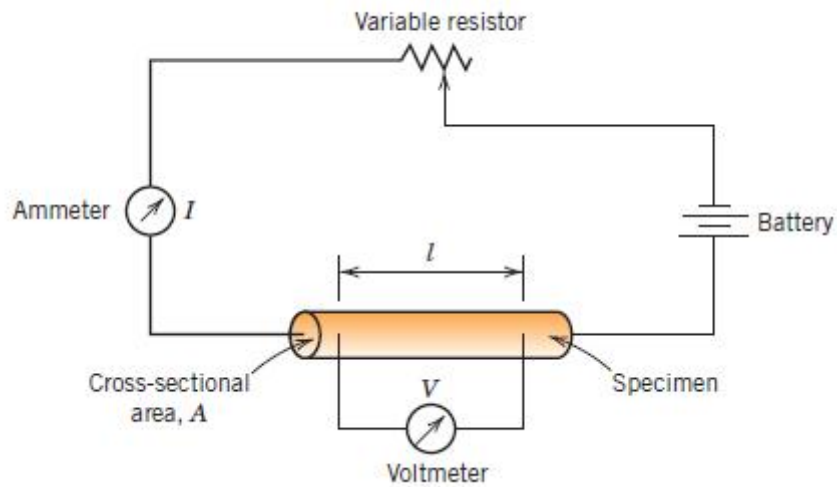


Figure 1.5. Schematic representation of the apparatus used to measure electrical resistivity (Callister and Retwisch, 2012).

The electrical resistivity, ρ , is depended on resistance specimen cross sectional area (A) and distance between measuring points and independent of specimen geometry but according to through the expression.

$$\rho = R \frac{A}{l} \quad (1.3.)$$

A , l are stated the cross-sectional area perpendicular to the direction of the current, the distance between the two points at which the voltage is measured, respectively. The units for ρ are ohm.meters ($\Omega.m$) (Callister and Retwisch, 2012).

1.1.3. Thermal Conductivity

Thermal conduction is the transport of thermal energy from high to low temperature regions of a material. The property characterizes the ability of a material to transfer heat (Callister and Retwisch, 2012).

$$q = k \frac{dT}{dx} \quad (1.4.)$$

Where q is heat flux per unit time per unit area (area being taken as that perpendicular to the flow chart), k is the thermal conductivity, dT/dx is the temperature gradient through the conductivity medium.

In solid materials, heat is transisted by both lattice vibration waves (phonons) and free electrons. A thermal conductivity is related with each of these mechanisms, and the total conductivity is the sum of the two contributions, or

$$\kappa = \kappa_e + \kappa_l \quad (1.5.)$$

κ_e and κ_l is stated the lattice vibration and electron thermal conductivities, respectively.

The κ_l contribution occurs from a net movement of phonons from high- to low-temperature regions of a body across which a temperature gradient exists. A gain in kinetic energy is clarified to the free electrons in a hot region of the specimen. Then, they migrate to colder areas. The areas are to where transferred of some of this kinetic energy to the atoms (as vibrational energy) as a result of collisions with phonons or other imperfections in the crystal (Callister and Retwisch, 2012).

For relatively pure metals, they have high thermal conductivity because of the large numbers of free electrons and the efficiency with which these electrons transport thermal energy. On the contrary, ceramics and polymers have low thermal conductivity due to the low free-electron concentrations and predominating phonon conduction (Callister and Retwisch, 2012).

1.1.4. Seebeck Coefficient

Owing to conduction, the transfer of heat energy by microscopic diffusion and collisions of particles or quasi-particles within a body because of due to a temperature gradient, heat flows through a solid material. The heat flux is the rate of heat transfer per unit area through a material, in order words, is directly proportional to the temperature gradient. There are different mechanisms which can transfer heat in a material. The first mechanism is occurred through vibrations of the internal

structure of the material, such as vibrations of the crystal lattices or individual atoms, while the other mechanism is occurred through electron transport (Kim et al., 2012).

In a material having electrically conductive, electrons can carry heat from one end to another giving rise to the Seebeck effect. To stop the drag and continue equilibrium, a force is required. This force takes the form of a voltage potential that develops to stop the drag of electrons. The magnitude of this Seebeck effect is characterized by the Seebeck Coefficient. The coefficient has units of voltage per unit temperature generally stated in microvolts per Kelvin (Kim et al., 2012).

The magnitude of this effect is quantified by the Seebeck coefficient. Seebeck Coefficients have units of voltage per unit temperature, usually expressed in microvolts per Kelvin, and can be calculated using Equation 2:

$$S = \Delta V / \Delta T \quad (1.6.)$$

Where ΔV is stated the voltage difference between the hot and cold sides of a thermoelectric material and ΔT is the change in temperature between the sides. Related to whether the mobile charges are holes or electrons, they can have a positive or negative value, therefore giving the Seebeck coefficient a positive or negative value (Kim et al., 2012).

1.1.5 The Figure Of Merit

A thermoelectric tool includes of an element put between a heat source i.e. with regard to waste heat generation and the heat sink. From the source to the sink, heat transfer is through the carriers (electrons) motion or through the lattice.

The carrier transport occurs in a development of a potential difference. This potential difference (ΔV) is referred as the Seebeck voltage. As the showed on the formula of S above, the Seebeck coefficient is the ratio of Seebeck voltage (ΔV) to the temperature variance ΔT .

The combination of three effects (Seebeck effect, Peltier effect and Thomson effect) is stated to Kelvin Relationships. This feature represent properties of three

effects thus it is called as figure of merit by researchers.(Du and Wen, 2011) The efficiency of thermoelectric devices is characterized by the dimensionless figure of merit (ZT) of thermoelectric materials.

$$ZT = \frac{S^2 T}{\rho \kappa_{total}} = \frac{S^2 \alpha T}{\kappa} = \frac{\alpha^2 \sigma}{\kappa} \quad (1.7.)$$

In above equation (3.2);T, ρ , κ_{Total} , are referred to the average operating temperature between the hot and cold sides, electrical resistivity, total thermal conductivity respectively.

Table 1.1. shows comparison of thermoelectric properties of metals, semiconductors and insulators at 300K.

Table 1.1. Comparison of Thermoelectric Properties of metals, semiconductors and insulators (Zheng, 2008)

Property	Metals	Semiconductors	Insulators
S(μVK^{-1})	~5	~200	~1000
$\sigma(\Omega^{-1}\text{cm}^{-1})$	~ 10^6	~ 10^3	~ 10^{-12}
Z(K^{-1})	~ 3×10^{-6}	~ 2×10^{-3}	~ 5×10^{-17}

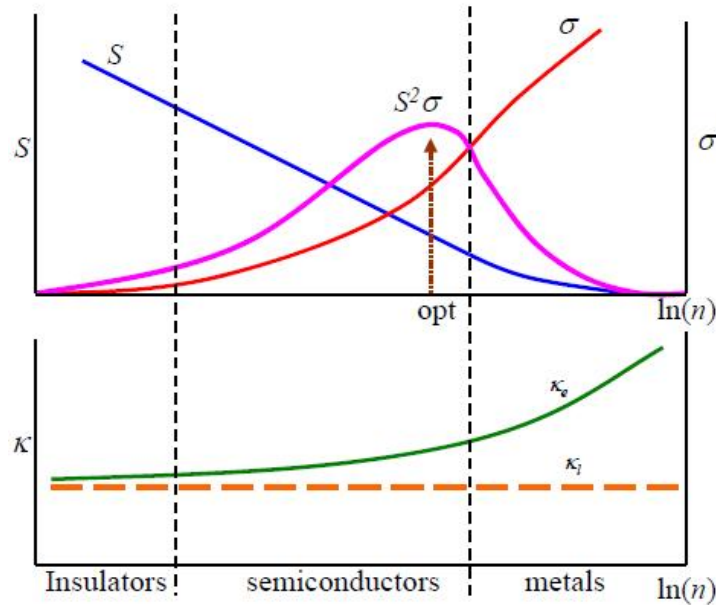


Figure. 1.6. Seebeck coefficient S , electrical conductivity σ , $S^2\sigma$, and electronic (κ_e) and lattice (κ_l) thermal conductivity as a function of free-charge-carrier concentration n (Zheng et al., 2008)

Table 1.1. is indicated the comparison of thermoelectric properties of metals, semiconductors and insulators at 300K and figure 1.4. is illustrated the Seebeck coefficient S , electrical conductivity σ , $S^2\sigma$, and electronic (κ_e) and lattice (κ_l) thermal conductivity as a function of free-charge-carrier concentration n . It is apparent that metals have very good electrical conductivity, but their very low Seebeck coefficient and large thermal conductivity. thus metals is not the most desired materials for TE applications. With large band gap, for insulators they have large Seebeck coefficient ($\sim 1000\mu\text{V/K}$), while they possess low electrical conductivity resulted from a small thermoelectric power ($S^2\sigma$), and small figure of merit (Z) ($\sim 5 \times 10^{-17}$) according to the metals. The optimal thermoelectric materials have a large value of $S^2\sigma$, thus the materials are located in the region near the crossover between the semiconductor and metals and have optimized carrier concentration of $1 \times 10^{19} \text{cm}^{-3}$ (Zheng et al., 2008).

1.1. The Wiedemann -Franz Law

A high quality thermoelectric material requires a high electrical conductivity and thermopower and the low thermal conductivity. The electrical conductivity and thermopower combine into the quantity $P=\sigma S^2$ referred as the ‘power factor’ due to their electronic properties (Dmitriev and Zuyagin, 2010). The Wiedemann-Franz law defines that the electronic contribution to the thermal conductivity is proportional relationship to the electrical conductivity of the materials (Alaam and Ramakhrisna, 2013).

$$\frac{\kappa_e}{\sigma} = LT = \left(\frac{\pi^2}{3}\right) \left(\frac{k_B^2}{e^2}\right) T \quad (1.8.)$$

$$\kappa_e = L\sigma T = n_e \mu L T = \frac{1}{3} c_v v \Lambda \quad (1.9.)$$

$$\kappa_{ph} = \frac{1}{3} v_s c_v L_{ph} \quad (1.10.)$$

$$\begin{aligned} L_0 &= \frac{\pi^2}{3} \left(\frac{k_B}{e}\right)^2 = 2.44 \times 10^{-8} \text{W}\Omega\text{K}^{-2} \quad (1.11.) \\ &= 2.44 \times 10^{-8} \frac{V^2}{K^2} \end{aligned}$$

$$L_0 = 2 \left(\frac{k_B}{e}\right)^2 = 1.48 \times 10^{-8} \frac{V^2}{K^2} \quad (1.12.)$$

Where k_B is defined to the Boltzmann constant, e is the charge of electron, n is the carrier concentration, μ is the charge carrier mobility, L is the Lorenz factor c_v is the heat capacity at constant value, v_s is the velocity of sound, L_{ph} is the phonon mean free path, v is the electron velocity that can be assumed to be Fermi velocity v_f and Λ is the electron mean free path, σ is the electrical conductivity and T is referred to the temperature in Kelvin. (Fergus, 2012) (Ruoho, 2012), (Tritt, 2002)

The Lorenz factor is constant only for materials and changes specifically with carrier concentration. A wide consideration of undetermination in electronic contribution happens in low carrier concentration of materials where the Lorenz factor is the reduced via approximately 20% from the free-electron value. In addition, the undetermination in κ_e is formed from combined conduction. The conduction reveals a bipolar term into the term conductivity (Snyder and Toberer, 2008).

c_v and v_s are generally temperature independent for $T > 300K$, thus at high temperatures.

$$\kappa_{bipolar} = \kappa_{bi} = \sigma_e T \left(\frac{k_B}{2} \right)^2 \left(\frac{(2r+5+n_g)^2}{1+e^{n_f} e^{n_g} \left(\frac{m_e^*}{m_h^*} \right)^{3/2} (\mu_e/\mu_h)^{3/2}} \right) \quad (1.13.)$$

In the above equation (1.8.) r , m is stated as scattering factor and carrier effective mass.

To success effective thermoelectrics, infamous way is replacing of bipolar effect, when two types of carriers are present. The significant effect is the conduction of the heat from hot side to cold side throughout lack-net-current, the origin of κ_{bi} . (Alaam and Ramarkrishna, 2013)

In a n-type material, the bipolar effect could be restrained using following conditions;

- i) The external carrier concentration are increased (i.e. through increasing the Fermi energy E_F),
- ii) The band gap E_g are enlarged,
- iii) The ratio of m_e^*/m_h^* or μ_e/μ_h are increased.

The total thermal conductivity is consistent of the thermal conductivity arisen from the movement of the charge carriers themselves; κ_e referred the electronic contribution, and thermal conductivity arisen from lattice vibrations, κ_l defined the lattice contribution (Dmitriev and Zvyagin, 2010).

According to the Wiedemann-Franz law; thermoelectric dimensionless figure of merit can be maximized through maximizing the electric conductivity and minimizing thermal conductivity(Dmitriev and Zvyagin, 2010).

$$ZT = \frac{S^2 T}{\rho \kappa_{total}} = \frac{\rho^2 / L}{1 + \frac{\kappa_l}{\kappa_e}} \quad (1.14.)$$

The Wiedemann-Franz law restricts the ratio of the electronic contribution to the thermal conductivity and electrical conductivity of metal(Nikiforov et al.). Whereas revealing a core materials debate for succeeding high thermoelectric efficiency. For metals, the Seebeck coefficient principally specified ZT, with either very high electrical conductivity or very low lattice conductivity as seen equation (1.14.) where $\kappa_l/\kappa_e \ll 1$ (Snyder,2008).

In ZT values, the energy carriers such as electrons and holes contribute to electric conductivity, electronic thermal conductivity, whereas the phonons also contribute to the electronic lattice conductivity.

Due to high values of ZT, it is required to acquire both high Seebeck coefficient and the electrical conductivity, and low thermal conductivity. These properties are interconnected to each other. As σ typically increases, S decreases and κ_{Total} increases.

- i) Low efficacy (with $ZT < 1$) of thermoelectric tools has largely restricted to their applications,
- ii) $ZT = 1$ is a maximum limit
- iii) In $ZT > 1$ cases, as ZT increases, the new thermoelectric applications show up.

Table 1.2. Examples on the Required device ZT (Vining, 2009)

Examples	Required device ZT
Solar thermal ‘engine’ replacement	>8–20
Industrial waste heat, geothermal bottoming cycles	>4
Vehicle waste heat, car cooling/heating, home co-generation	>1.5–2
Remote power, ‘personal’ micropower, all existing applications	>0.5–1

The most widely promising examples; vehicle waste heat is appeared.(Table 1.2.)

The Wiedemann- Franz law only performs to thermal conductivity via charge carriers. The carriers occur one-third of total electrical conductivity in thermoelectric materials (Ruoho, 2012).

With phonon scattering via adding flaws, the reducing of κ_{total} happens in reducing in both carrier mobility and electrical conductivity(Alaam and Ramakrishna, 2013) For semiconductors, the law is stated following equation;

$$\frac{\kappa_e}{\sigma} = (s + 2) \left(\frac{k_B}{e}\right)^2 T \quad (1.15.)$$

Where s is the scattering parameter referred as

$$l = l_0(T)E^s \quad (1.16.)$$

l is the defined as free path length (mean free path) of the scattering, E is the carrier energy, s is dependent on the scattering mechanism constant. For acoustic phonon scattering, optical phonon scattering (alloy disorder scattering), ionized

impurity scattering, s is given values in $-1/2$, $1/2$ and $-3/2$ respectively (Dughaish, 2002).

κ_l is referred as function of the acoustic phonon scattering processes like phonon-phonon scattering, phonon-electric carrier scattering and phonon-impurity scattering whereas κ_e will be influenced via nanostructuring if σ varies because of carriers scattering (Qintana, 2013). Both phonons and charge carriers can be subjected to distribution, because of other phonons, lattice holes, impurities, electrons, grain boundaries, interfaces. Thus distribution ends in variable of thermal conductivity.

The scattering mechanisms will affect the phonon mean free path. For nanostructured materials; the thermal conductivity can be given smaller values than their bulk counterparts. Because, with mean free paths, the effective phonon scattering of acoustic phonons is longer than the characteristic dimensions of the nanostructured materials. This process is referred to phonon-boundary scattering. Electric carriers transport could remain unmoved, while phonons can be scattered in nanostructured materials. Because, their mean free path is different orders of magnitude smaller than phonons (Qintana, 2013).

1.2. The Hall Effect

The Hall Effect discovered by Dr. Edwin Hall in 1879 is defined as an occurrence of transverse electric field vertical to both magnetic field and the original current flow, when a current-carrying conductor is put into a magnetic field. In other words, the mobile charges forming the current are distorted sideways and stepped up a potential variety between the two sides of the conductor when a magnetic field is performed vertical to a current in any conductor (Honeywell) (Grubbs, 1959).

A thin sheet of semiconducting material referred to Hall element through which a current is run. When magnetic field is absent, output connections are vertical to direction of current. If the Hall voltage is measured, the output is given zero value, when magnetic field is absent, and, non-zero will be seen at each output terminal (Honeywell).

A method of measuring both specific resistivity and Hall Effect of flat specimens of optional shape is dependent on a theorem. The theorem is defined to hold for a flat specimen of selective shape. The contacts are enough small and locate at the circuit of the specimen (Honeywell).

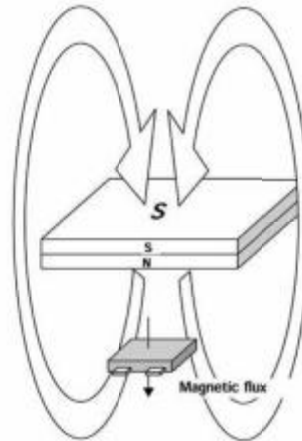


Figure 1.7. A Hall voltage generated from current flow in the semiconductor material (Rohm)

Both the specific resistivity and the Hall effect of the flat specimens selective shape can be measured non-knowing the current profile, if the below conditions are summed up;

- i) The contacts are at the circuit of the specimens
- ii) The contacts are equal small
- iii) The contacts are in homogeneously thickness
- iv) Specimen surface is one by one joined (Pauw, 1959)

In the Hall Effect, to maximize ZT of thermoelectric material, both α and σ will be low.

$$\mu_H = \frac{R_H}{\rho} \quad (1.17.)$$

In the above equation (1.17.); μ_H and R_H is defined to temperature dependence of the electron Hall mobility and Hall coefficient respectively(Pagava and Chkharishvili,2004).

1.4. Thermoelectric Materials And Manufacturing Methods

Thermoelectric materials are classified by the temperature interval of their application:

- i) Bi_2Te_3 and its alloy: They ordinarily work around room temperature and have a maximum operating (working) temperature,
- ii) PbTe based alloys and TAGS(Te-Ag-Ge-Sb): they work intermediary temperature between 600-900K,
- iii) Si-Ge alloys: they work at high temperature(1000-1300K) and utilize in power generation tools.

Researchers study other materials such as Ca, Al etc. also.

The discovery of thermoelectric materials started from traditional semiconductors such as group III-V(e.g. InSb), IV-IV(e.g. SiGe), group IV chalcogenides(e.g. PbTe), group V chalcogenides (Bi_2Te_3 , Sb_2Te_3) to recent complex materials (i.e. skutteridites, clathrates, half Husler alloys, complex chalcogenides, cobaltes and so on) and low-dimensional thermoelectrical materials such as quantum well, quantum dot, nanowires, molecular junctions.

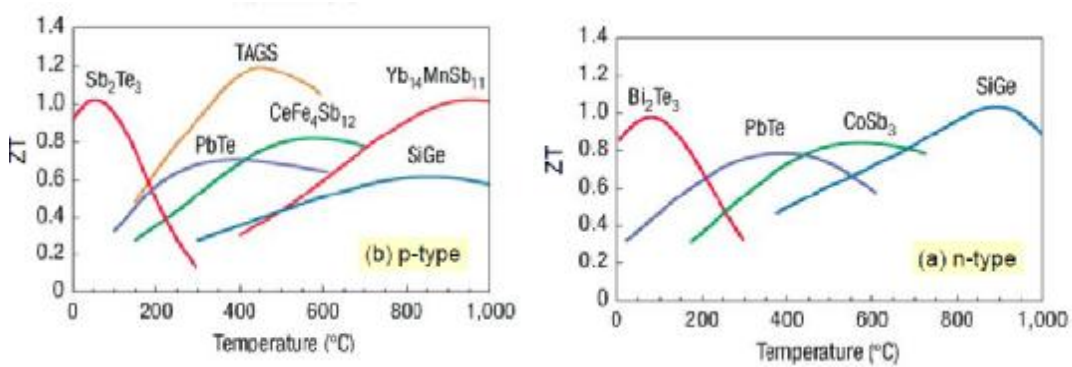


Figure 1.8. Temperature dependent on the Figure of merit (ZT) curves of p-type and n-type materials (Snyder and Toberer, 2008)

The commonly utilized thermoelectric materials are alloys of Bi₂Te₃ and Sb₂Te₃. Bi₂Te₃ alloys have been demonstrated to have the greatest figure of merit for both n- and p-type TE systems, for near-room-temperature applications such as refrigeration and waste heat recovery up to 200°C. Besides a reduction in lattice thermal conductivity, alloying with Sb₂Te₃ and Bi₂Se₃ permitted for the fine tuning of the carrier concentration. Whereas n-type compositions are close to Bi₂(Te_{0.8}Se_{0.2})₃, the most widely studied p-type compositions are near (Sb_{0.8}Bi_{0.2})₂Te₃. For single and polycrystalline materials peak ZT values are typically varied in the range of 0.8 to 1.1 with p-type materials achieving the highest values (Figure 1.8.)

The manufacturing methods of TE materials can be classified with their categories:

- crystal growth of bulk materials from melts
- thin –film preparation techniques
- powder based techniques

In the crystal growth techniques of thermoelectric materials, many various parameters affect the features of thermoelectric materials. A significant parameter of those is the microstructure, specifically the grain boundary. Their effects can be decreased or even eliminated through utilizing of single crystals. This case will be revealed the intrinsic feature of the compounds (Wagner et al. 2014). Throughout

various crystal planes, carrier transports are apparent. The prior-growth of a certain crystal planes would possess a great influence on thermoelectric performance (Zhu et al. 2014).

Thin film technique is a method to enhance the thermoelectric properties of thermoelectric materials via the increasing both the electrical conductivity and Seebeck coefficient. Because the technique improves the stronger quantum confinement effect. The enhanced thermoelectric properties of the film offer a huge potential in miniaturization sensors, micropower source of the film thermoelectric devices. (Zheng et al. 2014)(Lee et al. 2012). To enhance of both the electrical conductivity and Seebeck coefficient is difficult due to dependent on the figure of merit. Thin film techniques of materials are pointed out sol-gel, PLD, MOCVD CVD etc.(Castro et al., 2014)

Powder metallurgy method consists of milling, pressing and sintering processes and provides in producing such nanostructured thermoelectric materials (Lu and Liao,2013). Powder metallurgy is utilized to obtain improved mechanical properties such as higher compressive strength (Lim et al., 2006)(Bhuiyan, 2011).The same case is seen in the increasing of the figure of merit, whereas decreasing in the lattice conductivity because of grain purifications. The powder can be prepared gas atomization, mechanical alloying, chemical reactions besides other special methods based on the material, economy, their application areas(Bhuiyan, 2011)

2. PREVIOUS STUDY

2.1. The Thermoelectric Properties of Materials Produced By Powder Metallurgy

Powder metallurgy is related to manufacturing of metal powders and conversion of them to useful shape (Ramakrishnan, 1980). This method includes milling, pressing and sintering processes and widely applied in manufacturing nanostructured thermoelectric materials (Lu and Liao, 2013) (Figure 2.1.). In this method, it is acquired an improved mechanical property such as high strength and hardness (Lim et al., 2006) (Yang et al., 2009). Manufacturing of materials via powder metallurgy methods also achieves the increase of figure of merit because of grain purification as well as higher compressive strength (Bhuiyan, 2011).

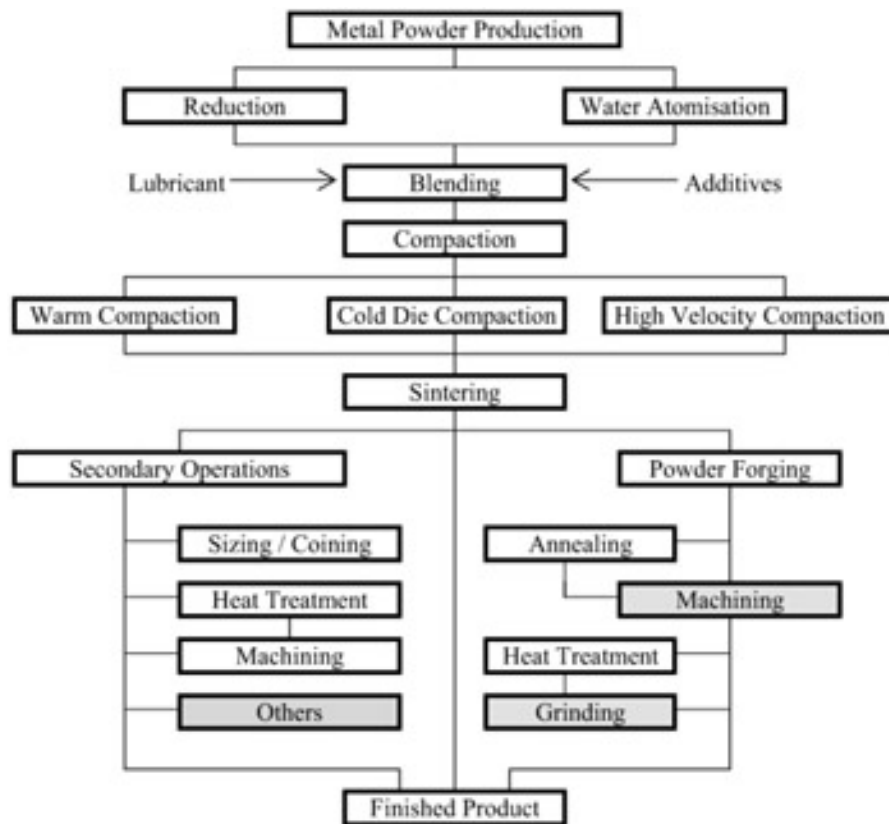


Figure 2.1. Schematic of the powder metallurgy processing steps.

Mechanical and thermoelectric properties are exceedingly related to the microstructures of materials and microstructure formation is affected via the hot consolidation process. For this reason, this case plays an important role to analyze and establish the connection between the material processing parameters, microstructures and their properties (Bhuiyan, 2011). As a known, microstructure of materials is qualified via particle size, shape, content, state of dispersed phases and the homogeneous grain boundary (Yang, 2009).

After the milling process, the ground powders are exposed to a high pressure in a mould to produce an intensive bulk either at low temperature (referred to cold press) or as well as heating (known as hot press) (Lu and Liao, 2013).

TE materials produced by cold press method generally show lower figure of merit according to their crystalline counterparts. Cold pressing technology includes of various steps, these steps influence feature of final material discretely. Navrátil et al. observed that thermoelectric properties (electrical conductivity, Seebeck coefficient, dimensionless figure of merit) of $Sb_{2-x}Bi_xTe_3$ ($x=0.43-0.51$) TE materials produced cold pressed varies throughout the grinding, pressing and sintering processes. A comparatively high figure of merit can be succeeded from various compositions in the existence of $Sb_{1.5}Bi_{0.5}Te_3$ alloys. In related to particle size and also it is determined that the smaller grain size caused to the bigger decreasing of σ values and the Seebeck coefficient of pressed materials increased with reducing of concentration of free carriers (Navrátil et al., 1996).

Hot pressing method consists of hot pressing with mechanical alloying processes. This both processes have conducted to improvement of the TE performances (Ueno et al., 2005). Using low temperature hydrothermal method, ball milling and rapid solidification consisted hot pressing structural transitions (as known as microstructures) and based to physical effects have been succeedingly applied to bulk materials and comparatively high TE performances have been succeeded. Shen produced the polycrystalline pseudo-binary $Bi_{0.5}Sb_{1.5}Te_3$ alloys fabricated via this method. Generally as a known the Seebeck coefficient varies conversely proportional to the carrier concentration and electrical conductivity cause to two variances as the carrier concentration and mobility. Whereas the carrier

concentration is dependent on the composition, the mobility can be related to grain size, boundary, density and flaws. Circumstanly authors observed that the Seebeck coefficient values of materials reduced with temperature increase and reach a maximum value at about 300K and the differences on electrical conductivity could be caused to various carrier concentrations led to the composition (Shen et al., 2011) (Figure 2.2.).

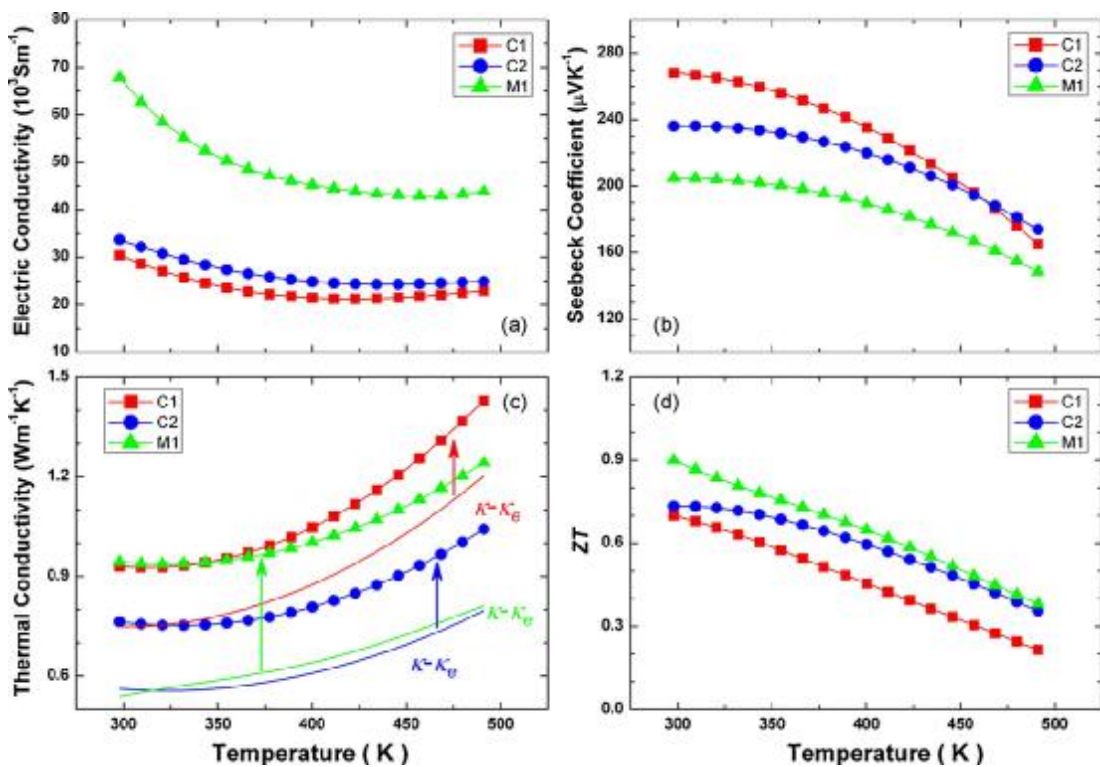


Figure 2.2. Temperature dependences of (a) the electrical conductivity, (b) the Seebeck coefficient (c) the thermal conductivity (d) ZT value. of the $\text{Bi}_{0.5}\text{Sb}_{1.5}\text{Te}_3$ bulk samples (Shen et al., 2011).

Large amount of grain boundary cause to scattering and important reduce in the conductivity because phonon conduction controls major part of thermal conductivity. MA method provides very fine grain size and hence enhances important possibility in order to enhance more efficient TE materials (Sridhar and Chattopadhyay, 1998).

For the synthesis of semiconducting TE compounds MA method is an advantageous method. The occurring powder produced by MA seems very

homogeneous and indicate low thermal conductivity because of large amount of stimulated grain boundaries. It explains the known as figure of merit. This figure of merit provides a significant measure for the performance of TE devices such as generators, Peltier coolers and sensors. (Schilz et al., 1999)

The mechanical alloying process(MA) developed by John Benjamin and his co-workers at the late 1960's is a powder processing method that enables manufacturing of homogeneous materials beginning from mixed powder mixtures and is a well-established method in solid-state powder processing methods (Li et al., 2013; Suryanarayana, 2001). This method has become a well-liked method to fabricate nanocrystalline materials for various usefulness; process simplicity, the required cheap equipment, the practicability to manufacture all classes of materials. Bulk TE materials with excellent features can be prepared via mechanical alloying and the sequent consolidation of powders to enhance an ultrafine grain structure ((Li et al., 2013).

In the study of Yang et al., p-type single phase $(\text{Bi}_2\text{Te}_3)_x(\text{Sb}_2\text{Te}_3)_{1-x}$ ($x=0.20, 0.225, 0.25, 0.275$ and 0.30) thermoelectric materials with high densification prepared through bulk mechanical alloying(BMA) and hot pressing(HP) from precursor elemental Bi, Sb and Te granules with 5 N purity and 1–5 mm diameter. Authors observed for $x \leq 0.275$, rising the Seebeck coefficient with x , reaches its maximum at the composition of $x= 0.275$, and then reduces rapidly., the figure of merit of $(\text{Bi}_2\text{Te}_3)_x(\text{Sb}_2\text{Te}_3)_{1-x}$ reduced rapidly with increasing x , when $x > 0.25$ (Yang et al., 2000). In the other study of Yang et al., it was studied n-type $(\text{Bi}_2\text{Se}_3)_x(\text{Bi}_2\text{Te}_3)_{1-x}$ with various chemical composition produced by bulk mechanical alloying(BMA) and hot pressing(HP) from precursor materials Bi, Te and Se granules. They observed the reducing the electrical resistivity and the Seebeck coefficient of $(\text{Bi}_2\text{Se}_3)_{0.05}(\text{Bi}_2\text{Te}_3)_{0.95}$ due to the doping with SbI_3 , so, the enhancement of figure of merit was not materialized. To improve the thermoelectric properties, annealing the as-hot pressed $(\text{Bi}_2\text{Se}_3)_{0.05}(\text{Bi}_2\text{Te}_3)_{0.95}$ (adequately long time) acts important role and the maximum figure of merit of $(\text{Bi}_2\text{Se}_3)_{0.05}(\text{Bi}_2\text{Te}_3)_{0.95}$ was obtained as $2.31 \times 10^{-3}/\text{K}$. As a known, the thermal conductivity consists of the lattice and carrier thermal conductivity, when the doping content varies. Properly the

thermoelectric properties will be varied. In this study, the carrier concentration increases and for this reason, both the electrical and thermal conductivities rises (Yang et al., 2000) (as seen in Figure 2.3.-4.).

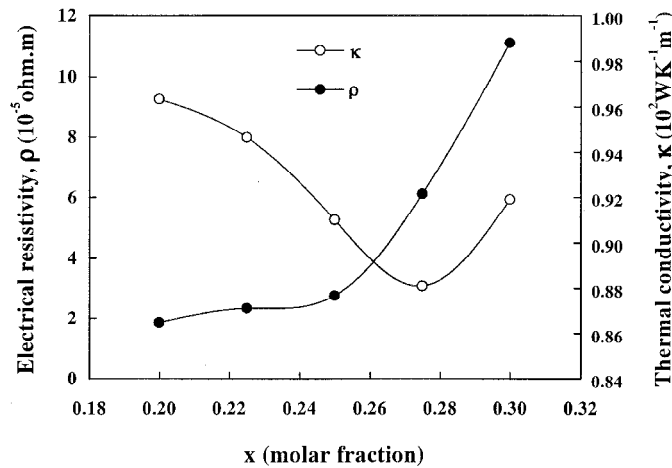


Figure 2.3. x (molar fraction) dependence of the Electrical resistivity and thermal conductivity of $(\text{Bi}_2\text{Te}_3)_x(\text{Sb}_2\text{Te}_3)_{1-x}$ (Yang et al., 2000).

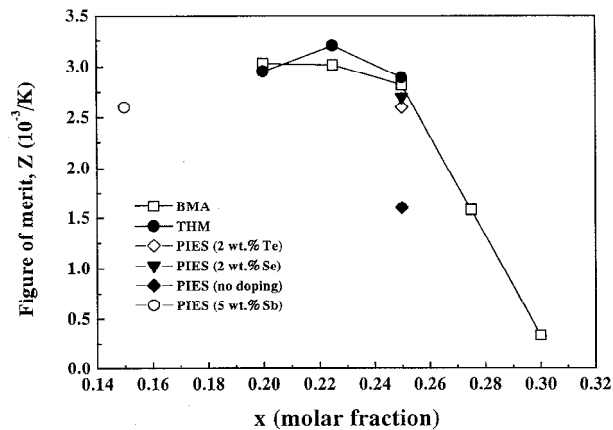


Figure. 2.4. x (molar fraction) dependence of figures of merit for $(\text{Bi}_2\text{Te}_3)_x(\text{Sb}_2\text{Te}_3)_{1-x}$ produced via different methods.(Yang et al., 2000).

The MG or MA technique is a very influential method in order to prepare the thermoelectric materials with high performance and more developments anticipated Katsuyama produced the thermoelectric materials via mechanical grinding (MG) or alloying (MA). The crystal grain is purified and the doped materials are distributed in the matrix through milling process. They revealed that progressed alloying between

the matrix and addition improves the phonon scattering at the grain boundaries occurring in the reduction of the thermal conductivity and however, the increasing of the Seebeck coefficient is caused to the stabilization of the matrix phase. (Katsuyama et al., 2004).

The degree of the scattering of the phonon is in proportion to the density of the below microscopic formations, and therefore, in order to reduce of κ_{ph} , introduce more disordered and substituted atoms, increase the density of the crystal grain boundary and more disperse the impurities, it is effective. for the low κ_{ph} , the ideal microscopic structure is illustrated in Figure 2.5-6.

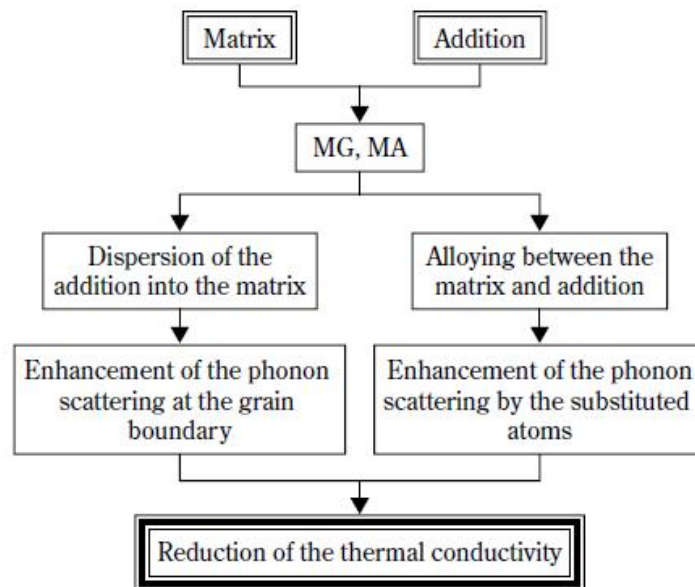


Figure. 2.5. Fundamental procedure for preparing the high performance thermoelectric materials by Powder Metallurgy (Katsuyama et al., 2004)

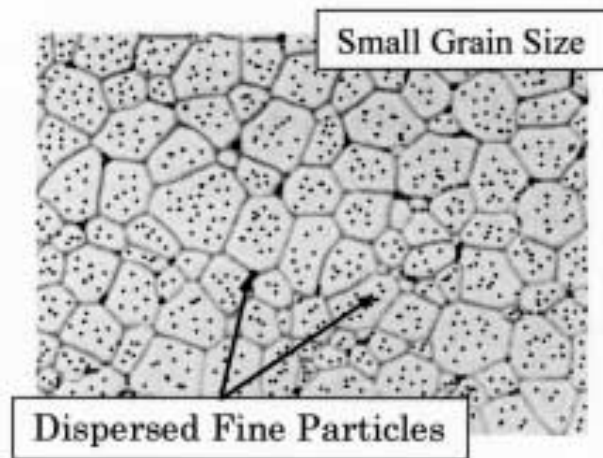


Figure. 2.6. Ideal microscopic structure for the low κ_{ph} . (Katsuyama et al., 2004).

Cryogenic grinding is a low-cost method and promises in large-scale application areas. Chen et al. produced nano-sized Bi_2Te_3 thermoelectric material powders through cryogenic grinding.

As seen in Figure 2.7., it was found that Bi_2Te_3 was not transformed into a non-equilibrium amorphous phase or decomposed through the cryogenic grinding process, and also as-prepared nano-powders possessed excellent sinterability. This technique might also be viable to the thermoelectric materials (Chen et al. 2012).

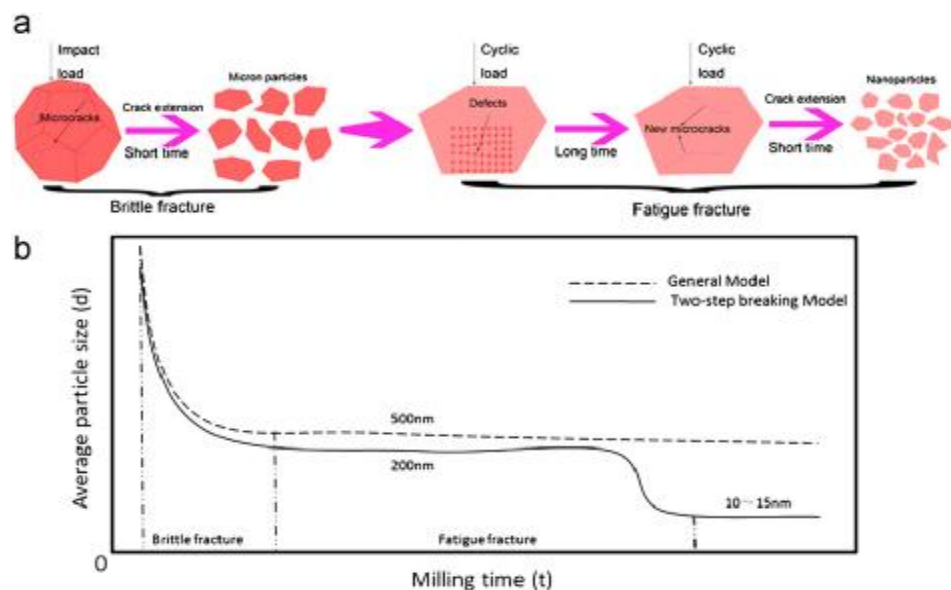


Figure 2.7. (a) A sketch of the break-down from micron to millimicron throughout the CG process. (b) Milling time related to average particle size of the CG samples as compared with that of the HEBM sample.

For characteristic powder metallurgy method, a high temperature sintering process is required to densify compacted powders and eliminate crystal flaws. This flaws resulted from ball milling and pressing processes. On the other hand, an prolonging thermal sintering process may lead to recognizable grain growth in the sintered bulk. This case is not desired for produced nanocrystalline thermoelectric materials with high ZT values (Liao, 2010).

Wang and Fan examined the thermoelectric features of $\text{Sr}_{1-x}\text{La}_x\text{TiO}_3$ nanoparticle compacts produced via the hydrothermal method followed by a cold-pressure procedure. Authors revealed the expansion of the unit cells in nanoparticles related to the improvement of thermopower and the morphology of nanoparticle compacts consisting of numerous interfaces strongly compressed the phonon thermal conductivity. It was obtained The ZT value of the nanoparticle compacts almost ~ 0.12 at 300 K, approximately 30% larger according to samples of both epitaxial films and single crystals (Wang and Fan, 2011) (Figure 2.8.-9.).

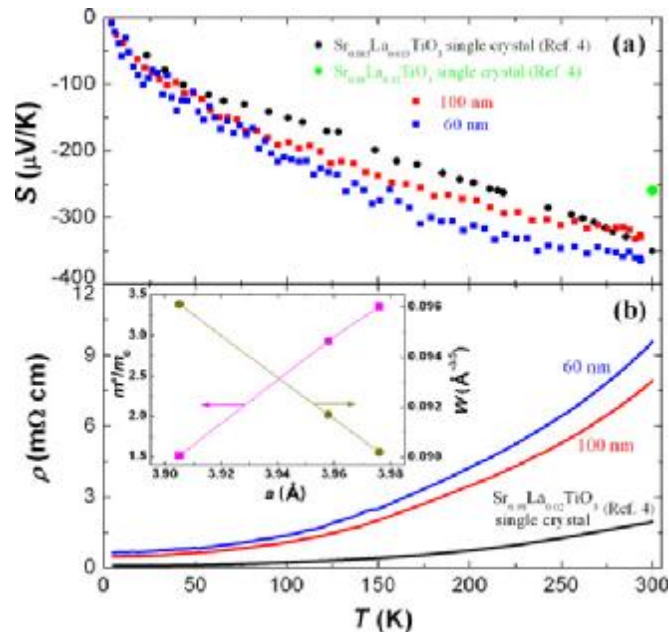


Figure 2.8. Temperature based on (a) thermopower S and (b) resistivity ρ for the nanoparticle compacts and single crystals (Wang and Fan, 2011).

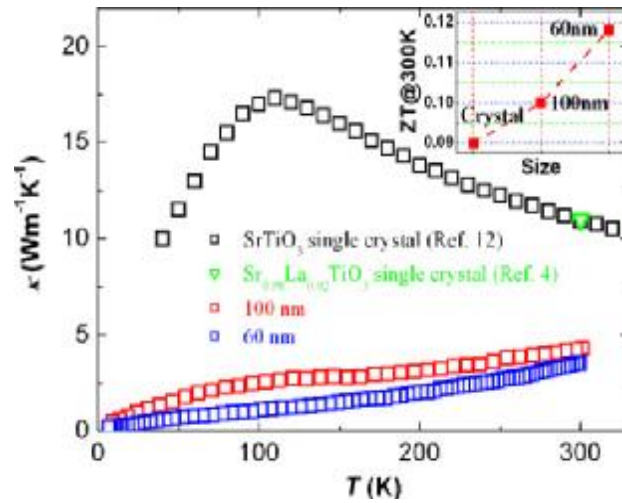


Figure 2.9. Temperature dependences of thermal conductivity κ for the nanoparticle compacts and single crystals (Wang and Fan, 2011).

Han et al., produced thermal conductive silicone rubbers filled with BN micro particles assisted with electric field assisted curing, and investigated the electric field effect and studied the thermal conductivity of BN/silicone composites with differing particle volume fractions and electric-field strengths. The electric field could happen in the constitution of an anisotropic aligned structure. The structure is put upon together the shape and thermal conductivity anisotropies of BN powder in the same direction. In this direction, the thermal conductivity has been importantly improved (Han et al, 2012).

Kuo et al. synthesized densitiae fine-grained PbTe bulk materials without oxide phases prepared a process that consisted of cryomilling defined to mechanical alloying at cryogenic temperature and spark plasma sintering (SPS). In this study, it was observed when the grain size decreases to the nano-scale, the thermal conductivity decreases and the Seebeck coefficient increases, the electrical conductivity only imperceptible changes for all sintered samples. They stated that the combination of cryomilling and spark plasma sintering (SPS) may enhance the thermoelectric properties of this bulk samples (Kuo et al., 2011) (Figure 2.10.).

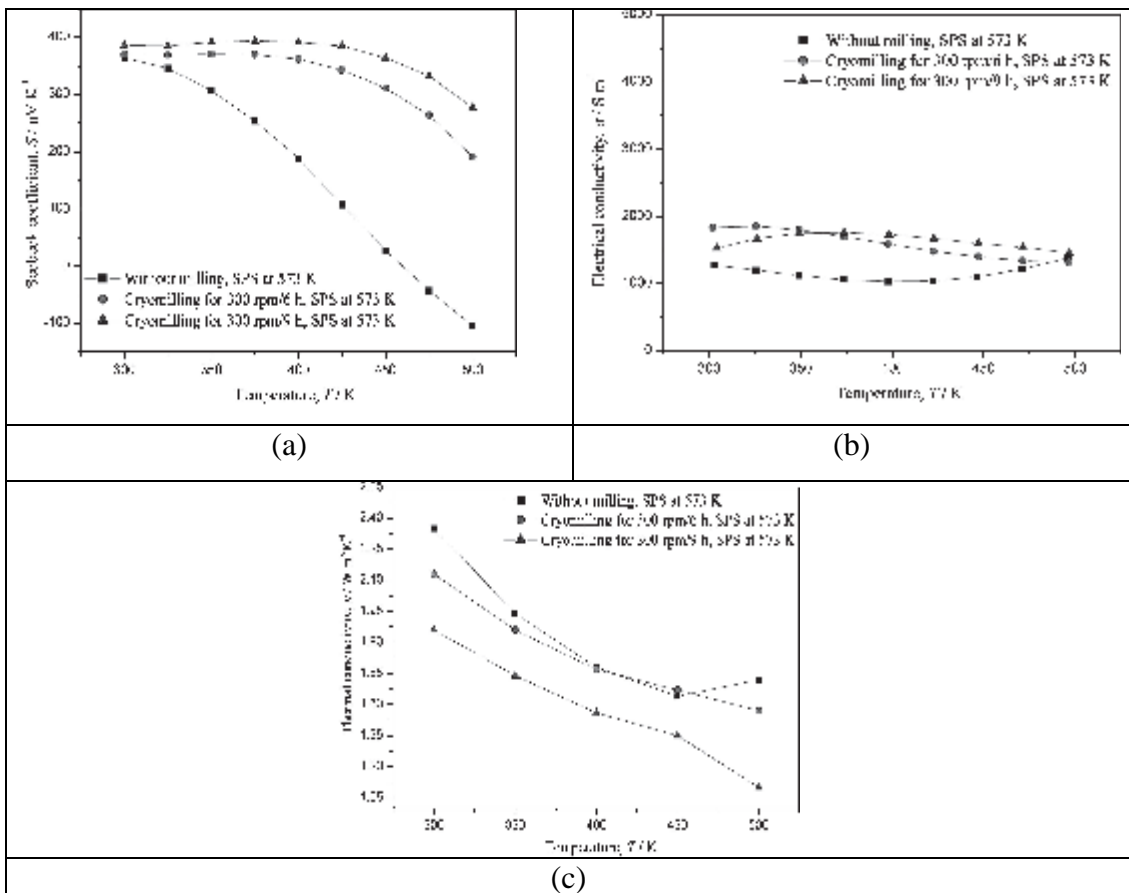


Figure. 2.10. Temperature-dependence of (a) Seebeck coefficient (b) electrical conductivity (c) thermal conductivity for PbTe samples prepared by different cryomilling times and sintered at 573 K (Kuo et al., 2011)

Alleno et al., prepared polycrystalline $\text{Co}_{1-x}\text{M}_x\text{Sb}_3$ ($\text{M}=\text{Ni}, \text{Pd}$) skutterudites synthesized through melting, annealing and spark plasma sintering. They determined the solubility limit of Pd and Ni of $x_{\text{max}}=0.03$ and $x_{\text{max}}=0.09$ respectively. It was anticipated the reducing values of the Seebeck coefficient with temperature for all x, in a degenerate semiconductor, till reaching the minimum increasing from the minority carrier conduction regime. It was revealed the minimum variations to higher temperature range from 540K to 630K in conformance with the rising of the electron concentration (Alleno et al., 2013).

2.2. Previous Studies on Thermoelectric Properties of Al-Zn-Mg-Cu Materials

Al-Zn-Mg-Cu alloys as-known as 7xxx series alloys are commonly used in aircraft structures, automobile industry due to their superior properties such as low density, high strength, hardness, ductility and toughness, outstanding workability (Fang et al., 2009; Jia et al., 2012; Liu et al., 2014 ;).

The microstructure of high-strength aluminum alloys includes of three types: (i) second phase particles (constituents) (ii) dispersoids and (iii) the strengthening precipitates.

Second phase particles (constituents): The particles occur from either the existence of iron and silisium impurities or excessive amounts of major alloying elements. The final size of the particles relates to the fabrication method and the size may vary from 5 to 30 μm .

Dispersoids: The particles are known as the intermetallic particles and produced from elements such as Cr, Zr and Mn that have low solubility in Al at all temperatures. At high temperatures (350-500°C) and for long times (6-24 hrs), homogenization acts role on the precipitated dispersoid particles such as Al_3Zr and spinule grain boundaries. Therefore this case prevents grain growth throughout both thermo-mechanical processing and solution heat treatments. The size of dispersoid particles may range from 20 to 50 nm (Dixit et al., 2008).

Strengthening precipitates: The precipitation of Al-Zn-Mg-Cu alloys includes three precipitation sequences with related to the composition. The base sequence consisting mostly of Mg and Zn is considered to dominate hardening in most Al-7xxx alloys;

Supersaturated Solid Solution (SSS) _{α} \rightarrow Guinier-Preston (GP) zones \rightarrow spherical or disc shaped semicoherent η' , disc shaped $\rightarrow \eta$

The first precipitates are coherent with the parent matrix and have metastable phase. The precipitates plays role as heterogeneous nucleation sites for more

thermodynamically stable precipitates causing to the dissolution of the metastable phases.

η -phase is a quaternary phase occurred from solid solution of $MgZn_2$ with AlCuMg components (i.e. $Mg(Zn,Al,Mg)_2$ or $Mg(Zn_2AlMg)$) and a stable phase with known as crystal structure. (Starink and Li, 2003; Waterloo et al., 2001). The Pseudo-hexagonal η' -phase is generated throughout the second aging phase. In a set of well-known direction relationships to the Al-matrix, the phase is transitioned to the stable hexagonal-Laves phase η - $MgZn_2$ as larger incoherent particles (Kverneland et al., 2011).

A second one occurs generally at $T > 200^\circ C$ and includes the T-phase.



If the ratio Zn: Mg is small, some aluminum will compensate for the low zinc content. T-phase particles which have the chemical composition $Mg_{32}[Al, Zn]_{49}$ will be replaced instead of η - particles. The T-phase particles consist of some copper in some alloys.

A third one includes exclusively Cu and Mg; $(SSS)_\alpha \rightarrow S$.

S- phase has the Al_2CuMg (Starink and Li, 2003),(Zander and Sandröm, 2008).

Guinier-Preston zones are coherent whereas η' and η phases have semi-coherent and incoherent structures, respectively, and occur throughout quenching and aging processes (Dixit et al., 2008).

Guinier-Preston(GP)zones have two types of the GP(I) and GP(II) zones and the types are observed throughout the early stage;

- Ø **GP(I) zone:** The equiaxed zones are occurred over a wide temperature range.
- Ø **GP(II) zones:** the disc-shaped zones are one-to two layers thick on $\{111\}_{Al}$ and are occurred via aging at temperatures above $75^\circ C$ (Kverneland et al., 2011)

High strength Al 7xxx series alloys are hardened via precipitation treatment process involved in solution treatment, quenching and ageing steps. Firstly; into Al-matrix, the soluble alloying elements are dissolved in solution treatment. Secondly; these elements are quenched so as to form the supersaturated solid solution. Lastly, formed solid solutions are aged artificially in order to acquire metastable η' precipitates for a certain time. As both size and distribution of these precipitates are optimized to prevent influentially the dislocations, maximum strength is reached (Zhang et al., 2014).

The metastable η' phase will maintain growing and transit to the η phase (equilibrium MgZn_2) throughout extended ageing. During slow cooling, the transformed equilibrium η phase can also deposit on heterogeneous nucleation structures, occur in a loss of solute from solution and a decreased strength after following ageing step (Zhang et al., 2014)

Aluminum alloys are alloyed with the elements of Zn, Mg, Cu and Zr. These elements Zn, Mg and Cu formed the Aluminum 7xxx series alloys occur precipitates of different ternary and quaternary compositions subsequent the steps of solution heat treatment and ageing. The strengthening effects of the precipitates base on their size, spacing and distribution, other mechanisms such as grain boundary strengthening, solid solution strengthening and strengthening (Dixit et al., 2008). And also the precipitation hardening relates to the process parameters such as temperatures of solution and hardening, deformation prior to the ageing, additional alloying elements (such as Cu and Zr) (Waterloo et al., 2001).

Rising of the amount of hardening elements is an influential route to strengthen the alloy (Zhao ,2013). Age hardening of Al 7xxx alloys are depend on precipitation in the Al-Zn-Mg system in the compositional range (wt%) 3-7 % zinc and 0.8-3% Mg (Kveneland et al.,2011).

By increasing the amount of zinc in the alloy, it will be acquire a higher volume fraction of secondary precipitated structures accompanied with enhanced mechanical properties. To generate dispersoids improved a secondary source of strengthening chromium, copper, zirconium are well-known materials(Sharma et al., 2008). High volume fraction of Zn content is preferred in order to enhance

mechanical features. By raising of Zn amount for the traditional casting process, the disadvantages such as coarse grains and improved macrosegregation besides crack tendency caused to the very lower cooling rate (Jia et al., 2012).

In the Al-7xxx alloy type, the complex microstructure arise from the other alloying elements like of $Al_{12}Si[Fe,Cr]_3$ and Mg_2Si ., the iron-rich particles are converted to Al_7Cu_2Fe structure, other subsequent heat treatment. In other words, chromium involved alloys occur $Al_{18}Cr_2Mg_3$ dispersoids. These dispersoids are concentrated in dendrite alloys. Other silicon an iron including particles which are coarse and given little contribution to the strength can also be appeared in the 7 xxx series alloys (Zander and Sanström, 2008)

2.2.1. Searching of the Electrical- Thermal Conductivities of Al7xxx Series Alloys

Guyot and Cottigines stated the investigating of the aging of AlMgZnCu alloys in a temperature range where the metastable phase η' precipitates homogeneously with a three-fold point of view utilizing the microstructural parameters and established the correlation with the electrical conductivity on the basis of a semi-phenomenological two-base model of electron scattering and the late conductivity increase ascribing to the precipitate coarsening at constant volume fraction (Guyot and Cottigines, 1996).

Salazar-Guapuriche et al. supplied a material (aluminum alloy 7010) as a plate produced from a sheet via a complex thermo-mechanical process. Authors studied the tensile strength and proof strength, hardness and electrical conductivity of Al alloy 7010 under various temper and ageing conditions, to correlate strength with hardness and electrical conductivity. They determined the acceptably linear relationship between the strength and hardness, spite of the reasonably nonlinear relationship between hardness and strength with electrical conductivity and stated the opposite effect between electrical conductivity and hardness in the natural and over ageing conditions. They also noticed the overall raising trend for both hardness and electrical conductivity, in the preternaturally aged condition owing to the constitution

of the coherent and semicoherent precipitates($MgZn_2$) and their intermediate precipitates and lattice strain hardening (Salazar- Guapuriche et al., 2006).

Feng et al., studied The effect of retrogression and re-aging(RRA) heat treatment on the microstructure and mechanical properties of a low frequency electromagnetic casting alloy as A1-9.99%Zn-1.72%Cu-2.5%Mg-01.3%Zr. Retrogression at 200 °C for 7 min, and then re-aging at 100 °C for 24 h, the alloy acquires tensile strength up to 795 MPa, yield strength up to 767 MPa, continues 9.1% elongation, and electric conductivity of 35.6%IACS(Integrated Administration and Control System); after preaging at 100 °C for 24 h. They observed the raising the conductivity at a decreasing rate, when increasing the retrogression time, as shown in Figure. 2.11.(a). As is seen from other Figures. 2.11. (b) and (c), the effects of pre-aging and re-aging on conductivity posses the same trend, the trend is means the raising the conductivity with the extending of aging time. They revealed the most important factor impressing the conductivity firstly the retrogression time, secondly the pre-aging time and lastly re-aging time.

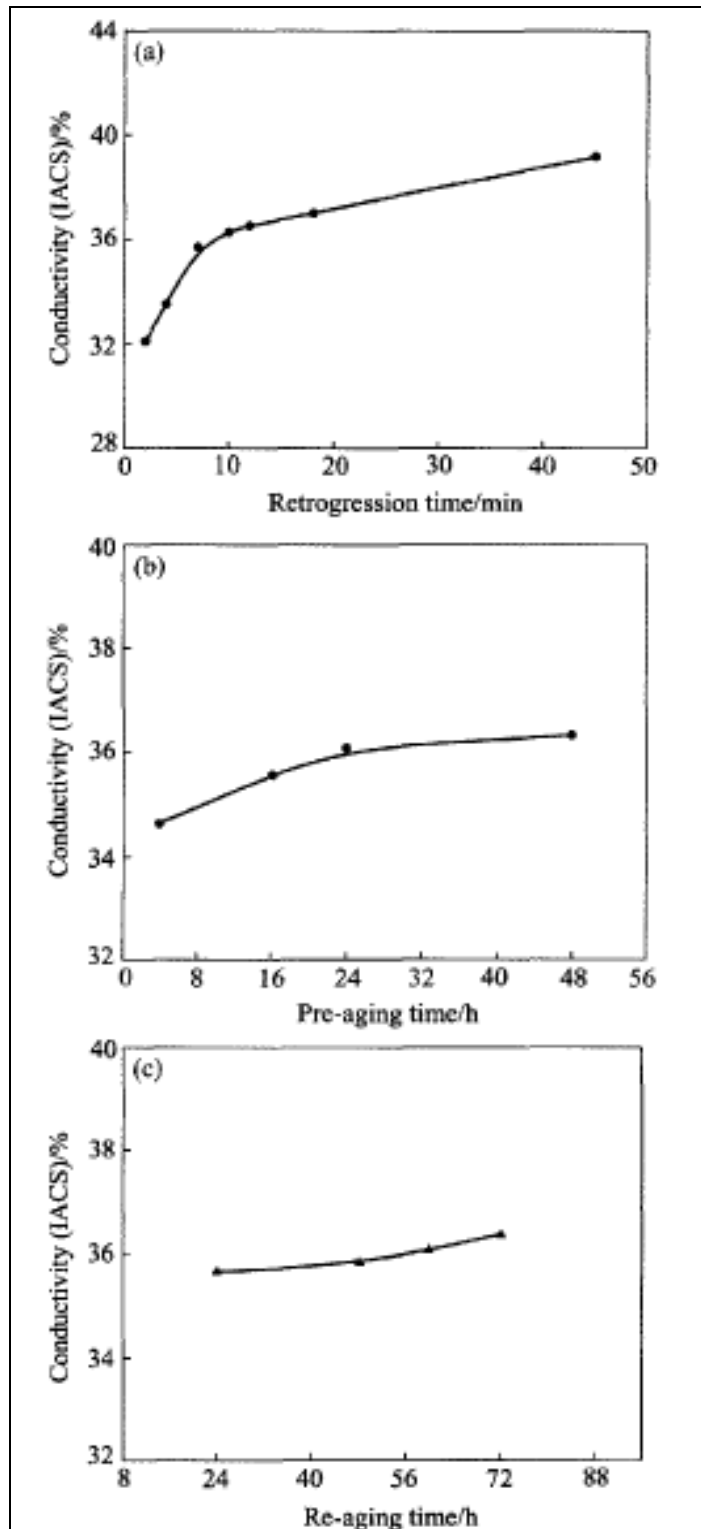


Figure 2.11. Variation of conductivity after different RRA treatments: (a) Retrogression; (b) Pre-aging; (c) Re-aging (Feng et al., 2006)

Li et al, used to 7B04 Al alloy, precipitation hardenable plate and forging material in their study. They observed the implementation of RRA treatments to material, to cause to electrical conductivities equals to T7451 condition material, simultaneously continuing the tensile strength closed to the T651 condition treated material and also showed that the retrogressed at 180° C for 60 min could generate high levels tensile properties (close to T6 strength) in integration with T74 levels electrical conductivity (Li et al.,2009).

In the article studied by Zaid et al., an implementation of retrogression and re-aging heat treatment processes are applied to improve toughness properties of the 7079-T651 aluminum alloy, while continuing the higher strength of T651-temper. It was observed the higher strength 7xxx aluminum alloys causing to low resistance to stress corrosion cracking (SCC) when aged to the peak hardness (T6 temper) and increasing the electrical conductivity with raising time or temperature of retrogression meaning the decrease of susceptibility of SCC due to the coarsening precipitates in both R-T651 and RRA-T651 alloys. (Zaid et al., 2011).

Zang et al., investigated the microstructure and the associated hardness, strength and electrical conductivity of a new Al–Zn–Mg–Cu alloy during one-step ageing treatment. Authors observed raised the electrical conductivity of the alloy continuously with raising ageing temperature and time and found the GPI and GPII zones in the alloy after ageing for 24 h at 120 °C. This case showed the existence of some stable GP zones via the ageing process. When aging at 160 °C, the hardness and strength raised rapidly after the peak value and both GPI zones and GPII zones vanished after ageing for 1 h at 160 °C.

To observe the stress corrosion cracking (SCC) resistance, The electrical conductivity is an influential method. In the Al–Zn–Mg–Cu alloy, the SCC resistance has been found to rise with increasing electrical conductivity. And the conductivity increases with increasing ageing temperature and ageing time. The electrical conductivity can be expressed as follows according to the Starink model:

$$1/\sigma_{M(t)} = \rho_{M(t)} = \rho_0 + r_{Zn}x_{Zn}(t) + r_{Mg}x_{Mg}(t) \quad (2.1.)$$

In this above equation; $\sigma_{M(t)}$, $\rho_{M(t)}$, ρ_0 are defined the conductivity of the matrix phase, the resistivity of the matrix phase, the resistivity of the alloy, respectively. $\chi_{Zn}(t)$ and $\chi_{Mg}(t)$ are referred the concentrations of the Zn and Mg elements in the matrix phase (which is time dependent, due to precipitation that can occur), after precipitation of the precipitation-hardening elements (Zn, Mg and Cu) has been completed; $r_{Zn}(t)$ and $r_{Mg}(t)$ are constant. The precipitates grow larger, so the $\chi_{Zn}(t)$ and $\chi_{Mg}(t)$ decrease, the conductivity increases with increasing ageing time, according to Eq. (1). At higher ageing temperature, the precipitates make larger more rapidly compared to at lower ageing temperature, therefore the conductivity raises sharply than at lower ageing temperature. So, the conductivity is higher at 160 °C as regards to at 120 °C at the same ageing time (Zang et al., 2012).

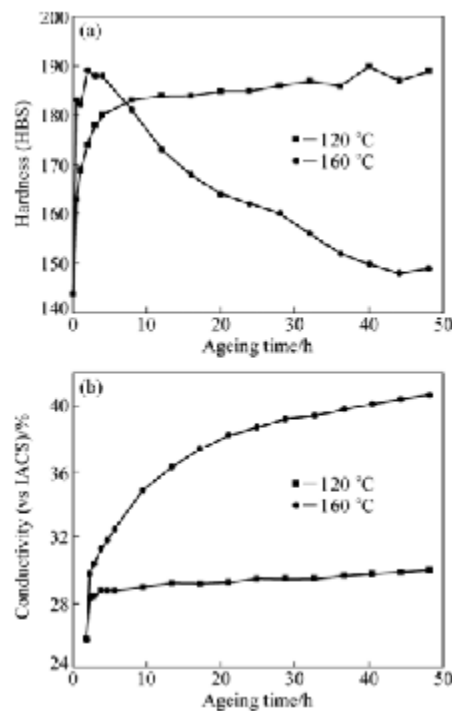


Figure 2.12. Evolution of ageing temperature on hardness (a) and conductivity (b) of studied alloy (Zang et al., 2012).

Liu et al. studied the mechanical and electrical properties of the hot-rolled aluminum plate, with compositions (mass fractions) of Zn 7.5%, Mg 1.7%, Cu 1.4%, Zr 0.12% and Al balance.

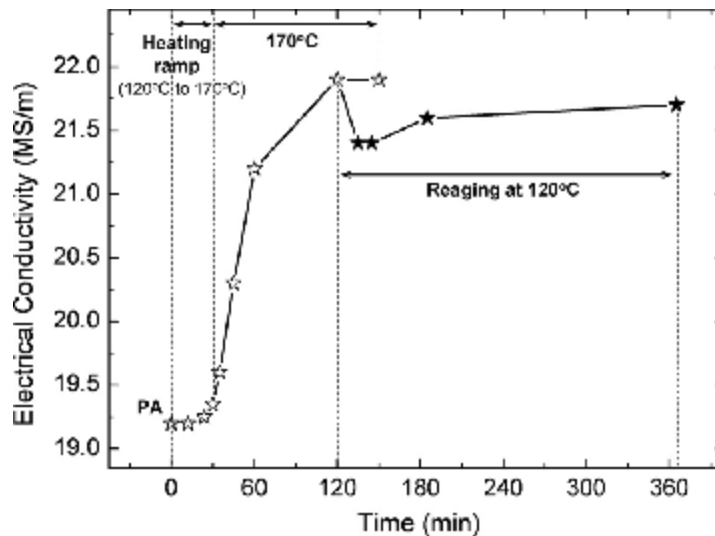


Figure 2.13. Changing variation of electrical conductivity during retrogression (open diamonds) and reaging (solid diamonds) treatments of the alloy (Liu et al., 2014).

They observed the qualified of the retrogression with a rapid dissolution stage at almost constant average precipitate size, pursued through a coarsening stage with raising precipitate size and volume fraction and a minor increase of the electrical conductivity, throughout the heating slope from 120 to 170 °C. Authors revealed the increasing electrical conductivity with the reducing time, after retrogression at 170 °C. As a known, the electrical conductivity functionates as an indicator of SCC resistance. This indicator acts a role on the raising with increasing electrical conductivity in Al-Zn-Mg-Cu alloys.(Liu et al., 2014).

As a known, heat treatment process possesses big effect on microstructure and conductivity of the ingots, and to evaluate corrosion resistance, the conductivity is a good route. Gaosong et al. produced the ingots of high strength 7075 aluminum alloy via low frequency electromagnetic casting(LFEC) and studied the effect of various homogenization processes(single-step homogenization at 465°C for various anticipation times and three-step homogenization) on the microstructure and conductivity of 7075 aluminum alloy. Authors revealed that the grains of LFEC ingot are qualified via a lower content of low melting point phases and observed the higher electrical conductivity of the ingots compared to DC ingot under the same homogenizing conditions (Gaosong et al., 2014).

2.2.2. Searching of the Electrical Resistivity of The Al-7xxx series Alloys

Ferragut et al., studied the early stages of pre-aging at near room temperature in an Al–Zn–Mg–Cu based commercial alloy via electrical resistivity. They sufficiently defined the resistivity changes in the same terms of a Johnson–Mehl–Avrami (JMA) type function. This is required for the volume fraction growth of the Guinier–Preston zones or pre-precipitate solute clusters constituted. For one specific case, authors specified the resistivity results with those acquired throughout synchrotron-radiation small-angle X-ray scattering (SR-SAXS).

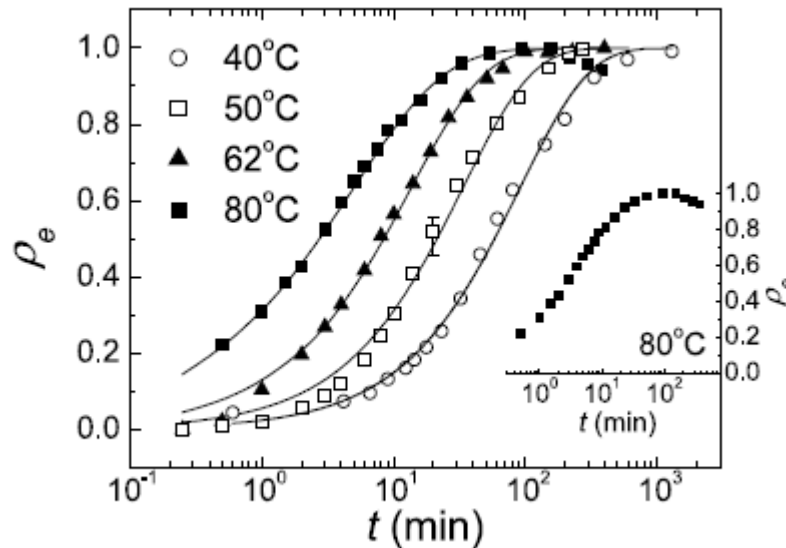


Figure 2.14. Isothermal pre-aging curves of the relative resistivity ρ_e at various temperatures for samples of 7012 alloy quenched at 470 °C.

Authors thermally treated the samples were thermally treated via : (i) in an electric air circulating furnace and water quenching at 20 °C, homogenization process for 2 h at 470 °C; (ii) pre-aging at various temperatures: 40, 50, 62 and 80 °C for various aging times (see Figure 2.14.).

As seen in The Figure 2.34, it is appeared that the evolution of the relative resistivity ρ_e acts as a function of the pre-aging time t at different temperatures. To prevent the nucleation of incoherent particles, authors selected the temperatures of

the pre-aging heat treatments of low enough at near room temperature. The relative resistivity is expressed as follows:

$$\rho_e = \frac{\rho(t) - \rho_i}{\rho_s - \rho_i} \quad (2.2.)$$

Where, ρ_i is defined the initial resistivity value after quenching, ρ_s is the maximum resistivity value and $\rho(t)$ is the measured instantaneous resistivity value.

In below equation, the relative resistivity ρ_e increase could be well stated by means of a Johnson–Mehl– Avrami(JMA) function, in the limit case of small pre-precipitates, throughout pre-aging.

$$\rho_e = 1 - \exp \left[- \left(\frac{t}{t_c} \right)^n \right] \quad (2.3.)$$

Where, the parameters t_c and n , base on the diffusion conditions and related to the change of the relative resistivity at each pre-aging temperature. Acquired n values are in suitable agreement with those procured for some Al–Zn–Mg alloys (with both high Zn and low variable Mg contents) owing to resistivity measurements under similar thermal treatments, i.e. aging at near RT after quenching. They also stated that the resistivity changes would be depended on the volume fraction growth of the generated pre-precipitate particles such as GP zones or precipitate solute clusters) (Ferragut et al., 2002; Ferragut et al, 1999).

The base precipitating phase (defined M) in 7xxx alloys is isomorphous phase to $MgZn_2$, while other phases can also nucleate on quenching(S and T phases). Grain boundary and subgrain boundaries formed at lower temperatures plays role as intergranular nucleation sites despite chromium or zirconium acting as intragranular sites. In studies, qualifying the precipitation processes in aluminum alloys it benefits from resistivity measurements. Archambault and Godard investigated the electrical resistivity of an industrial 100 mm thick plate AA7010 cast and rolled via Pechinery

Rhenalu Issorie. In their study, they developed a very sensitivity measurement method to specify the high temperature precipitation kinetics in aluminum alloys. They observed the different precipitation processes appeared throughout DSC above 200°C finding out as a single process via the resistivity measurement. This measurement supports the validity of the Mathiessen's rule in this temperature range. the resistivity variation , showed firstly a sharp reduce because of the 50°C/s cooling before holding in order to interrupt quenching and isothermal holding conditions, (Figure 2.15.). Then, it was observed the smoother and pursued through an asymptotic plateau. They discerned the raising of the resistivity variation with the reducing holding temperature.

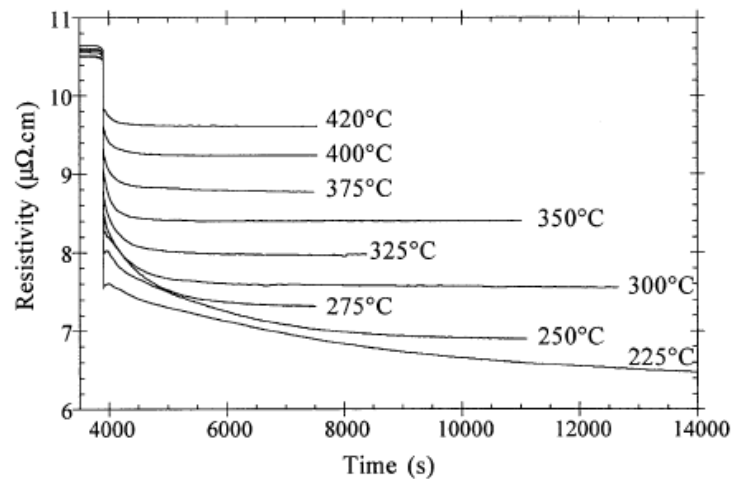


Figure 2.15. Changing of the resistivity throughout isothermal holdings then interrupted quenching from the solutionizing temperature (Archambault and Godard, 2000).

The magnitude of the precipitation relates to the decomposition temperature and on the cooling rate. They specified the precipitation kinetics for the three linear cooling rates between 475 and 200°C and acquired the similar kinetics via two techniques for the 10°C/mn cooling rate (see figure 3) and observed the pursuing the resistivity to the Matthiessen's rule over this temperature range and following the differential resistivity to the decomposition of the solid solution (Archambault and Godard, 2000).

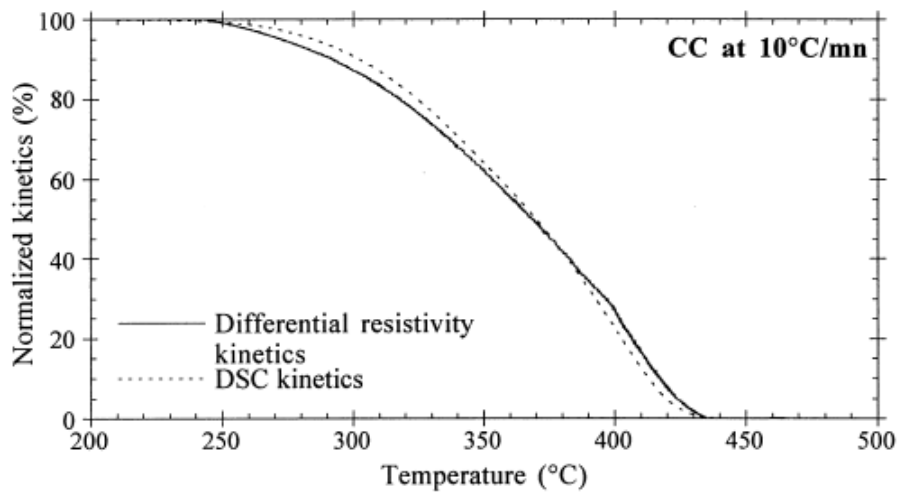


Figure 2.16. Temperature based on precipitation kinetics obtained between 475 and 200°C by DSC and resistivity measurement for the 10°C/mn cooling (Archambault and Godard, 2000).

Dellah et al. investigated the structural, electrical resistivity and hardness changes of aged Al–Zn–Mg alloys. They showed that the isothermal annealing in temperature range of 25–200 °C causes to the sequent precipitation sequence: Guinier–Preston zones $\rightarrow \eta'$ -phase $\rightarrow \eta$ -phase; and revealed the important increase of electrical resistivity (ρ) of the considered alloys relating to the stage of GP zone decomposition. It was observed that the constitution of the intermediate η' -phase was accompanied with both a decrease of electrical resistivity and an increase of hardness and found the Non-continuous quenching to suppress the η' -phase formation; spite of causing the elevated quenching rates to the formation of uniformly scattered fine precipitates in the alloy bulk (Dellah et al., 2013).

In the previous studies, It was studied the Figure of Merit and Seebeck Coefficient of Al-7xxx Series alloys, In this work, it has been searched the thermoelectric properties such as Seebeck coefficient, figure of merit accompanied with Electrical resistivity, Thermal conductivity of Alumix 431 alloy which is the Al 7xxx series alloy.

3. MATERIAL AND METHOD

3.1. Material

In this thesis work, the material used was Alumix 431[®] powder which is a mixture of Al 7xxx series aluminum alloy and obtained from Ecka Granules in Germany. The chemical composition and particle size characteristics of Alumix 431 powders utilized in this work is given in table 3.1.

Table 3.1. Typical chemical composition and physical characteristics of Alumix 431 Material

Chemical Composition,% (density 2.786 g/cm ⁻³)		Particle Size Distribution (µm)	
Al	89	D ₁₀	54.8
Cu	1.5	D ₅₀	107.2
Mg	2.5	D ₉₀	193.1
Zn	5.5	*S _w	4.7
Lubricant	1.5	Mean Value	18.2

*S_w means the particle size distribution slope.

As seen in table 3.1., the Alumix 431 series alloy is based on additions of zinc, magnesium and copper and the material is a high strength alloy. Zinc is dissoluble in aluminum, important alloying addition for Alumix 431 and supports to the precipitation hardening (Ekşi et al., 2004). A practical limit of about 8wt% Zn is implemented for traditional cast materials due to intrinsic foundry problems like solute macrosegregation and cracking (Feng et al., 2009). Copper is doped to these alloys to enhance the wetting behavior of the liquid phase of aluminum and also supports to precipitation hardening as Zinc element (Ekşi et al., 2004). Both copper containing and zinc containing aluminum alloys possess a high strength/weight ratio and have been extensively implemented in aerospace, automotive, textile engineering etc. Really, zinc effect on the strength of aluminum alloy is more important compared to effect of copper. The Al-7xxx alloys are sensitive to localize corrosion

because of the existence of strengthening phases such as $MgZn_2$, $AlMg_3Zn_2$, Al_3CuMg (Xue et al., 2007). Mg is the lightest material and indicates superior properties such as high dimensional stability and thermal conductivity, good formability and recyclability. Spite of its advantages, there is a major disadvantage of Mg element as inadequate corrosion resistance because of high reactivity. Mg and its alloys are also qualified via low hardness and wear resistance, so their useful areas are restricted to mechanical parts working under static conditions such as casing, housing (Mola , 2013). Magnesium even at 0.5% level, have positive effect on shrinkage via decreasing the oxide, permitting metal/metal contact at particle interfaces and facilitating diffusion (Ekşi et al., 2004).

3.2. Method

3.2.1. Manufacturing Method of Specimens

In this thesis work, the specimens used, were previously prepared. First of all, the components of powder (Al-5.5 Zn-2.5 Mg-1.5 Cu; elemental mixing is in weight%.) which are approximately weight of 15 g are mixed to put into blanks , together with lubricant, until a homogeneous mix is obtained using a 3-D Turbula Mixer. The specimens were compacted in a cylindrical mold of 15 mm diameter to obtain compacts of about height of 15 mm which has almost 3.5 g in weight with an accuracy of 0.001 g for static features. They were pressed up between 300 and 500 MPa pressure and specimens was applied at two various temperatures and pressing conditions; room temperature (RT), 50°C and 80°C. Warm compaction was implemented through a furnace of Heraeus, UT 12P.

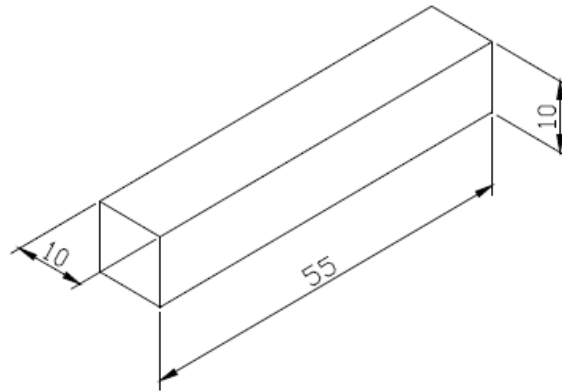


Figure 3.1. Compacted aluminium alloy used in this study.

In order to investigate the thermoelectric properties , the samples cracked so as to replace properly to probe-holder of machine as shown in Figure 3.2.



Figure 3.2. The cracked samples for measuring thermoelectric properties

3.2.2. Characterization Methods of Alumix 431 Specimens

3.2.2.1. Optical Microscope and Scanning Electron Microscope (SEM) Characterization Methods

In both optical and Scanning Electron Microscope (SEM), preparation of sample is important. Firstly, the specimens are cut and grinded to size and polished the surface to subject to the features. These steps are widely defined as metallography.

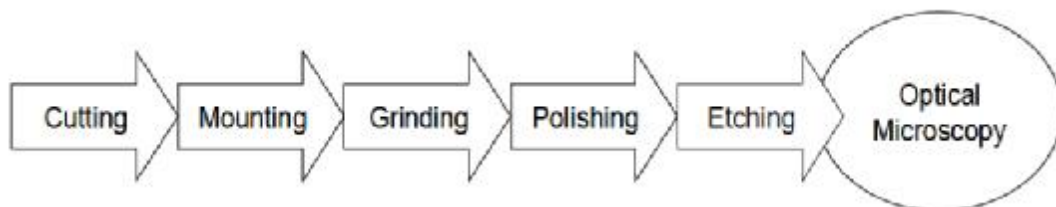


Figure 3.3. Specimen preparation steps for Optical Microscopy and SEM (Dilek, 2006)

In optical microscopy, the probing beam is light; this is reflected off or conveyed via sample before the image of specimen occurs. The image is generated by opposed among various properties of sample. This features such as brightness, phase, colour, polarization, fluorescence base on the illuminating source. Magnification is checked via a system of optical lenses. Resolution restriction is normally lined off throughout the light wavelength or maximum magnification value will be enhanced any significant contrast.

In Scanning Electron Microscope (SEM), the observing of electrically insulating material occurs via electrically isolated sample' surface, when bombarding with electrons. This case causes to a charge build-up on the samples, this makes either imaging or other analysis hard.

The morphology and microscope examinations of pressed samples have been done by light (Leica DMRX) and scanning electron microscopy (LEO 1530 GEMINI).

3.2.2.2. Density Measurements of Alumix 431 Specimens

Density of samples were measured by Classical Method and the Archimedes Principle (water displacement technique) using Presica 320XT series for analytical and precision balances which has 1/10000 precision of scale in Gazi University's Mechanical Research Laboratory in Ankara, Turkey. Archimedes Principle is simple to implement, experimental results can be reckoned rapidly., Precisa Density Measurement Set is also used, so as to measure densities by Archimedes Principle. This set specially produced with this balance includes of liquid tube carrier table, specimen holder, glass liquid tube and fitted temperature for liquid. Pure water is used for measuring media at room temperature, 22 °C for this study.

According to Classical Method and Archimedes Principle, there are a lot of the basic formulas related to density. These are given with symbols and explanations to determine densities of samples below:

a) Classical Method to determine the green density

ρ_{green} = Green density of specimen, g / cm³

m_{green} = Green mass of specimen, g

V_{green} = Green volume of specimen, cm³

$$\rho_{\text{green}} = m_{\text{green}} / V_{\text{green}} \quad (3.1.)$$

b) Archimedes Method to determine the sintered density

x = Weight of specimen, g

y = Carrier material weight, g

z = Weight of specimen in the water, g

b = Difference of weight, g

a = Weight without carrier bond, g

ρ_{sintered} = Sintered density of specimen, g / cm³

k = 0,9999 (special constant for pure water at 18-26 °C temperature from handbook of the density measurement set)

$$a = z - y \quad (3.2.)$$

$$b = x - a \quad (3.3)$$

$$\rho_{\text{sintered}} = k.x/b \quad (3.4)$$

The densities have been calculated easily with the help of these equations to compare used all data in connecting with density in this work.

3.2.2.3. Measurement of Thermal Transport Properties Of Alumix 431 Specimens Via The Physical Properties Measurement Systems (PPMS)

For physical features such as heat capacity, magnetization, magnetic torque, Hall effect, DC-resistivity and other thermal and electronic properties of a specimen, the PPMS produced by Quantum Design, is various temperature field systems. The system permits automated measurements. The magnetic field can be installed to 9 T and the temperature interval ranges from 1.8 to 400 K or down to 0.4 K with a Helium 3 refrigerator(Figure 3.5-13).



Figure 3.5. The PPMS of Model 6000 PPMS Machine.



Figure 3.6. The Model 6000 Controller of Model 6000 PPMS Machine.



Figure 3.7. The NMR Apparatus and PPMS head of Model 6000 PPMS machine.



Figure 3.8. Samples prepared to examine the thermal-transport properties.

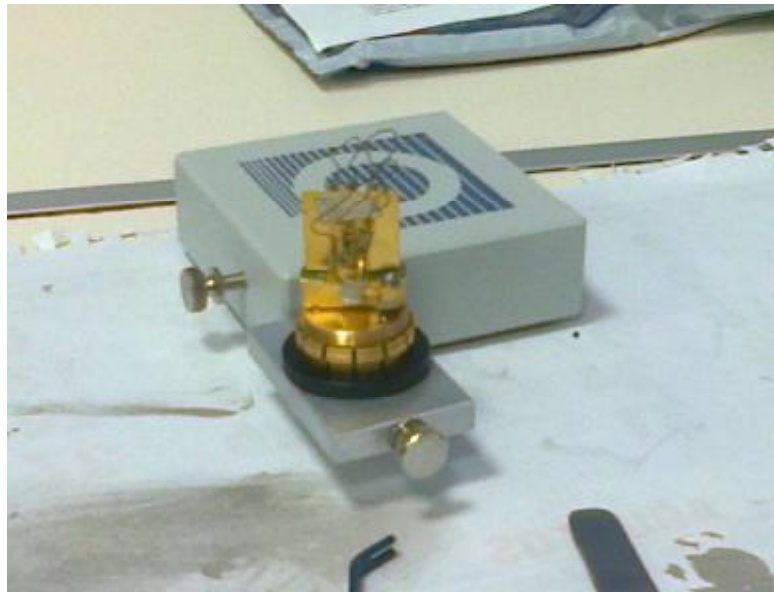


Figure 3.9. Sample-holder of PPMS machine.

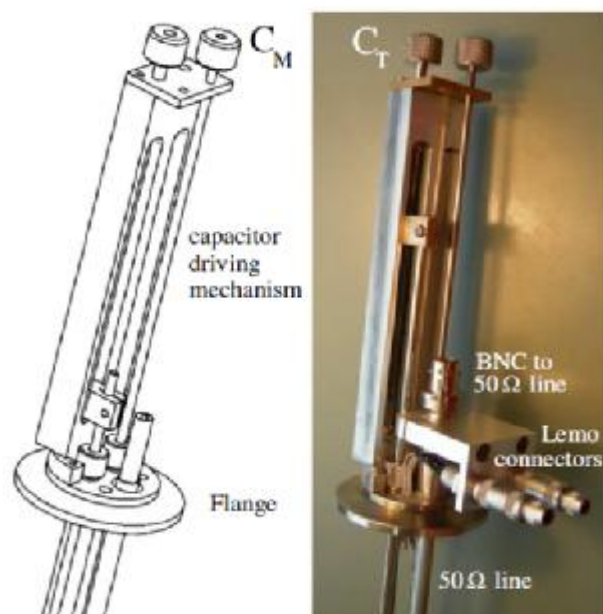


Figure 3.10 . The upper part of the NMR probe head (Gafner, 2006).

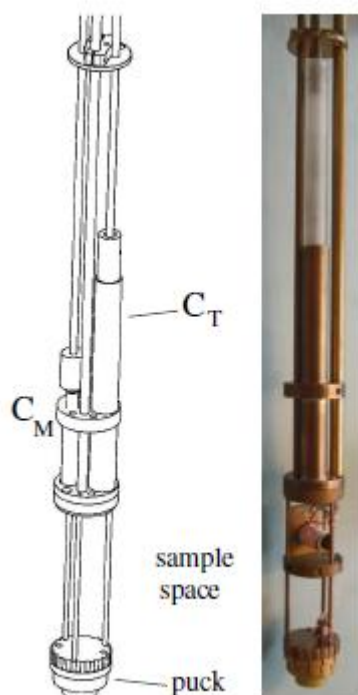


Figure 3.11. The bottom part of NMR probe head (Gafner, 2006).



Figure 3.12. The NMR probe head (Gafner, 2006).

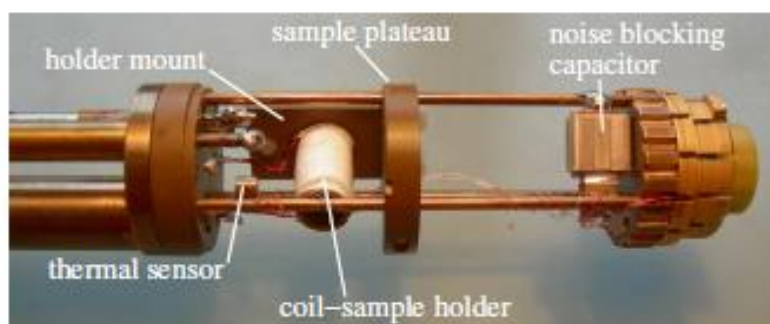


Figure 3.13. The sample holder, plateau, thermal sensor and noise-blocking capacitor (Gafner, 2006).

The system can be exactly checked and displayed via either the model 6000 controller or MultiVu software running on PC. Simple sequence script can be written with MultiVu software, so as to allow the PPMS work fully automatized.

The high capacity nitrogen jacked thermos hampers fast liquid helium evaporation loss. The PPMS interpolate with the superconducting magnet is submerged in liquid helium. The outer layer of the insert is a superconducting magnet. The magnet is made of NbTi / Nb₃Sn. In order to adjust the magnetic , there are three modes; the oscillating mode, the no-overshooting mode and the linear mode. The no-overshooting and the linear modes culminate in a field drift whereas

the oscillating mode is almost stable. The uniformity of field is insisted to $\pm 0.01\%$ over a (5.5×1) cm cylindrical volume with the center at 5.1 cm above the puck surface.

In order to check the temperature of PPMS proposes the high temperature control and the continuous low-temperature control techniques. These permit a fast cooling and heating of the PPMS specimen surface, a smooth transition through the 4.2K helium boiling point and continue mistily a temperature below 4.2 K (Gafner, 2006).

For the Physical Property Measurement System (PPMS), the Quantum Design Thermal Transport option (TTO) allow measurements of thermal properties, such as thermal conductivity κ and Seebeck coefficient (also called the thermopower) α , for sample materials over the entire temperature and magnetic field range of the PPMS. In the measurement of thermal conductivity, the TTO system is occurred via by monitoring the temperature drop along the sample as a known amount of heat passes through the sample and in the measurement of thermoelectric Seebeck effect, the system is carried out as an electrical voltage drop that come along a temperature drop across certain materials. These two measurements are implemented concurrently throughout monitoring both the temperature and voltage drop across a sample as a heat pulse is performed to one end, via The TTO system. The system can also measure electrical resistivity ρ throughout the standard four-probe resistivity enhanced via the PPMS. AC Transport Measurement System (ACT) option (Model P600). In order to specify the so-called “thermoelectric figure of merit,” $ZT = \frac{\alpha^2 T}{\kappa \rho}$, all three measurement types are important. The figure of merit is usually stated as the dimensionless quantity $Z \times T$, where $Z \times T \sim 1$ is a common consideration for viability of a material for thermoelectric applications.

Table 3.2. System Requirements for the Thermal Transport System

Component	Function
PPMS Resistivity Option (Model P400)	Enhancing user bridge board that reads two thermometer shoes.
PPMS AC Transport Measurement System (Model P600)	Outputs current to heater and sample while providing low-noise, phase-sensitive detection
PPMS High-Vacuum Option (Model P640)	Provides thermal isolation for measurements. Cryopump or Turbo Pump may be used
PPMS MultiVu Software Version 1.1.6 or Later	Provides single user interface for PPMS and PPMS options.

Table 3.3. Thermal Transport System Parameters

Parameter	Value
Pressure	High vacuum ($\sim 10^{-4}$ torr)
Temperature	1.9–390 K
Magnetic field	0–14 T when $T > 20$ K

Measurement Modes: The TTO system involve two measurement modes; (i) continuous measurement mode and (ii) single measurement mode. Measurements of all properties proposed via TTO can be applied in either of these two modes.

In continuous measurement mode, to optimize the measurements, measurements are being taken progressively and the adaptive software is setting parameters (such as heater power and period). This mode is depended on slow sweepings of system variables such as temperature or magnetic field, and it is often the most rapid way of obtaining. via the use of a complicated curve-fitting algorithm the continuous mode is also speed up. The algorithm specifies the steady-state thermal properties throughout estimating from the response to a relatively short (typically several minutes) heat pulse.

In the single measurement mode, mode is operated slower than continuous measurement mode because of its requirement that reached of the system to a steady state in both the heater “off” and “on” states, The advantage of single measurement mode is necessity of no subtle curve-fitting calculations , therefore remark of the raw data is more obvious..

Measurement of Thermal Properties: The TTO system is adjusted to measure four thermal transport properties:

- Thermal conductivity
- Seebeck coefficient
- Electrical resistivity
- Thermoelectric figure of merit

The thermoelectric figure of merit, which is the algebraic combination of these three measurements, can be calculated ,when thermal conductivity, Seebeck coefficient, and electrical resistivity are all measured.

Thermal Conductivity: The TTO system measures thermal conductivity κ via implementing heat from the heater shoe so as to occur a user-determined temperature differential between the two thermometer shoes. In terms of the thermal response of the sample to the low-frequency, square-wave heat pulse,The TTO system dynamically is been model, thus speeding up data acquisition and TTO system can be reckoned thermal conductivity directly from the implemented heater power, occurring ΔT , and sample geometry.

Seebeck Coefficient: the Seebeck coefficient (also called the thermopower) α specified The TTO system via occurring a determined temperature drop between the two thermometer shoes. However, the voltage drop created between the thermometer shoes is also monitored for Seebeck coefficient measurement. these thermometer shoes caused to the additional voltage –sense are connected to the ultra-low-noise preamplifier of the ACT system.

Electrical Resistivity: The TTO system measures electrical resistivity ρ via using both a precision DSP current source and phase-sensitive voltage detection. For

this AC resistivity measurement, the specifications are importantly identical to those for the AC Transport Measurement System (ACT) option.

Figure of Merit: The dimensionless thermoelectric figure of merit ZT is determined here simply as the algebraic combination $ZT = \alpha^2 T / \kappa \rho$ of the three measured quantities—thermal conductivity.

In this thesis work, Model 6000 Physical Property Measurement System , Quantum Design machine was utilized to measure the thermal transport properties such as electrical resistivity, thermal conductivity, Seebeck coefficient and figure of merit. Specimens measured in this machine were cut so as to replace properly to probe-holder of machine.

4. RESULTS AND DISCUSSIONS

In this study, the thermoelectric properties of alumix (431) (Al-5.5 Zn-2.5Mg-1.5Cu) prepared on different pressures and temperatures have been investigated. It was examined Optical microscope, SEM images and density measurements of specimens for their structural properties and searched the electrical resistivity, thermal conductivity, Seebeck coefficient, the dimensionless figure of merit (ZT) data obtained from PPMS Quantum Design (Physical Property Measurement System) at measured temperature ranges 5-300 K for their thermoelectric properties.

In this study, the samples prepared on different pressures and temperatures were symbolized 1, 2, 3, 4, 5, 6

Alumix 1	350MPa, RT
Alumix 2	350MPa, 50°C
Alumix 3	350 MPa, 80°C
Alumix 4	400MPa, RT
Alumix 5	400MPA, 50°C
Alumix 6	400MPa, 80°C

4.1. Analysis of Optical Micrographic Figures of Alumix (431) 1, 2, 3, 4, 5 ,6 Specimens

In Figures 4.1, and 4.2, the badge microstructure of primary α -Al solid solution turned round via inter-dendritic secondary phases and some grain boundary precipitates having laminar morphology was shown. It was observed that the microstructures have the eutectic characteristic structure. In the microstructure, it is considered the existence of the coarse eutectic phases relating of the high amount of Zn, Mg and Cu in the alloys and low cooling rate linking to the traditional solidification process.

Figures 4.1 and 4.2 show the microstructure of Al-5.5Zn-2.5 Mg-1.5Cu alloy comprised of the both equiaxed grains and some fine secondary phases. The existence of the equiaxed grain morphology is considered to result from the high cooling rate, related to the rapid solidification processes. On the contrary, the existence of coarse eutectic phases in the IM counterpart processed traditionally was repressed.

In this Figures 4.1 and 4.2, it is also shown that second phases having both the grain boundaries and in the grain inners. The second phases in the grain inners reveal different shapes such as needle and square microstructure shape of particles. Along the matrix, most of the second phases is the comparative uniformly dispersed and it is sighted the some of the grain boundary precipitates possessing an allotriomorphic morphology (Feng et al. 2009)

The concentrated second phases have eutectic precipitated from the liquid phase directly at grain boundary. The distributed gray phases within the grains are mostly the strengthening phase (MgZn_2). The phase is precipitated from solid based body. In the microstructure, it was observed the some tiny pores. The pores decrease by the mechanical properties.

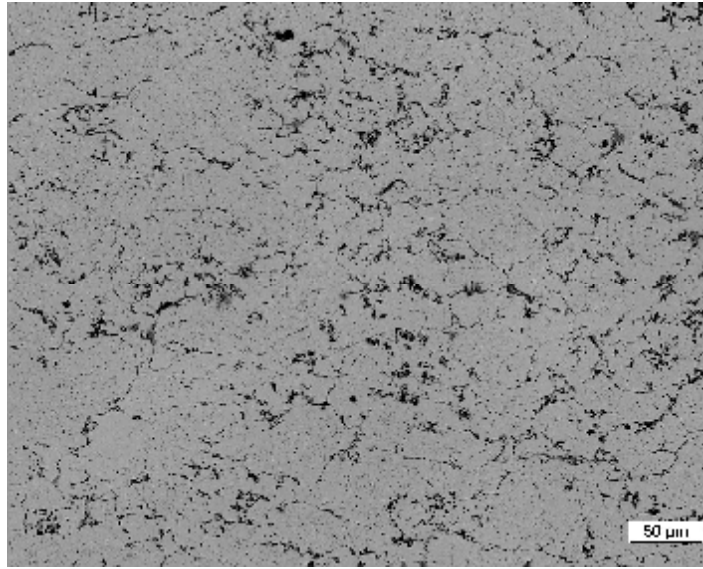


Figure 4.1. Optical microscope image of alumix (431) sample (50µm).

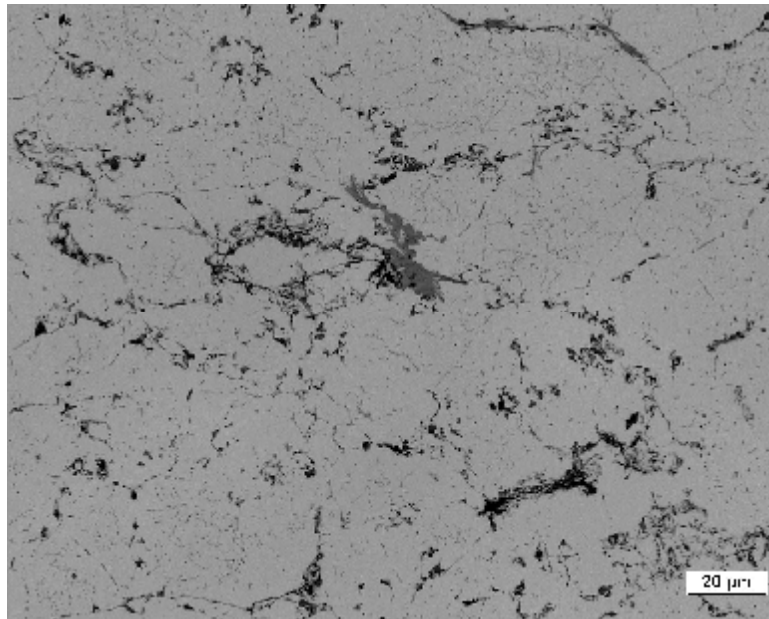


Figure 4.2. Optical microscope image of alumix (431) sample (20µm).

The cracks near the crack source zone of the fracture are intergranular microstructure. Course of events of deep into certain depth, the cracks transits into transcrystalline. Some coarse particles were sighted on the surface of the specimens. This case manifests the fatigue damage (see in Figure 4.3.) (Hai-Gen et al., 2009).

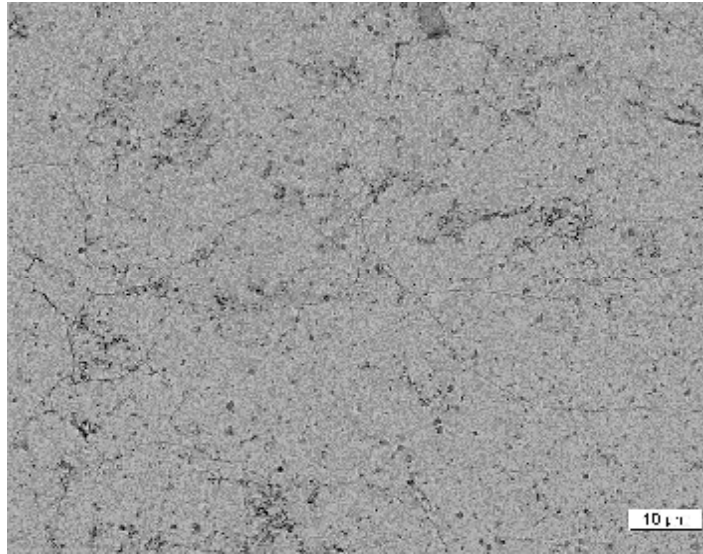


Figure 4.3. Optical microscope image of alumix (431) sample with transactions (10 μ m).

In the figure 4.4., it is observed that an equiaxed grains and two types of phases with apparent origins. The first one is the phase occurred at the grain boundaries throughout the solidification process led by the segregation of the alloying elements. The other phase is commonly constituted near the grain boundary. This case resulted from coring leading precipitation. Many coarse precipitates are apparent within the constituted grains (Mazzer et al. 2013).

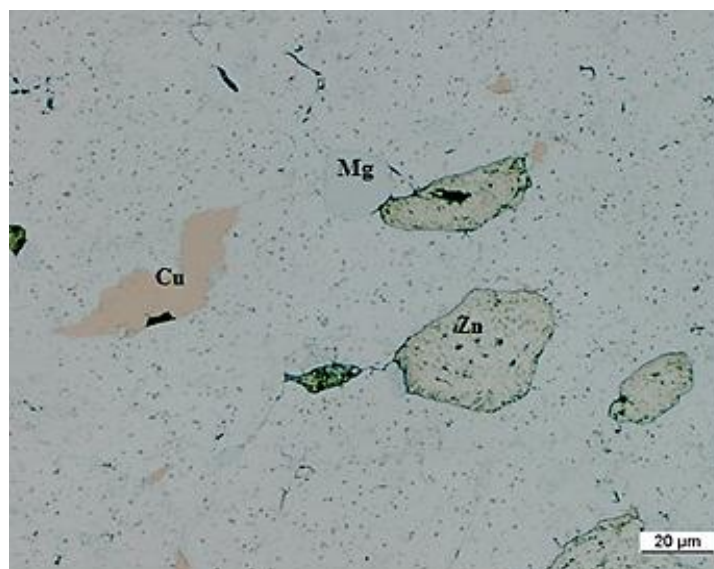


Figure 4.4. Optical microscope image of alumix (431) sample with materials (20 μ m).

4.2. Analysis of SEM Figures of Alumix (431) 1, 2, 3, 4, 5, 6 Specimens

Figures 4.5-8 present the fracture surface of the samples. Many fine holes specified ductile resulted from fracture can be observed. Holes caused from the aged sample treated smaller than the solution heat treatment. It manifests the precipitated particles have affected the fracture occurred. At the grain and subgrain boundaries, the smaller holes are constituted because of the existence of the equilibrium η phase at these regions. This phase decrease the plastic deformation at the zone and the following plastic flow around the precipitates (Mazzer et al. 2013).

The precipitation behavior in α -Al matrix is related to the mechanical properties sized such as the ductility change and strength of various hot deformation treatments linked to size, dispersion and volume fraction of the precipitated second phases. It is observed the transgranular microstructures and fine holes with secondary cracks, in the figures. This case means the undissolved coarse phases caused to stress concentration. This stress concentration occurs in the constitution of the secondary cracks in the matrix and worsening influence on the ductility (Jia et al. 2012).

Deep and fewer holes were observed. The holes caused from including of secondary phases. It is considered the fracture of precipitates induced to the fracture. Naturally aged joints showed the fracture surface surrounded with deeper and larger holes besides few flat zones. Some deep hollows can be observed on the surface of the fracture (Figures 4.5-8) (Sharma et al. 2013).

The surface of fractures showed the mainly cup-cone holes with changing and no such intergranular cracks are seen. This case is explained the ductile fracture, non-similar intergranular brittle failure (Rout et al. 2014).

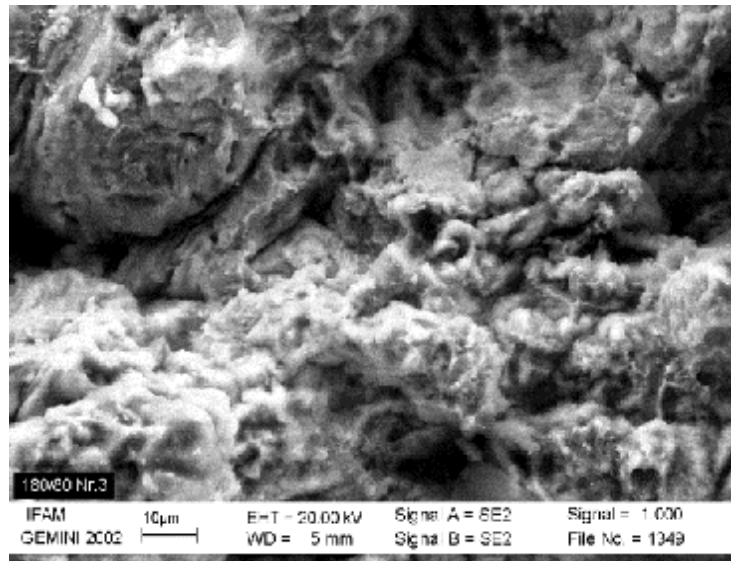


Figure 4.5. SEM image of Alumix (431) sample prepared under the 180MPa and 80° conditions(10µm).

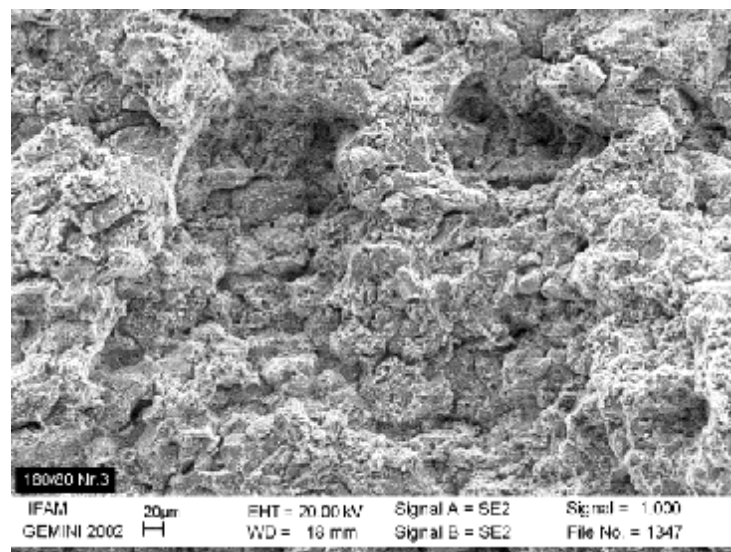


Figure 4.6. SEM image of Alumix (431) sample prepared under the 180MPa and 80° C conditions (20µm).

4.3. Density Measurements of Alumix 431 Specimens

The results of the density measurements of Alumix 431 indicates the highest density on compacted specimen at 400MPa/RT. It was observed the decreasing porosity and homogeneous structure with increasing temperature. This case is shown that the density was influenced directly with decreasing porosity and shrinkage of pores was generated because of reducing of volume of sintered parts and non-varied weight. Therefore, these conditions increased the density. High density is resulted from high strength of sintered parts and high density also influences mechanical properties such as strength, toughness and hardness. For this reason, high density property is a desirable feature (İynen et al., 2010)(Figure 3.1-2).

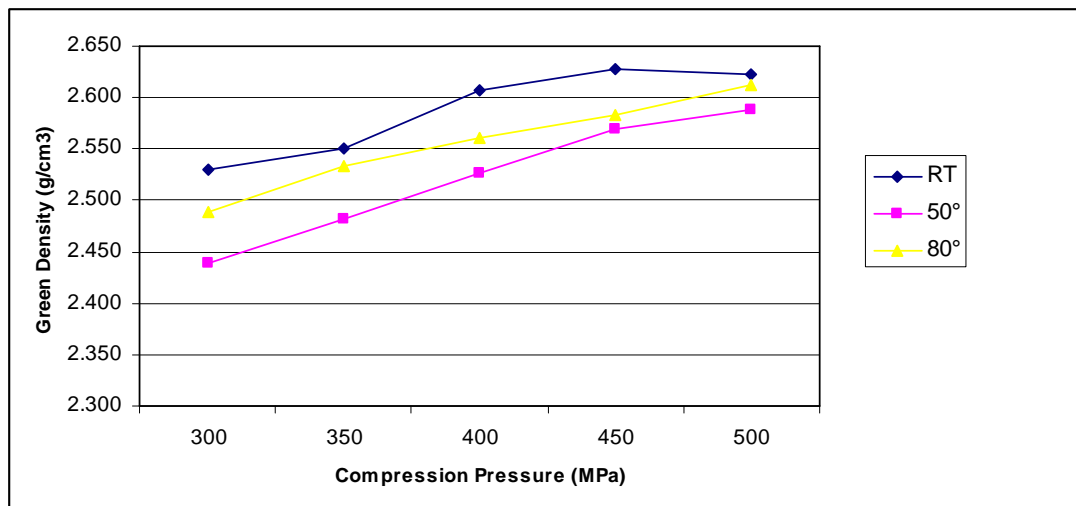


Figure 4.7. The green density (g/cm^3) changes of Alumix 431 samples related to compression pressure(MPa)(İynen,2009).

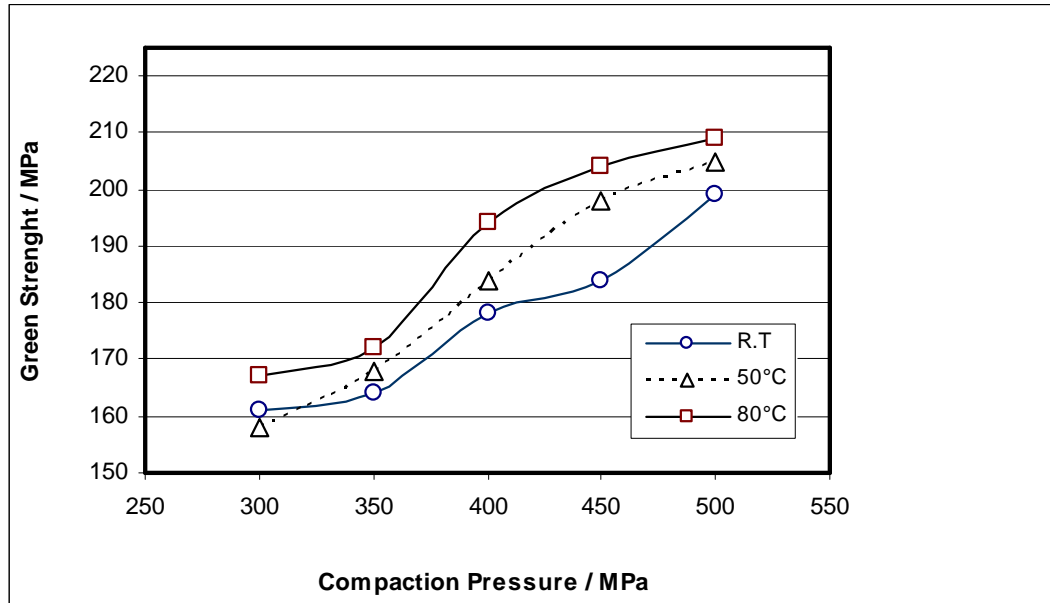


Figure 4.8. Relationship between the compaction pressure and green strength of the samples prepared in three various compaction temperatures (İynen,2009).

4.4. Analysis of Electrical Resistivity Results of Alumix (431) 1, 2, 3, 4, 5, 6 Specimens

Electrical resistivity is a significant feature related to material, and is generally dependent upon the temperature. At room temperature, ρ value is representer of if a material is an insulator (ρ is on the order of $10^6 \Omega\text{m}$) or a metal (ρ is on the order of $10^{-6} \Omega\text{m}$ or less). Among the metal and insulator orders, semiconductor materials' resistivity values are low from materials. For the thermoelectric material the optimum electrical resistivity range is varied from 10^{-3} to $10^{-2} \Omega\text{m}$.

In metallic compounds, the analysis of the electrical resistivity related the temperature is an effective tool to acquire knowledge related the main features of these materials.

Alumix 1 is a the best material according to the other materials over 230K and ρ is roughly constant and the size and temperature related of ρ in the material is like to sighted in wicked metals or heavy added semiconductors (electrical resistivity of $0.13482 \Omega\text{m}$ at 230 K) indicated as figure 4.7. Also the decreases show the specifial metallic behavior of the alumix 431 systems.

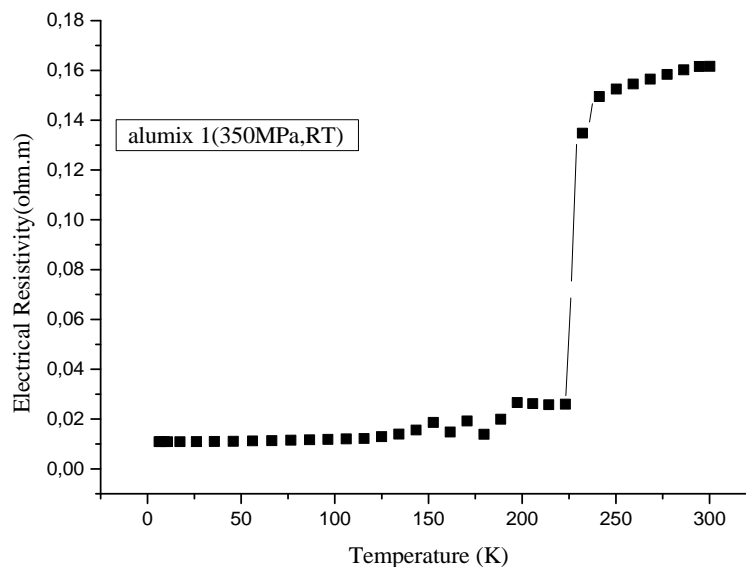


Figure 4.9. The Resistivity –Temperature graph of alumix(431) 1

For alumix 1 specimen; such a tendency is ascribed to a falling offset of E_F from the valley of the pseudogap. E_F moves to the location with larger density of states (DOS) leading to the decreasing in the electrical resistivity magnitude. The sample also indicates reducing of the same tendency with an inceptive step. The explanation for this case can be related to electrical conductivity that is electrical conductivity is based on the degree of texture; the conductivity increases with the increasing of the texture strength.

In the Figure 4.7., the sharp rise was exhibited. This case was considered to originate the impurity phases developed in the base matrix and weak inter-granular matchup. Development of both impurity phases and constitution of weak matchup among the impurities and alumix 431 grains acts a significant role in reducing the transition temperature (T_c) and increasing in the normal state resistance. As a result of in the figure the linear increase is means to a metallic behaviour down to transition temperature (T_c) (Aksan et al. , 2006, 2007).

For alumix 3 sample, the $\rho(T)$ relation of alumix 3 system, nearly resembles nonmagnetic amorphs alloys with Pauli paramagnetism of conductivity electrons. Also, in the graph in Figure 4.8. , at 225-275 K, this case is explained that on the electrical resistivity, both the constitution and resolution of η' phase and the constitution of η phase possess a powerful effect. This effect is more than inclined via the development of Guinier – Preston (GP) zones. The development is based on the a small peak centered at 225 K. The reason for this result may be less in flaws' concentration and sprinkling because of the slow cooling process. The process is required for the constitutions of the GP zones. The linear increase of alumix 3 specimen shows the favorable action inside the Baym-Meisel-Cote theory that regards the inelastic electron-phonon reaction. Below the Debye temperature θ_D , at temperatures, for the electron transport this case is important (Figure 4.8.).(Smontara et al., 2007)

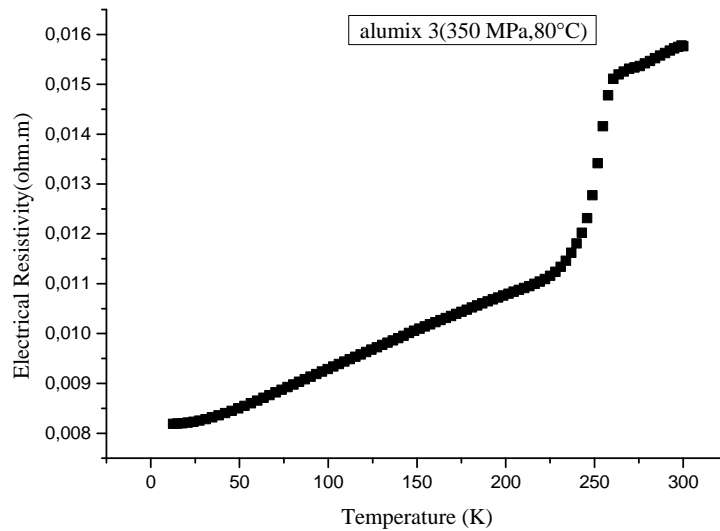


Figure 4.10. The Resistivity –Temperature graph of alumix(431) 3

In alumix 1, 3, 4, 6 samples, it is indicated that an abrupt jump in similarity of the structural transition at different temperatures. With respect to resistivity magnitude, in agreement with behavior indicated via thermoelectric power. Alumix 431 samples is reckoned through hole transport, as proved via positive sign of the Seebeck effect. (see Figure 4.7-10)(Carlini et al., 2014)

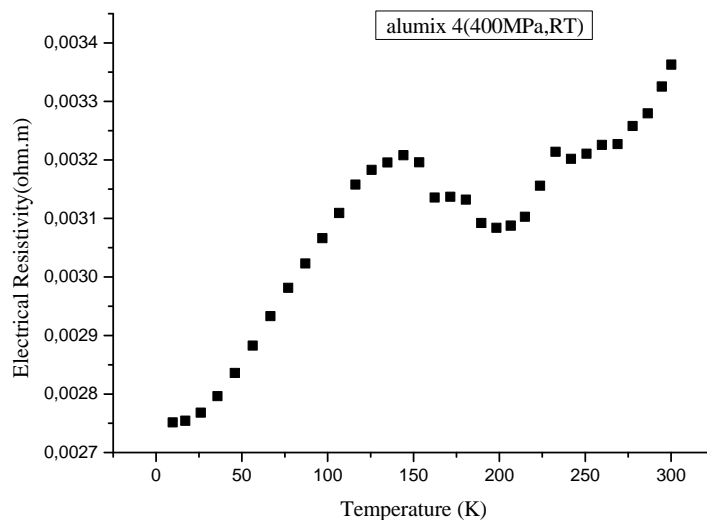


Figure 4.11. The Resistivity –Temperature graph of alumix(431) 4

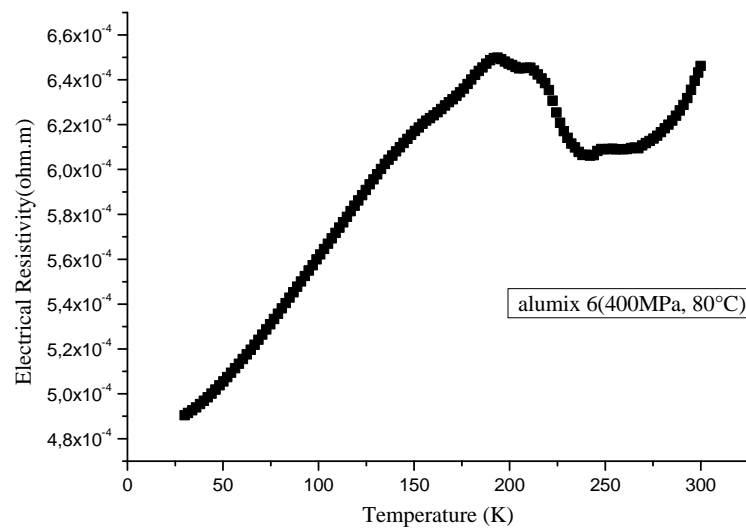


Figure 4.12. The Resistivity –Temperature graph of alumix(431) 6

In alumix 1(25-225K) (Figure 4.7.), alumix 2(5-300K) (Figure 4.11) alumix 6(at 30-195K), (Figure 4.10.), alumix 5(at 10-180K) (Figure 4.12.), alumix 4(25-115K) (Figure 4.14), (Figure 4.15) specimens, the resistivity values rise from 8.2×10^{-4} to 1.1×10^{-3} for alumix 1, from 0.0217 to 00445 for alumix 2; from 2.7×10^{-4} to 3.2×10^{-4} for alumix 4, from 4.72×10^{-4} to 7.60×10^{-4} for alumix 5; from 5×10^{-4} to 6.5×10^{-4} for alumix 6. The increases exhibited the consistent of the electrical resistivity hoped for a degenerate semiconductor; increasing with temperature, probably because of acoustic phonon spreading. (Figure 4.11.) (Tsujii et al., 2011).

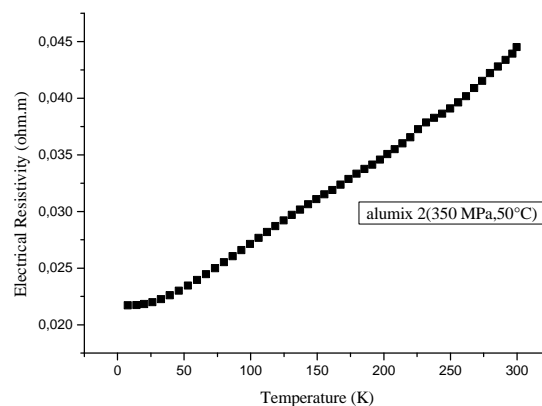


Figure 4.13. The Resistivity –Temperature graph of alumix(431) 2

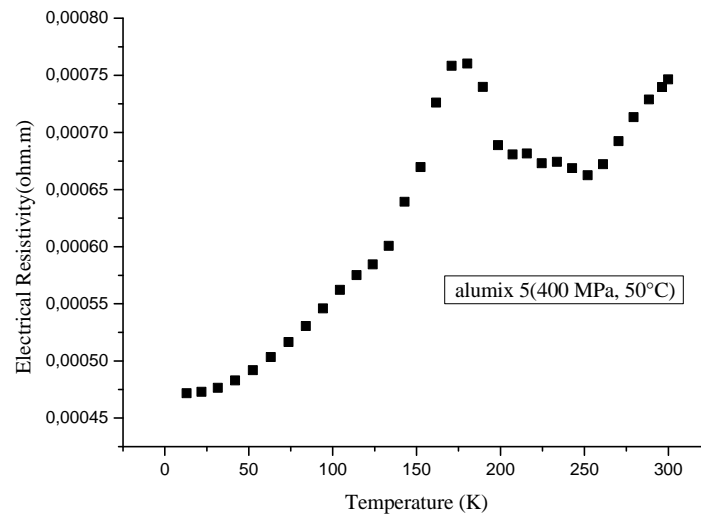


Figure 4.14. The Resistivity –Temperature graph of alumix(431) 5

In alumix (431)4, 5, 6 samples, the graphs (Figure 4.9-11) are signed the A, B, C, D, E, F characters. The characters are stated the properties of alumix 431 systems whether the solutions, transitions, diffusions or not. AB, BC, CD, DE, EF are defined the a metallic transition because of spreading of electrons from isotropic centres, a semi insulating transition is commented as the constitution of either electron hole drop (EHD) or quantum well, semi metallic transition because of anisotropic spreading of electrons from gap or cracked sites, metalloid diffusion transitions and semi metallic diffusion (both are referred the a hybrid transition) respectively(Gormani et al., 1995).

In alumix 4 (144-189K) , alumix 5(at temperature range 180-207 K) alumix 6(at temperature range 210-245K), , the decreases in alumix (431) systems is clarified lowers the resistivity of from $3.2 \times 10^{-4} \Omega\text{m}$, $7.60 \times 10^{-4} \Omega\text{m}$ $6.457 \times 10^{-4} \Omega\text{m}$, and to $3.0923 \times 10^{-4} \Omega\text{m}$ $6.807 \times 10^{-4} \Omega\text{m}$, 6.0657×10^{-4} , respectively, and produces a metallic conductors shown in Figures 4.1-14. These observings show that within these temperature ranges, there is a composition attribute that obtains semiconducting features while metallic behavior is sighted on both sides of these ranges.

In the decreases of the alumix (431) 4, 5, 6 systems, the temperature related to mobility presents that the $\mu \propto T^{-3/2}$ expression and the acoustic lattice scattering is

the predominant mechanism. Therefore, the increase in ρ at low temperature is clarified via the decrease in mobility with the increasing the temperature and the decrease is also explained conduction happens due to their band gap. The peaks also related with the sequence of the constitution and resolution of metastable phases(Tani and Kido, 2008).

In these materials the electrical resistivity values is based on the precipitation process of Al-Mg-Cu phases and their slight increases with a further increases in the temperature can be ascribed to the reducing amount of Al-Mg-Cu types precipitates in the alumix 431 structures at temperature ranges from 25 K to 200K, 175K, 180K respectively. These changes are rapid after 275K, 265K, and 285K respectively, as the resolution process dense, when Al-Mg-Cu type precipitates are no more stable. After 300 K, electrical resistivity value reaches the maximum value as the resolution of the alloying elements is rounded around. For alumix 1, 4, 5 samples gives the values of resistivity $6.46 \times 10^{-4} \Omega m$, $7.465 \times 10^{-4} \Omega m$ and $3.4 \times 10^{-4} \Omega m$ respectively.

4.5. Analysis of Thermal Conductivity Results of Alumix (431) 1, 2, 3, 4, 5, 6 Specimens

A high quality thermoelectric material must be required both a high electrical conductivity and a high thermopower and a low thermal conductivity as explained introduction section. The first two are specified via the electronic properties of the material, these are comprised into the quantity $PF = \alpha^2 \sigma$ defined to 'power factor'.

As a known, the thermal conductivity is stated with Wiedemann-Franz law expression; $\kappa = \kappa_e + \kappa_l$; in this expression; κ_e is transporting heat of carriers (electrons and holes), κ_l is expressed the travelling of phonons via the lattice. The thermoelectric figure of merit can be maximized through maximizing the electrical conductivity and minimizing the thermal conductivity. Increasing of the electrical conductivity both generates an increase in the electronic thermal conductivity and reduces the thermopower.

Increasing of ZT value through the decreasing of both κ , and the lattice contribution to the thermal conductivity. The most significant factors acts role; i) utilizing of compounds ii) the existence of heavy atoms weakly linked to the structures iii) the presence of inclusions and/or impurities iv) the solid solutions' constitution, v) the presence of a large number of grain boundaries (Elsheikh et al., 2014).

In all the alumix (431) specimens, the increases in the thermal conductivity can be considered to originating because of mainly the changes in lattice component term (κ_{ph}) (Demirel et al., 2014). Also these increases could be occurred because of the rapid reducing in electrical resistivity and accordingly strong increasing in the electronic thermal conductivity component κ_e (Gloria et al., 2013). Commonly it is ascribed to the porosity influence. High thermal conductivity was caused to low porosity position. In spite of that the thermal conductivity was increased with large grain size. This case is occurred because of decreasing grain boundary spreading of phonons (He et al., 2007).

For decreasing of all alumix 431 systems; the decreasing of κ originated the mass-variety scattering in the lattice of the alumix systems (Mikami et al., 2009). The Wiedemann-Franz law depend on the validity of the same the electron mean free path only at the low temperature for electrical and thermal transition. At low temperature, via flaws and impurities, the base electron spreading mechanism is elastic spreading mechanism. These low values show that electrons' elastic scattering acts the important role through impurities and flaws at room temperatures (Carlini et al. 2014). Stronger phonon scattering was caused to the lowest thermal conductivity (Pan et al., 2010).

For all the samples, it was indicated that increases firstly and then decreases at final measured temperature. This case results from the decreasing of thermal spreading at low temperatures. as the phonon free path is taken after to crystal site distance, the maximum κ value happens (Kuo et al.2012).

For figure 4.13 and 4.14; in alumix 5, 6 samples, at 250-300K, it was exhibited the rising from 7.29 W/Km to 7.83 W/Km for alumix 5; from 17.806W/Km to 18.720W/Km for alumix 6,. To state of the origin of such a rapid

increasing of κ , two mechanisms can be proposed. One mechanism attributed to the increase of phonon mean free path electrons intensify into the copper pairs. Other alternative mechanism ascribed to the electron contribution. The rapid increase of κ below transition temperature (T_c) indicates improvement of the quasiparticle contribution the heat conductivity and increase of the quasiparticle mean-free path. The κ (T) reduced in magnitude and the location of maximum offsets against lower temperatures. The irregularities caused to impurities flaws act as a important role in restricting the heat transport because of a strong increase of the electron-phonon impurity spreading rate (Aksan et al. 2007).

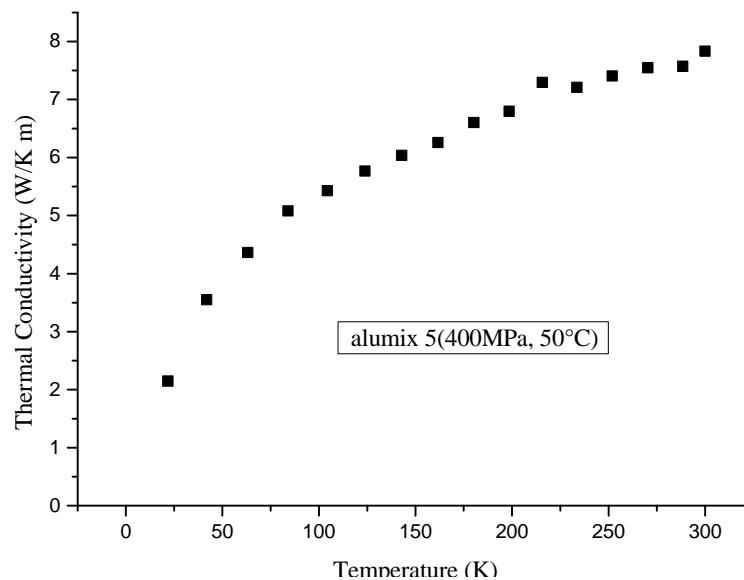


Figure 4.15. The thermal conductivity –Temperature graph of alumix(431) 5

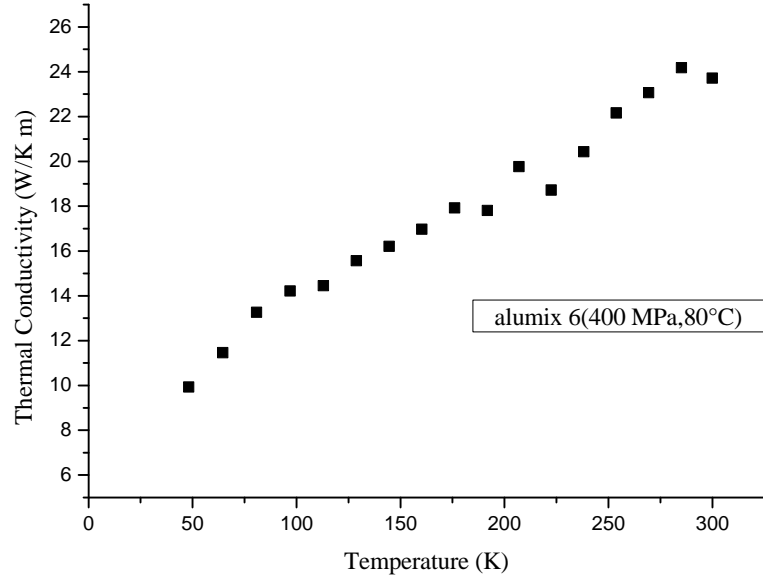


Figure 4.16. The thermal conductivity –Temperature graph of alumix(431) 6

In these graphs, it was indicated that two beginning transition temperatures. The temperatures remarked out two high T_c phases. Whereas the first transition is occurs because of η' phase progressively weaken, the second transition occurs owing to η phase becomes more impressive. Another possible reason for the reducing of the density is a decreasing in the phonon scattering inclined via flaws such as vacancies. (Özkurt et al., 2007) This case is occurred either electronic contribution or phononic contribution because of the reducing in phonon-carrier spreading and an increase in the phonon free path or both of them can be impressive (Aksan et al. 2007).

The same case exists in alumix 2, 3, 4 specimens. Only in this graphs quasiparticle life-span and quasiparticle mean free path abruptly increase in the superconducting state. This inclines in the electronic heat transport (Figure 4.20-22.) (Aksan et al., 2012).

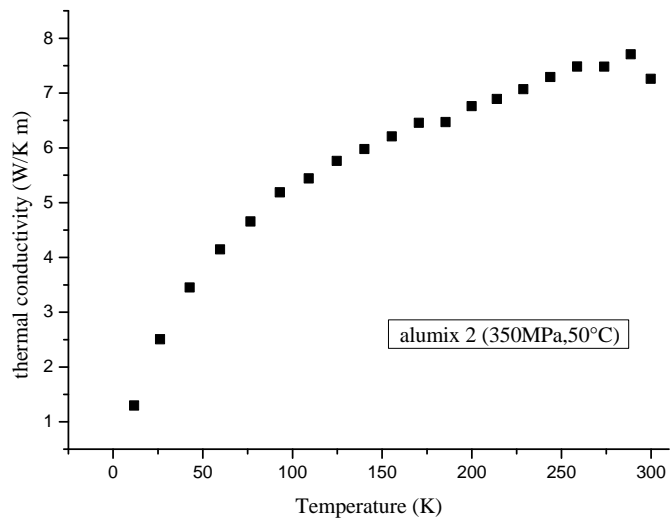


Figure 4.17. The Thermal Conductivity –Temperature graph of alumix(431) 2

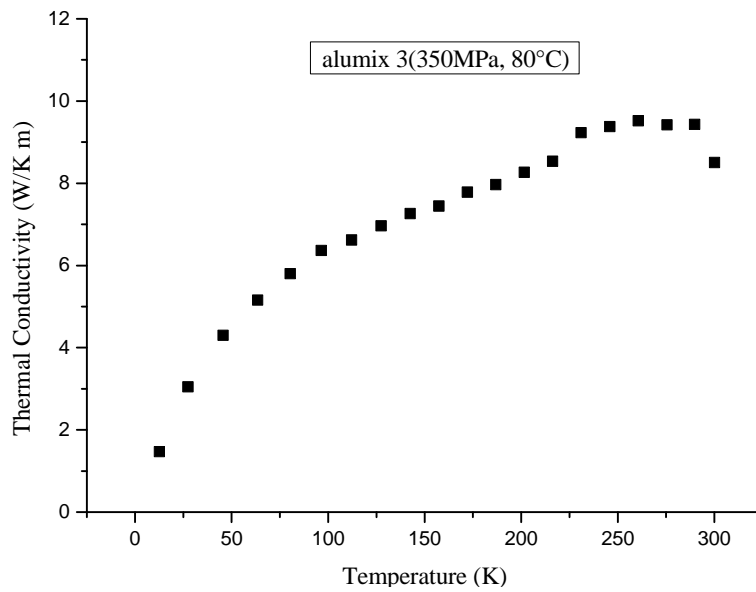


Figure 4.18. The Thermal Conductivity –Temperature graph of alumix(431) 3

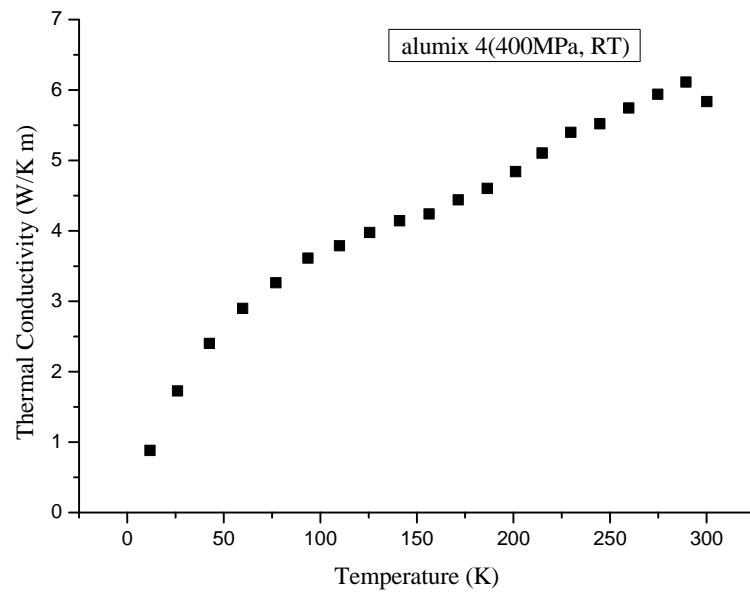


Figure 4.19. The Thermal Conductivity –Temperature graph of alumix(431) 4

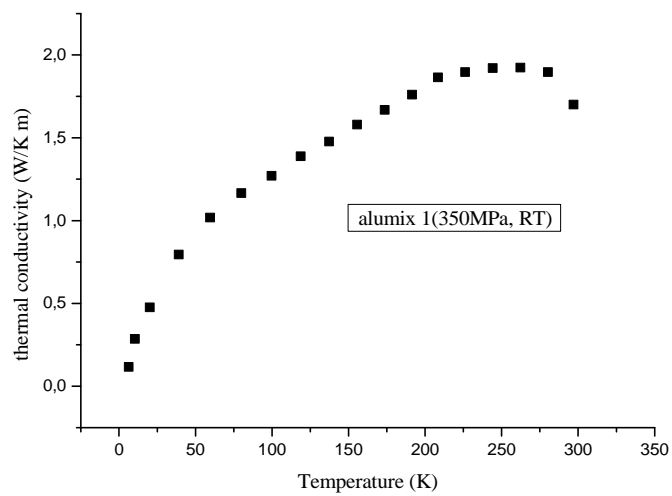


Figure 4.20. The Thermal Conductivity –Temperature graph of alumix(431) 1

4.6. Analysis of Seebeck Coefficient Results of Alumix(431) For 1, 2, 3, 4, 5, 6 Specimens

The Seebeck coefficient value is important physical property in reclaiming the potential performance of thermoelectric materials. The value is quite sensitive to the electronic structure and formulated by Mott's formula at a temperature T, for ordinary metals and semiconductors;

$$S(T) \propto T \left(\frac{\partial \ln \sigma(E)}{\partial E} \right)_{E_T = E_F} \quad (4.1)$$

Where σ_E is stated the electrical conductivity as a function of energy (Kuo, et al. 2012).

In alumix 1 sample, a change in transport feature is appeared as the sign and the magnitude of S(T) change rapidly, demonstrating charge carriers varies from n- to p-type in figure 4.19.

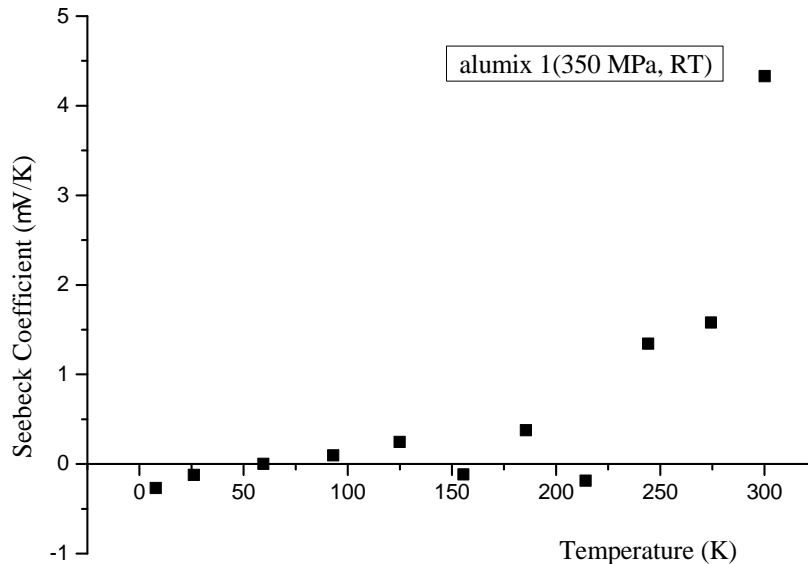


Figure 4.21. The Seebeck Coefficient –Temperature graph of alumix(431) 1

For alumix 1 (at various temperatures), alumix 2 (at 60K), alumix 3 (at 172K) alumix 6 (at 164.23 K), Seebeck coefficient values of the $0.09372 \mu\text{V/K}$, $0.0507 \mu\text{V/K}$, $0.00187 \mu\text{V/K}$, $0.0106 \mu\text{V/K}$ and respectively. Seebeck effect generated via both electrons and holes. Electrons and holes neutralize each other. The Fermi level can be offset from the lowest part of the pseudogap to a conduction band possessing a sharply increasing density of state (DOS) via electron doping in all the alumix 431 systems related on the rigid band model. After, the Seebeck coefficient increases as to Mott's equation. This equation proposes the Seebeck coefficient value is commensurate to the slope of the DOS at Fermi level. According to above equation, the negative effect of Seebeck coefficient is occurred via the increasing in the number of carriers, while the positive effect on the Seebeck coefficient is obtained from the increase in the slope of the DOS (figures 4.19-22) (Mikami et al., 2009).

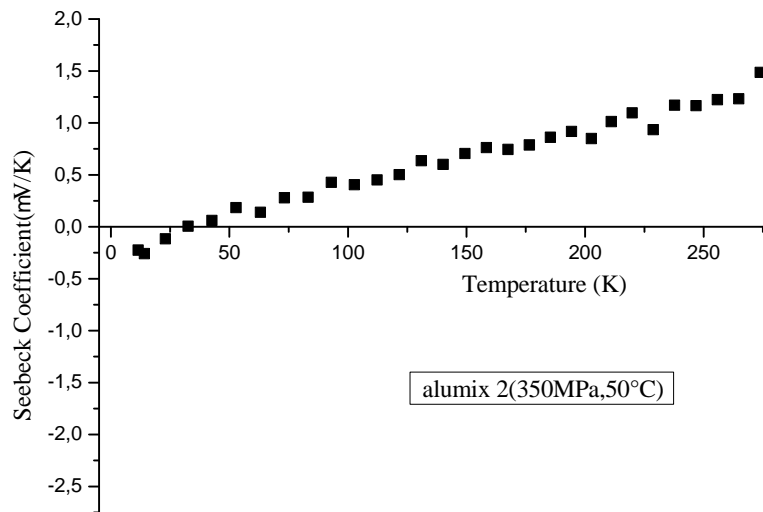


Figure 4.22. The Seebeck Coefficient –Temperature graph of alumix(431) 2

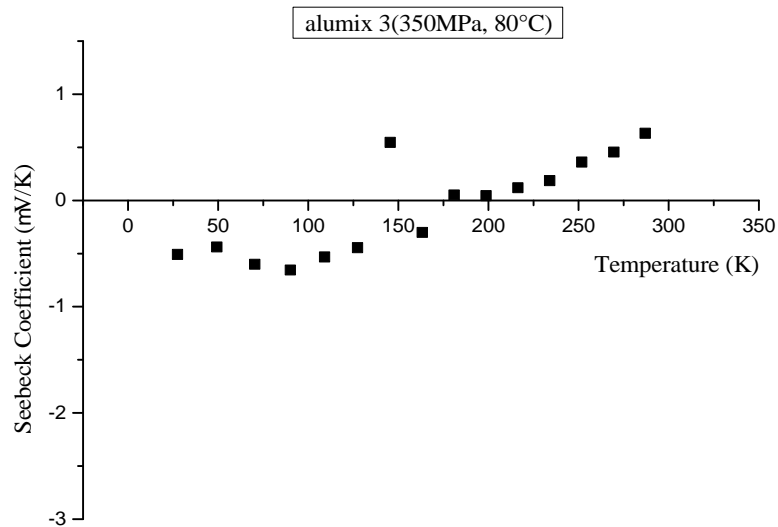


Figure 4.23. The Seebeck Coefficient –Temperature graph of alumix(431) 3

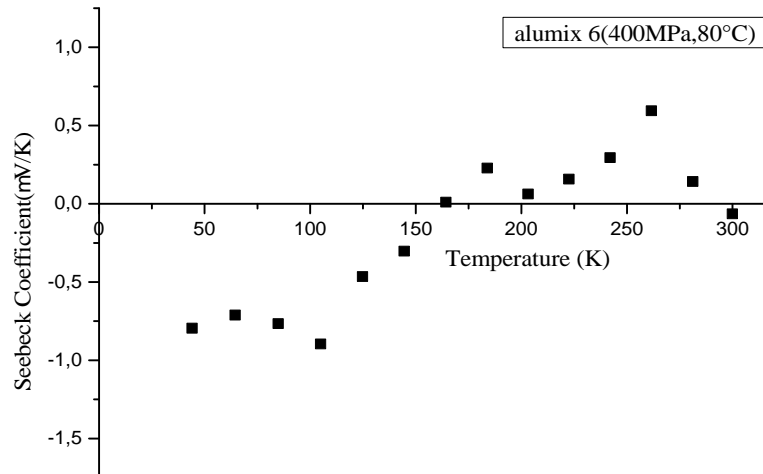


Figure 4.24. The Seebeck Coefficient –Temperature graph of alumix(431) 6

At alumix 3,4,6 specimens in figures 4.24, 4.27 and 4.28; a change of $S(T)$ sign says the existence of both positive (holes) and negative (electrons) types of carriers, this case show the multiband nature of the compounds. The positive contribution resulted from holes come from a powerful energy related to hole mobility, leading the positive TEP at higher temperatures. The figures exhibited that in the alumix systems, both the defects and dislocations increase. Also the extra scatter mechanism increases from both the impurity atoms and flaws and dislocations. This case induces to a increasing of the mean-free path of electron-hole pairs, and causes to positive effect on the TEP results (Özkurt et al., 2007).

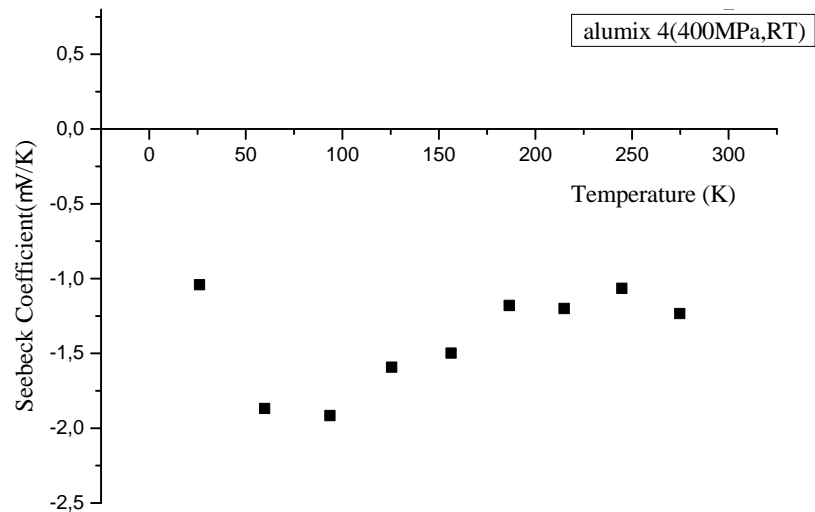


Figure 4.25. The Seebeck Coefficient –Temperature graph of alumix(431) 4

Alumix 4, 5, 6 samples, it is explained that around the Fermi level, the electronic band structure is qualified via a small coincide of alumix conduction band minimum, comprising electron carriers, with a valence band maximum increasing

For alumix 5 and 6 specimens, valleys, at 0-150K temperature range, is explained the larger influence in lowering and imperfection the transition properties (the valleys of Seebeck coefficients; for alumix 5 sample, is $-3.0657 \mu\text{V/K}$ at 90.82K, for alumix 6 sample, is $-0.895 \mu\text{V/K}$ at 105K; (Figure 4.22 and 4.24)

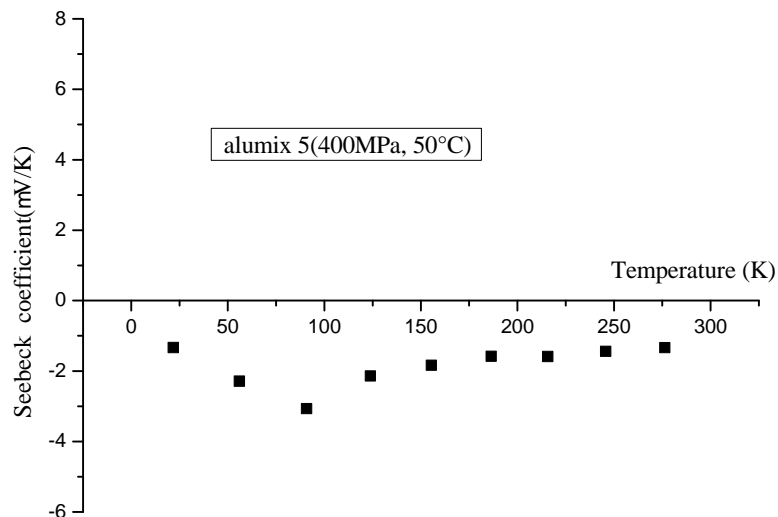


Figure 4.26. The Seebeck Coefficient –Temperature graph of alumix(431) 5

In alumix 6 sample graph exhibited as figure 4.20., Seebeck coefficient values of alumix 1 at temperature ranges between 150-200K and 200-300K are 0.228 $\mu\text{V/K}$ and 0.594 $\mu\text{V/K}$ respectively, for this reason, the samples show positive peak, at the same time it was observed that samples indicated the negative peak at 50-100 K temperature range. This case is explained through the Kondo Effect and crystal electric field, the second positive peak is showed the spin fluctuations on its ground state. As a known the Kondo effect is occurred to the appeared upturn the resistance at low temperatures (Kouwenhoven and Glazman,2001; Kuwai et al., 2006) .

In alumix 6 sample graph, the Seebeck coefficient sign indicates positive value at temperature from 50 K to room temperature due to the having the holes which are the major conductivity carriers. But, in alumix 2 and 5 samples, the sign of Seebeck coefficient shows negative value for measured temperature range. This case is also explained that the major conductivity carriers are electrons (Park et al.). Electrons are the prevailing charge carriers in alumix 2 and 5 samples, while holes the dominant charge carriers in alumix 6 specimen (Smontara et al.). Seebeck coefficient is increased, when the more acute spreading carriers as the temperature is increase. The negative peak compressed with increasing the heat treatment time. The decreasing of phonon heat current causes to a decrease in phonon-drag effect. This effect is electron transported momentum. Hence, the negative peak is referred to phonon-drag effect (Aksan and Yakıncı, 2007). And then, the Seebeck coefficient decreases because of a rapid increase in carrier concentration with the increasing of the temperature.

Higher Seebeck coefficient is succeeded in higher porosity specimen. On the Seebeck coefficient, the grain size possesses the effect. When the number of both impurities and point flaws within grains slant to increase through the decreasing of the grain boundaries, with the rising spreading of carriers resulted via impurities and flaws, Seebeck coefficient increase (He et al.2007).

As a result; at all alumix 431 samples (except sample 2) presents an increasing tendency with the measurement temperature range while alumix 2 sample exhibited in figure 4.20. showed the decreasing tendency with sintering temperature

of 250-300K. This case is resulted from the increasing of electron concentration because of anti-structural defects constitution.

4.7. Analysis of Figure of Merit Results of Alumix (431) For 1, 2, 3, 4, 5, 6 Specimens

The dimensionless figure of merit, ZT , sums up the thermoelectric properties. The value is an important factor in choosing materials for thermoelectric power generation. The dimensionless figure of merit is reckoned from the electrical conductivity, Seebeck coefficient and thermal conductivity measured.

All the ZT of alumix (431) specimens related to the thermal conductivity besides the power factor (Tani and Kido, 2008).

For alumix 1, 3, 5 sample graphs, the small values of ZT in such a manner that for alumix 3 sample, the value is 1.527×10^{-10} at 214K ; for alumix 4 samples the value is 3.803×10^{-8} at 21.8K; for alumix 6 sample, 2.121×10^{-10} at 63.4K, are resulted from very large thermopower, low thermal conductivity and very high the electrical resistivity. Also their carrier concentrations are optimized (figure 4.25-27) (Zhang et al.,2009; Søndergaard et al., 2013).

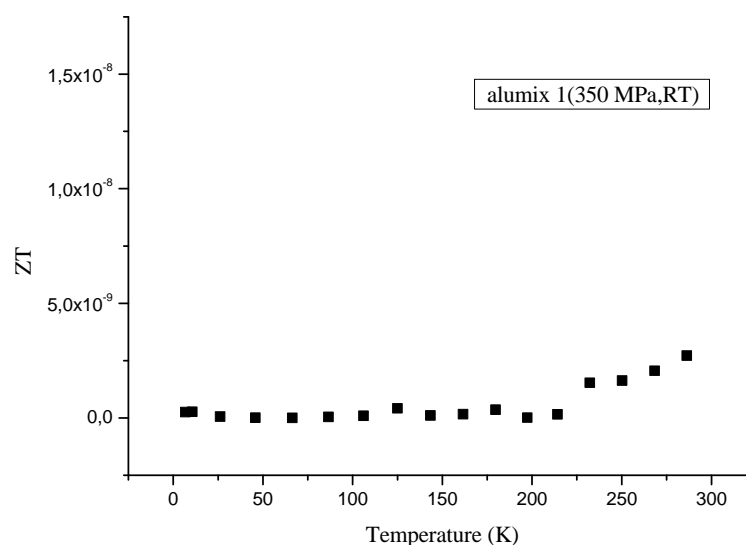


Figure 4.27. The ZT –Temperature graph of alumix(431) 3

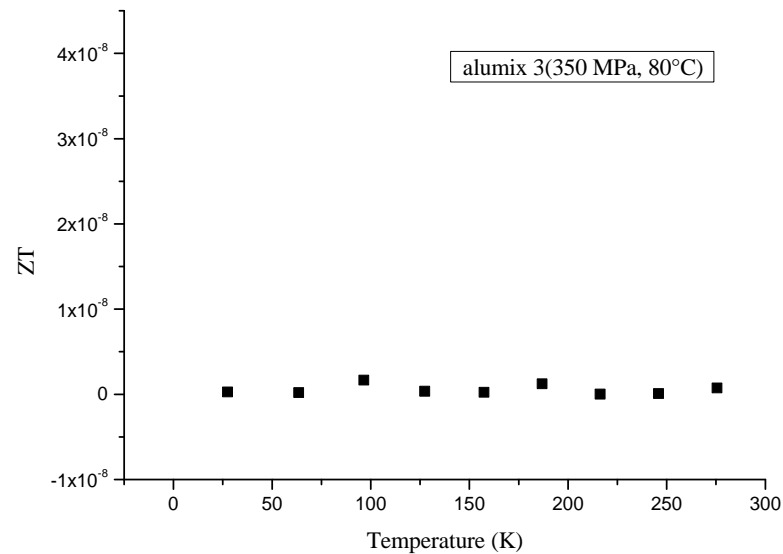


Figure 4.28. The ZT –Temperature graph of alumix(431) 3

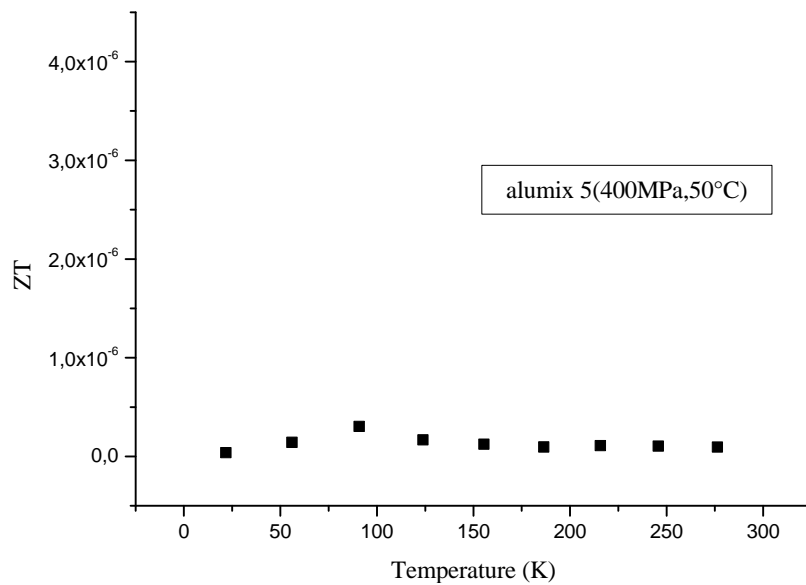


Figure 4.29. The ZT –Temperature graph of alumix(431) 3

In alumix 2 specimen graph (figure 4.28.); the enhancement of the thermoelectric features is commonly originated from improved phonon scattering, increasing of electrical conductivity and mostly its lower electrical resistivity (Wang et al.2011 and Ahmadpour et al. 2007). Lower thermal conductivity and much lower

Seebeck coefficient which is seriously defacer to ZT is observed in alumix 3 sample graph as shown in figure 4.26. (Carlini et al., 2014).

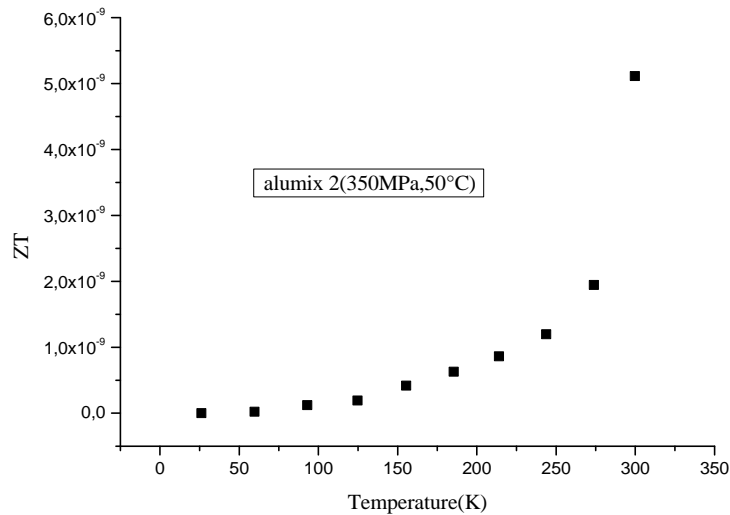


Figure 4.30. The ZT –Temperature graph of alumix(431) 2

In figures 4.30 and 4.31; for alumix 4 and 6 specimens, ZT decreases due to the increase of thermal conductivity and the highest ZT attains about 5.0×10^{-9} at 325 K by improvement of Seebeck coefficient (Han et al.). Samples show valleys at the temperature ranges 110-260K (for alumix 1) and 130-190K (for alumix 5) due to $\eta \rightarrow \eta'$ phase transition. Also, it is preponderated with various effects such as larger thermal conductivity, smaller Seebeck coefficient, though its electrical resistivity is improved. This enhancements in the thermoelectric properties of alumix 6 and 4 specimens, arise from the reduce in both the electrical resistivity and lattice thermal conductivity which can be attributed to the increased holes concentration and improved phonon scattering (Pan et al.2010).

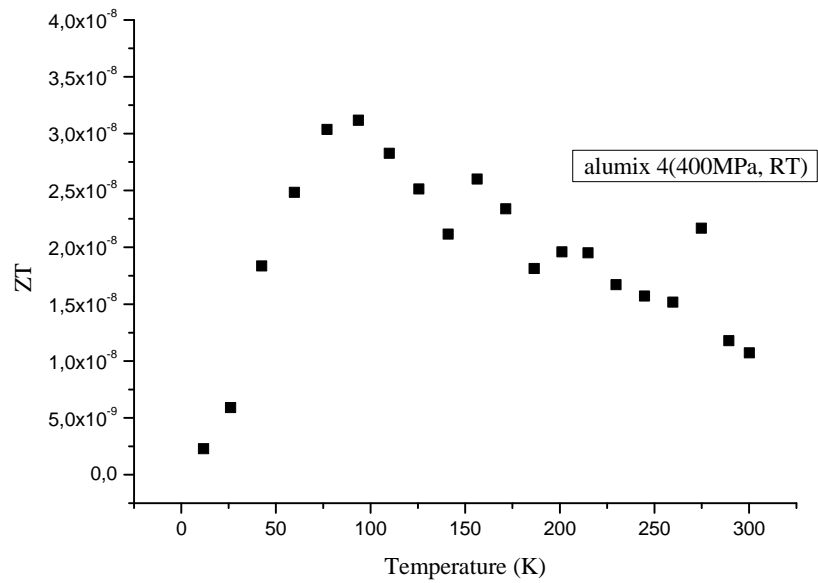


Figure 4.31. The ZT –Temperature graph of alumix(431) 4

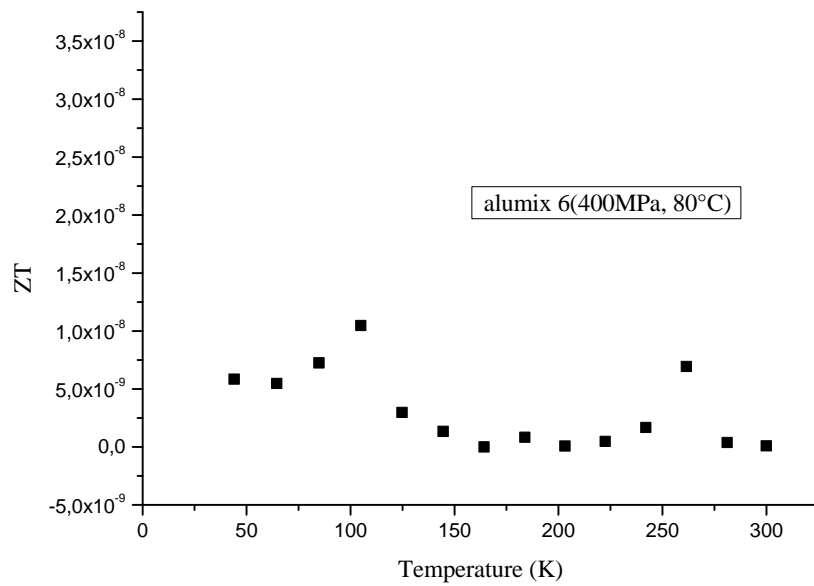


Figure 4.32. The ZT –Temperature graph of alumix(431) 6

4. RESULTS AND DISCUSSIONS

In this study, the thermoelectric properties of alumix (431) (Al-5.5 Zn-2.5Mg-1.5Cu) prepared on different pressures and temperatures have been investigated. It was examined Optical microscope, SEM images and density measurements of specimens for their structural properties and searched the electrical resistivity, thermal conductivity, Seebeck coefficient, the dimensionless figure of merit (ZT) data obtained from PPMS Quantum Design (Physical Property Measurement System) at measured temperature ranges 5-300 K for their thermoelectric properties.

In this study, the samples prepared on different pressures and temperatures were symbolized 1, 2, 3, 4, 5, 6

Alumix 1	350MPa, RT
Alumix 2	350MPa, 50°C
Alumix 3	350 MPa, 80°C
Alumix 4	400MPa, RT
Alumix 5	400MPA, 50°C
Alumix 6	400MPa, 80°C

4.1. Analysis of Optical Micrographic Figures of Alumix (431) 1, 2, 3, 4, 5 ,6 Specimens

In Figures 4.1, and 4.2, the badge microstructure of primary α -Al solid solution turned round via inter-dendritic secondary phases and some grain boundary precipitates having laminar morphology was shown. It was observed that the microstructures have the eutectic characteristic structure. In the microstructure, it is considered the existence of the coarse eutectic phases relating of the high amount of Zn, Mg and Cu in the alloys and low cooling rate linking to the traditional solidification process.

Figures 4.1 and 4.2 show the microstructure of Al-5.5Zn-2.5 Mg-1.5Cu alloy comprised of the both equiaxed grains and some fine secondary phases. The existence of the equiaxed grain morphology is considered to result from the high cooling rate, related to the rapid solidification processes. On the contrary, the existence of coarse eutectic phases in the IM counterpart processed traditionally was repressed.

In this Figures 4.1 and 4.2, it is also shown that second phases having both the grain boundaries and in the grain inners. The second phases in the grain inners reveal different shapes such as needle and square microstructure shape of particles. Along the matrix, most of the second phases is the comparative uniformly dispersed and it is sighted the some of the grain boundary precipitates possessing an allotriomorphic morphology (Feng et al. 2009)

The concentrated second phases have eutectic precipitated from the liquid phase directly at grain boundary. The distributed gray phases within the grains are mostly the strengthening phase (MgZn_2). The phase is precipitated from solid based body. In the microstructure, it was observed the some tiny pores. The pores decrease by the mechanical properties.

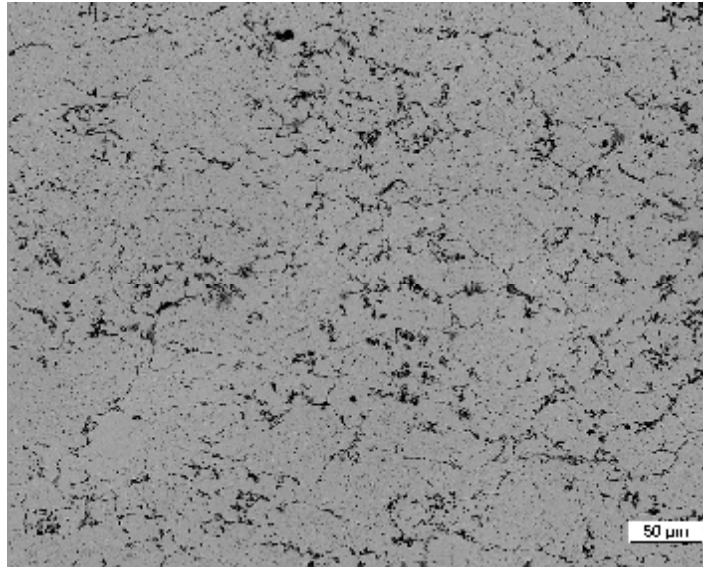


Figure 4.1. Optical microscope image of alumix (431) sample (50µm).

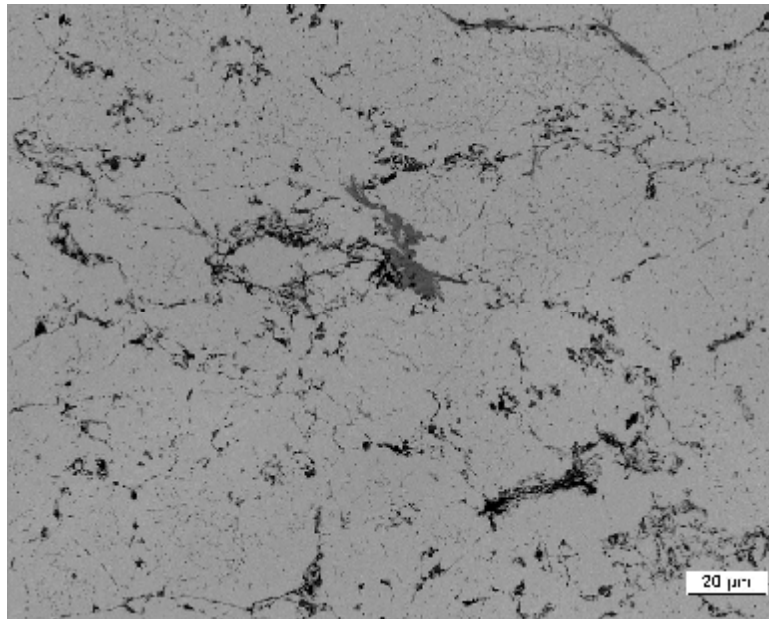


Figure 4.2. Optical microscope image of alumix (431) sample (20µm).

The cracks near the crack source zone of the fracture are intergranular microstructure. Course of events of deep into certain depth, the cracks transits into transcrystalline. Some coarse particles were sighted on the surface of the specimens. This case manifests the fatigue damage (see in Figure 4.3.) (Hai-Gen et al., 2009).

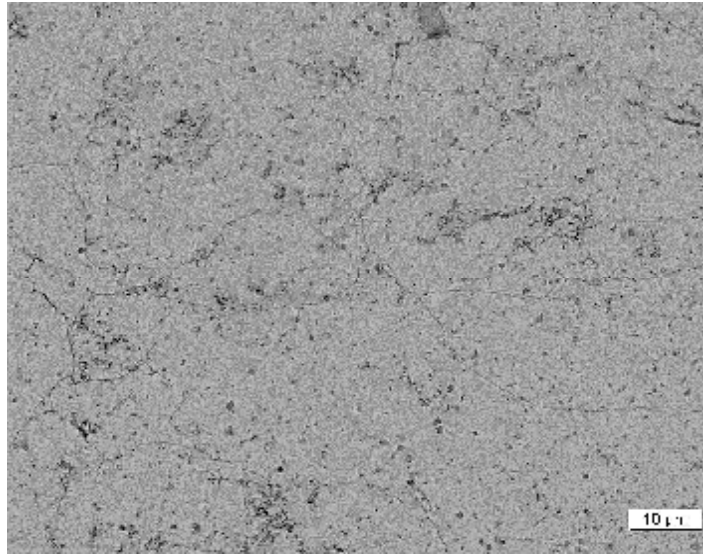


Figure 4.3. Optical microscope image of alumix (431) sample with transactions (10 μ m).

In the figure 4.4., it is observed that an equiaxed grains and two types of phases with apparent origins. The first one is the phase occurred at the grain boundaries throughout the solidification process led by the segregation of the alloying elements. The other phase is commonly constituted near the grain boundary. This case resulted from coring leading precipitation. Many coarse precipitates are apparent within the constituted grains (Mazzer et al. 2013).

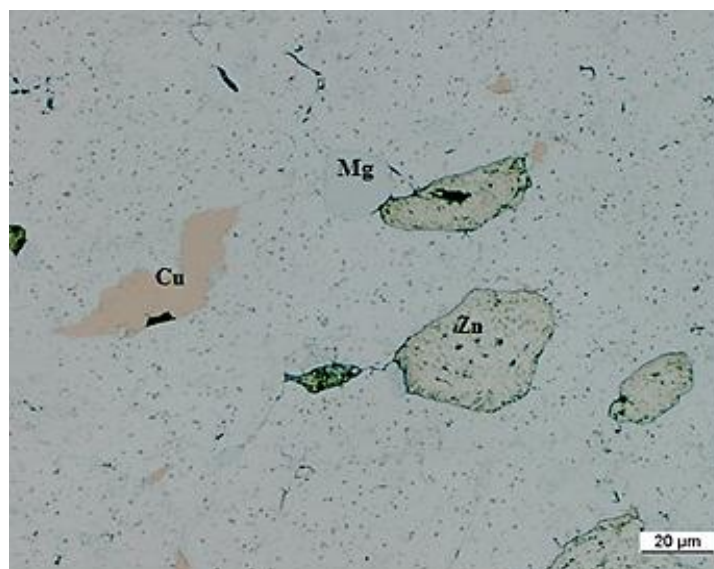


Figure 4.4. Optical microscope image of alumix (431) sample with materials (20 μ m).

4.2. Analysis of SEM Figures of Alumix (431) 1, 2, 3, 4, 5, 6 Specimens

Figures 4.5-8 present the fracture surface of the samples. Many fine holes specified ductile resulted from fracture can be observed. Holes caused from the aged sample treated smaller than the solution heat treatment. It manifests the precipitated particles have affected the fracture occurred. At the grain and subgrain boundaries, the smaller holes are constituted because of the existence of the equilibrium η phase at these regions. This phase decrease the plastic deformation at the zone and the following plastic flow around the precipitates (Mazzer et al. 2013).

The precipitation behavior in α -Al matrix is related to the mechanical properties sized such as the ductility change and strength of various hot deformation treatments linked to size, dispersion and volume fraction of the precipitated second phases. It is observed the transgranular microstructures and fine holes with secondary cracks, in the figures. This case means the undissolved coarse phases caused to stress concentration. This stress concentration occurs in the constitution of the secondary cracks in the matrix and worsening influence on the ductility (Jia et al. 2012).

Deep and fewer holes were observed. The holes caused from including of secondary phases. It is considered the fracture of precipitates induced to the fracture. Naturally aged joints showed the fracture surface surrounded with deeper and larger holes besides few flat zones. Some deep hollows can be observed on the surface of the fracture (Figures 4.5-8) (Sharma et al. 2013).

The surface of fractures showed the mainly cup-cone holes with changing and no such intergranular cracks are seen. This case is explained the ductile fracture, non-similar intergranular brittle failure (Rout et al. 2014).

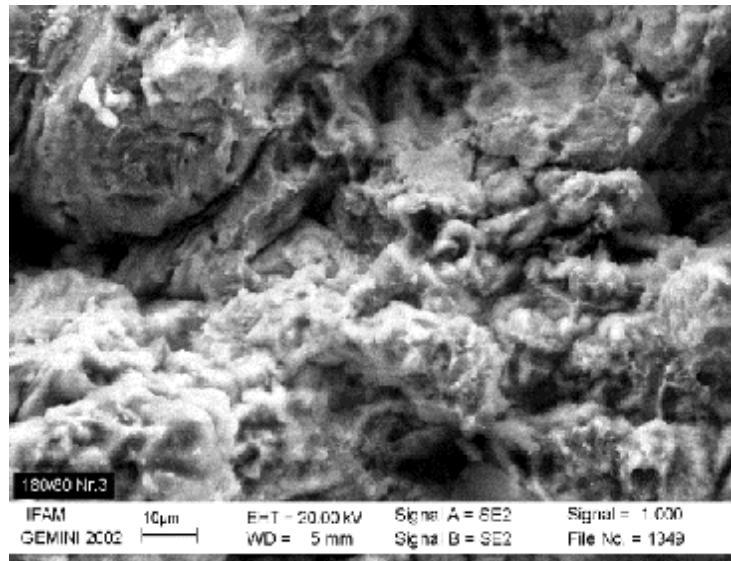


Figure 4.5. SEM image of Alumix (431) sample prepared under the 180MPa and 80° conditions(10µm).

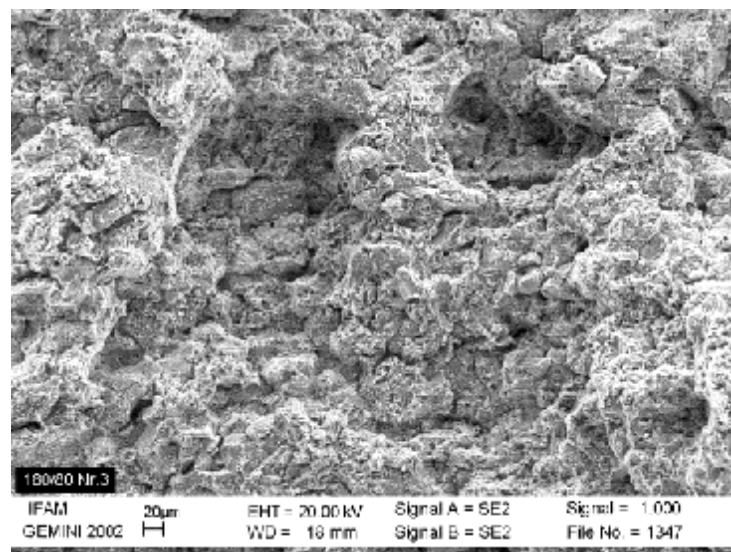


Figure 4.6. SEM image of Alumix (431) sample prepared under the 180MPa and 80° C conditions (20µm).

4.3. Density Measurements of Alumix 431 Specimens

The results of the density measurements of Alumix 431 indicates the highest density on compacted specimen at 400MPa/RT. It was observed the decreasing porosity and homogeneous structure with increasing temperature. This case is shown that the density was influenced directly with decreasing porosity and shrinkage of pores was generated because of reducing of volume of sintered parts and non-varied weight. Therefore, these conditions increased the density. High density is resulted from high strength of sintered parts and high density also influences mechanical properties such as strength, toughness and hardness. For this reason, high density property is a desirable feature (İynen et al., 2010)(Figure 3.1-2).

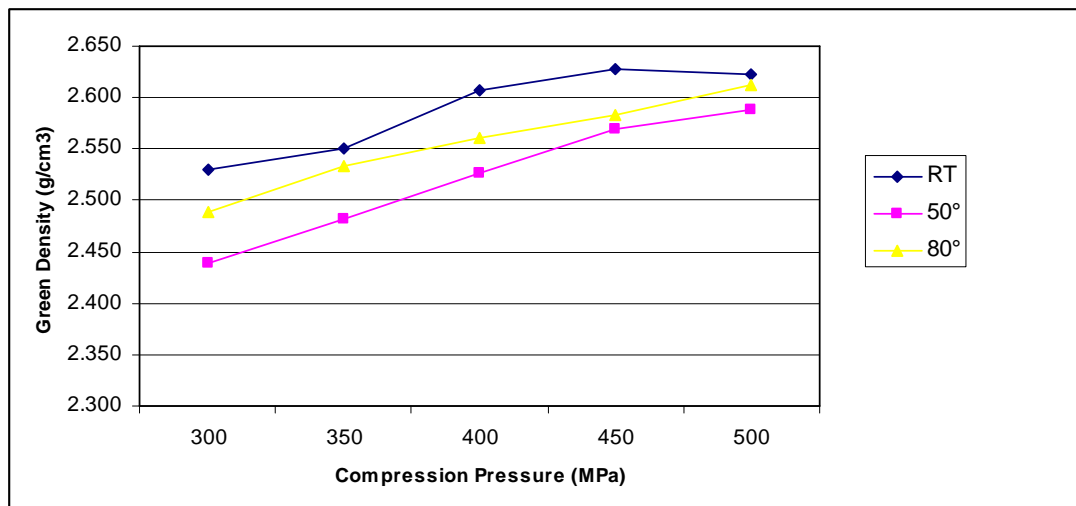


Figure 4.7. The green density (g/cm^3) changes of Alumix 431 samples related to compression pressure(MPa)(İynen,2009).

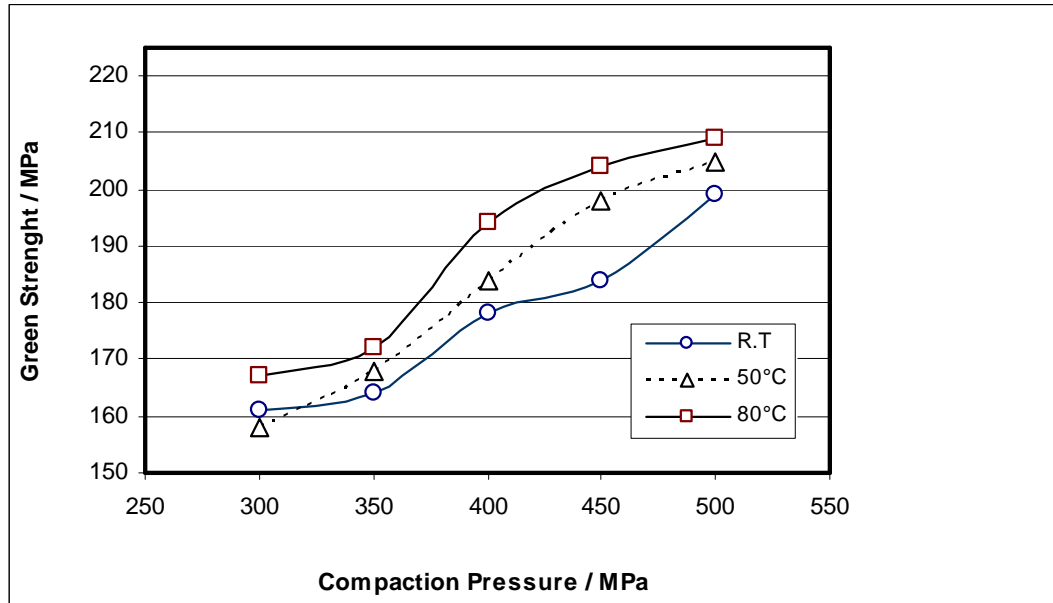


Figure 4.8. Relationship between the compaction pressure and green strength of the samples prepared in three various compaction temperatures (İynen,2009).

4.4. Analysis of Electrical Resistivity Results of Alumix (431) 1, 2, 3, 4, 5, 6 Specimens

Electrical resistivity is a significant feature related to material, and is generally dependent upon the temperature. At room temperature, ρ value is representer of if a material is an insulator (ρ is on the order of $10^6 \Omega\text{m}$) or a metal (ρ is on the order of $10^{-6} \Omega\text{m}$ or less). Among the metal and insulator orders, semiconductor materials' resistivity values are low from materials. For the thermoelectric material the optimum electrical resistivity range is varied from 10^{-3} to $10^{-2} \Omega\text{m}$.

In metallic compounds, the analysis of the electrical resistivity related the temperature is an effective tool to acquire knowledge related the main features of these materials.

Alumix 1 is a the best material according to the other materials over 230K and ρ is roughly constant and the size and temperature related of ρ in the material is like to sighted in wicked metals or heavy added semiconductors (electrical resistivity of $0.13482 \Omega\text{m}$ at 230 K) indicated as figure 4.7. Also the decreases show the specifial metallic behavior of the alumix 431 systems.

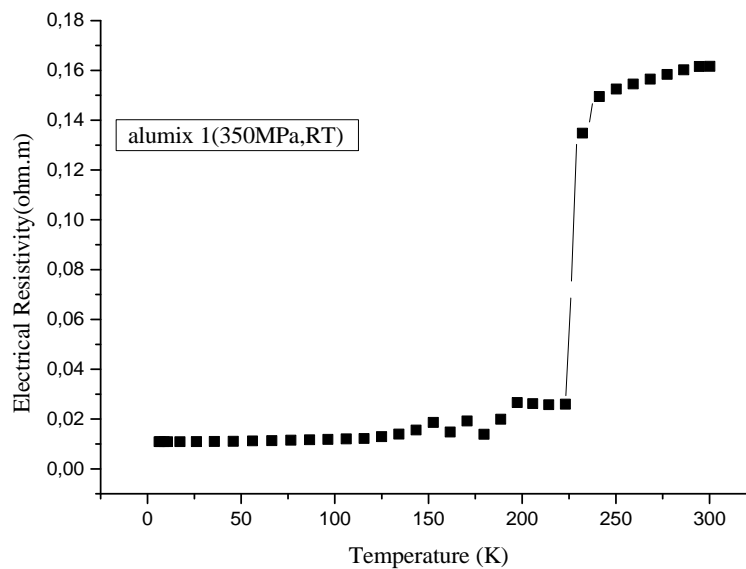


Figure 4.9. The Resistivity –Temperature graph of alumix(431) 1

For alumix 1 specimen; such a tendency is ascribed to a falling offset of E_F from the valley of the pseudogap. E_F moves to the location with larger density of states (DOS) leading to the decreasing in the electrical resistivity magnitude. The sample also indicates reducing of the same tendency with an inceptive step. The explanation for this case can be related to electrical conductivity that is electrical conductivity is based on the degree of texture; the conductivity increases with the increasing of the texture strength.

In the Figure 4.7., the sharp rise was exhibited. This case was considered to originate the impurity phases developed in the base matrix and weak inter-granular matchup. Development of both impurity phases and constitution of weak matchup among the impurities and alumix 431 grains acts a significant role in reducing the transition temperature (T_c) and increasing in the normal state resistance. As a result of in the figure the linear increase is means to a metallic behaviour down to transition temperature (T_c) (Aksan et al. , 2006, 2007).

For alumix 3 sample, the $\rho(T)$ relation of alumix 3 system, nearly resembles nonmagnetic amorphs alloys with Pauli paramagnetism of conductivity electrons. Also, in the graph in Figure 4.8. , at 225-275 K, this case is explained that on the electrical resistivity, both the constitution and resolution of η' phase and the constitution of η phase possess a powerful effect. This effect is more than inclined via the development of Guinier – Preston (GP) zones. The development is based on the a small peak centered at 225 K. The reason for this result may be less in flaws' concentration and sprinkling because of the slow cooling process. The process is required for the constitutions of the GP zones. The linear increase of alumix 3 specimen shows the favorable action inside the Baym-Meisel-Cote theory that regards the inelastic electron-phonon reaction. Below the Debye temperature θ_D , at temperatures, for the electron transport this case is important (Figure 4.8.).(Smontara et al., 2007)

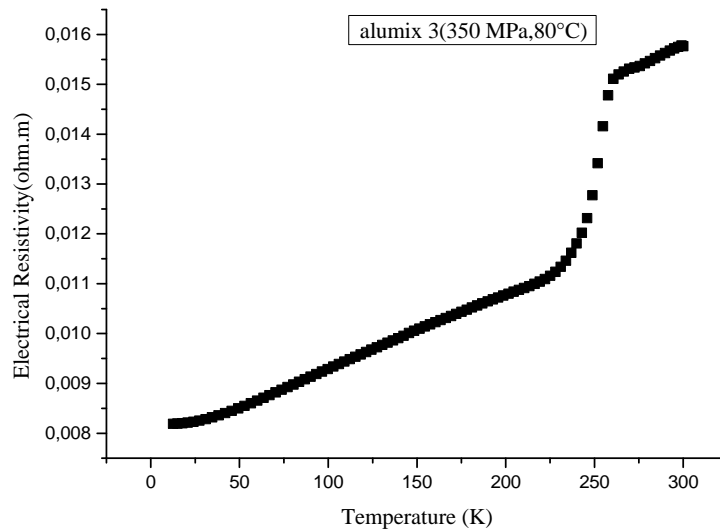


Figure 4.10. The Resistivity –Temperature graph of alumix(431) 3

In alumix 1, 3, 4, 6 samples, it is indicated that an abrupt jump in similarity of the structural transition at different temperatures. With respect to resistivity magnitude, in agreement with behavior indicated via thermoelectric power. Alumix 431 samples is reckoned through hole transport, as proved via positive sign of the Seebeck effect. (see Figure 4.7-10)(Carlini et al., 2014)

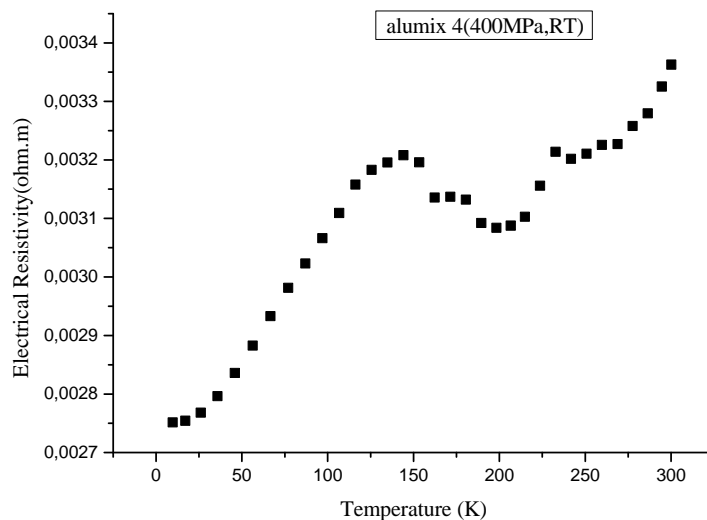


Figure 4.11. The Resistivity –Temperature graph of alumix(431) 4

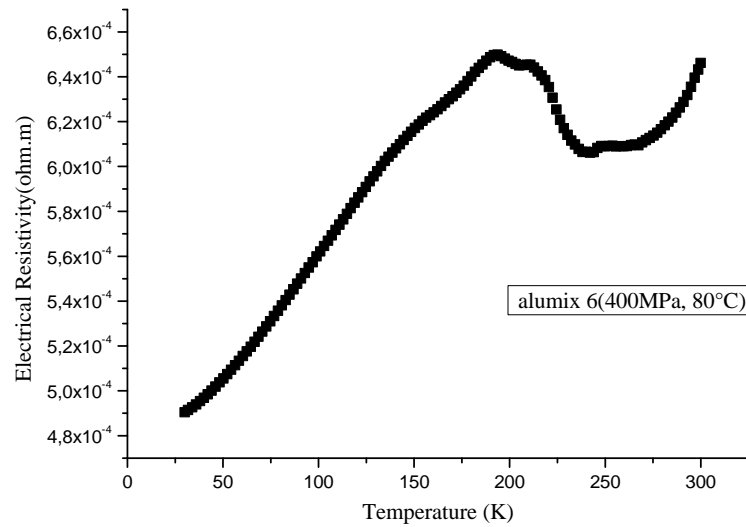


Figure 4.12. The Resistivity –Temperature graph of alumix(431) 6

In alumix 1(25-225K) (Figure 4.7.), alumix 2(5-300K) (Figure 4.11) alumix 6(at 30-195K), (Figure 4.10.), alumix 5(at 10-180K) (Figure 4.12.), alumix 4(25-115K) (Figure 4.14), (Figure 4.15) specimens, the resistivity values rise from 8.2×10^{-4} to 1.1×10^{-3} for alumix 1, from 0.0217 to 00445 for alumix 2; from 2.7×10^{-4} to 3.2×10^{-4} for alumix 4, from 4.72×10^{-4} to 7.60×10^{-4} for alumix 5; from 5×10^{-4} to 6.5×10^{-4} for alumix 6. The increases exhibited the consistent of the electrical resistivity hoped for a degenerate semiconductor; increasing with temperature, probably because of acoustic phonon spreading. (Figure 4.11.) (Tsujii et al., 2011).

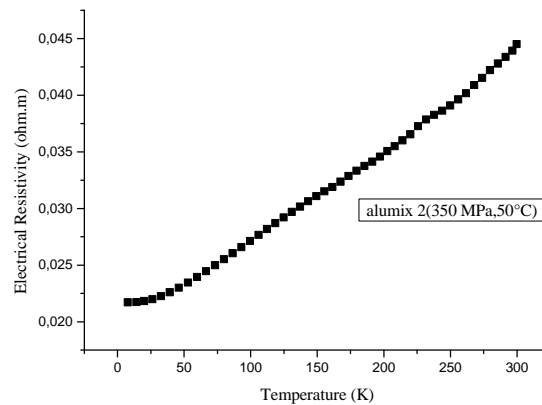


Figure 4.13. The Resistivity –Temperature graph of alumix(431) 2

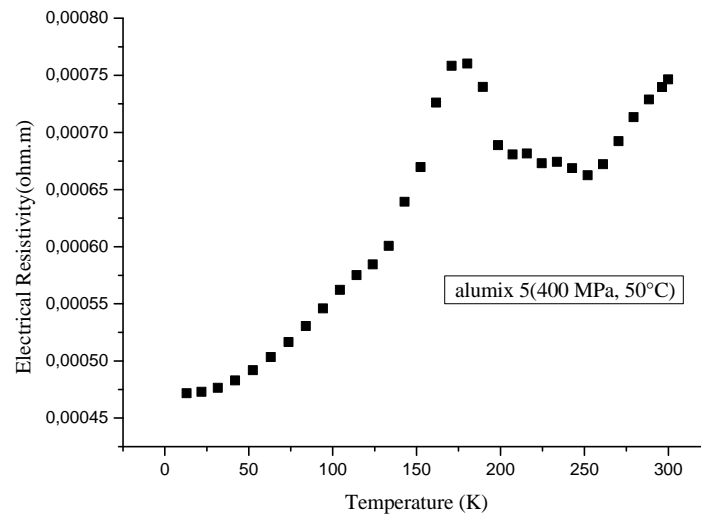


Figure 4.14. The Resistivity –Temperature graph of alumix(431) 5

In alumix (431)4, 5, 6 samples, the graphs (Figure 4.9-11) are signed the A, B, C, D, E, F characters. The characters are stated the properties of alumix 431 systems whether the solutions, transitions, diffusions or not. AB, BC, CD, DE, EF are defined the a metallic transition because of spreading of electrons from isotropic centres, a semi insulating transition is commented as the constitution of either electron hole drop (EHD) or quantum well, semi metallic transition because of anisotropic spreading of electrons from gap or cracked sites, metalloid diffusion transitions and semi metallic diffusion (both are referred the a hybrid transition) respectively(Gormani et al., 1995).

In alumix 4 (144-189K) , alumix 5(at temperature range 180-207 K) alumix 6(at temperature range 210-245K), , the decreases in alumix (431) systems is clarified lowers the resistivity of from $3.2 \times 10^{-4} \Omega\text{m}$, $7.60 \times 10^{-4} \Omega\text{m}$ $6.457 \times 10^{-4} \Omega\text{m}$, and to $3.0923 \times 10^{-4} \Omega\text{m}$ $6.807 \times 10^{-4} \Omega\text{m}$, 6.0657×10^{-4} , respectively, and produces a metallic conductors shown in Figures 4.1-14. These observings show that within these temperature ranges, there is a composition attribute that obtains semiconducting features while metallic behavior is sighted on both sides of these ranges.

In the decreases of the alumix (431) 4, 5, 6 systems, the temperature related to mobility presents that the $\mu \propto T^{-3/2}$ expression and the acoustic lattice scattering is

the predominant mechanism. Therefore, the increase in ρ at low temperature is clarified via the decrease in mobility with the increasing the temperature and the decrease is also explained conduction happens due to their band gap. The peaks also related with the sequence of the constitution and resolution of metastable phases(Tani and Kido, 2008).

In these materials the electrical resistivity values is based on the precipitation process of Al-Mg-Cu phases and their slight increases with a further increases in the temperature can be ascribed to the reducing amount of Al-Mg-Cu types precipitates in the alumix 431 structures at temperature ranges from 25 K to 200K, 175K, 180K respectively. These changes are rapid after 275K, 265K, and 285K respectively, as the resolution process dense, when Al-Mg-Cu type precipitates are no more stable. After 300 K, electrical resistivity value reaches the maximum value as the resolution of the alloying elements is rounded around. For alumix 1, 4, 5 samples gives the values of resistivity $6.46 \times 10^{-4} \Omega m$, $7.465 \times 10^{-4} \Omega m$ and $3.4 \times 10^{-4} \Omega m$ respectively.

4.5. Analysis of Thermal Conductivity Results of Alumix (431) 1, 2, 3, 4, 5, 6 Specimens

A high quality thermoelectric material must be required both a high electrical conductivity and a high thermopower and a low thermal conductivity as explained introduction section. The first two are specified via the electronic properties of the material, these are comprised into the quantity $PF = \alpha^2 \sigma$ defined to 'power factor'.

As a known, the thermal conductivity is stated with Wiedemann-Franz law expression; $\kappa = \kappa_e + \kappa_l$; in this expression; κ_e is transporting heat of carriers (electrons and holes), κ_l is expressed the travelling of phonons via the lattice. The thermoelectric figure of merit can be maximized through maximizing the electrical conductivity and minimizing the thermal conductivity. Increasing of the electrical conductivity both generates an increase in the electronic thermal conductivity and reduces the thermopower.

Increasing of ZT value through the decreasing of both κ , and the lattice contribution to the thermal conductivity. The most significant factors acts role; i) utilizing of compounds ii) the existence of heavy atoms weakly linked to the structures iii) the presence of inclusions and/or impurities iv) the solid solutions' constitution, v) the presence of a large number of grain boundaries (Elsheikh et al., 2014).

In all the alumix (431) specimens, the increases in the thermal conductivity can be considered to originating because of mainly the changes in lattice component term (κ_{ph}) (Demirel et al., 2014). Also these increases could be occurred because of the rapid reducing in electrical resistivity and accordingly strong increasing in the electronic thermal conductivity component κ_e (Gloria et al., 2013). Commonly it is ascribed to the porosity influence. High thermal conductivity was caused to low porosity position. In spite of that the thermal conductivity was increased with large grain size. This case is occurred because of decreasing grain boundary spreading of phonons (He et al., 2007).

For decreasing of all alumix 431 systems; the decreasing of κ originated the mass-variety scattering in the lattice of the alumix systems (Mikami et al., 2009). The Wiedemann-Franz law depend on the validity of the same the electron mean free path only at the low temperature for electrical and thermal transition. At low temperature, via flaws and impurities, the base electron spreading mechanism is elastic spreading mechanism. These low values show that electrons' elastic scattering acts the important role through impurities and flaws at room temperatures (Carlini et al. 2014). Stronger phonon scattering was caused to the lowest thermal conductivity (Pan et al., 2010).

For all the samples, it was indicated that increases firstly and then decreases at final measured temperature. This case results from the decreasing of thermal spreading at low temperatures. as the phonon free path is taken after to crystal site distance, the maximum κ value happens (Kuo et al.2012).

For figure 4.13 and 4.14; in alumix 5, 6 samples, at 250-300K, it was exhibited the rising from 7.29 W/Km to 7.83 W/Km for alumix 5; from 17.806W/Km to 18.720W/Km for alumix 6,. To state of the origin of such a rapid

increasing of κ , two mechanisms can be proposed. One mechanism attributed to the increase of phonon mean free path electrons intensify into the copper pairs. Other alternative mechanism ascribed to the electron contribution. The rapid increase of κ below transition temperature (T_c) indicates improvement of the quasiparticle contribution the heat conductivity and increase of the quasiparticle mean-free path. The κ (T) reduced in magnitude and the location of maximum offsets against lower temperatures. The irregularities caused to impurities flaws act as a important role in restricting the heat transport because of a strong increase of the electron-phonon impurity spreading rate (Aksan et al. 2007).

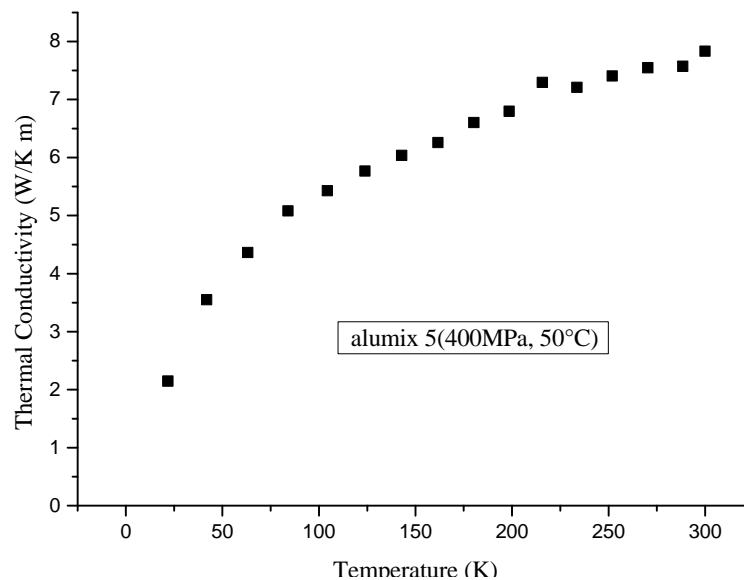


Figure 4.15. The thermal conductivity –Temperature graph of alumix(431) 5

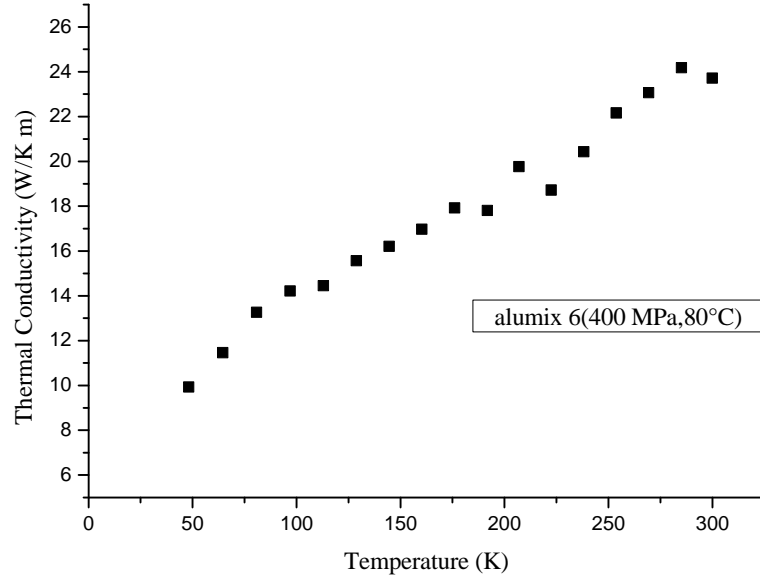


Figure 4.16. The thermal conductivity –Temperature graph of alumix(431) 6

In these graphs, it was indicated that two beginning transition temperatures. The temperatures remarked out two high T_c phases. Whereas the first transition is occurs because of η' phase progressively weaken, the second transition occurs owing to η phase becomes more impressive. Another possible reason for the reducing of the density is a decreasing in the phonon scattering inclined via flaws such as vacancies. (Özkurt et al., 2007) This case is occurred either electronic contribution or phononic contribution because of the reducing in phonon-carrier spreading and an increase in the phonon free path or both of them can be impressive (Aksan et al. 2007).

The same case exists in alumix 2, 3, 4 specimens. Only in this graphs quasiparticle life-span and quasiparticle mean free path abruptly increase in the superconducting state. This inclines in the electronic heat transport (Figure 4.20-22.) (Aksan et al., 2012).

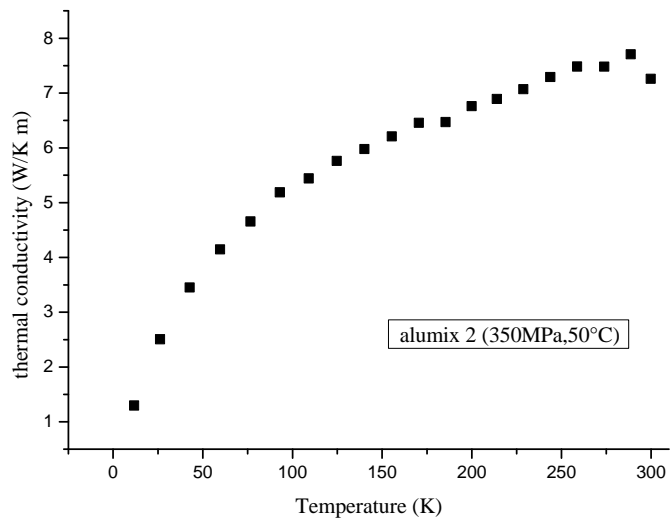


Figure 4.17. The Thermal Conductivity –Temperature graph of alumix(431) 2

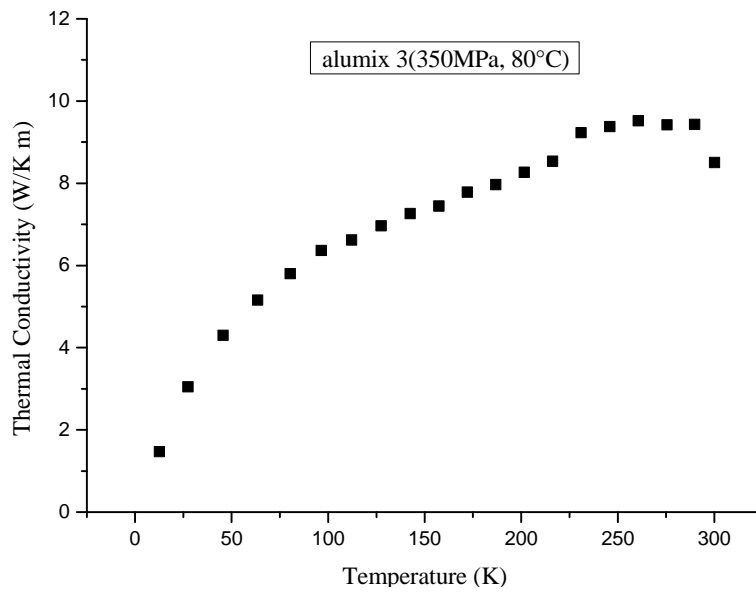


Figure 4.18. The Thermal Conductivity –Temperature graph of alumix(431) 3

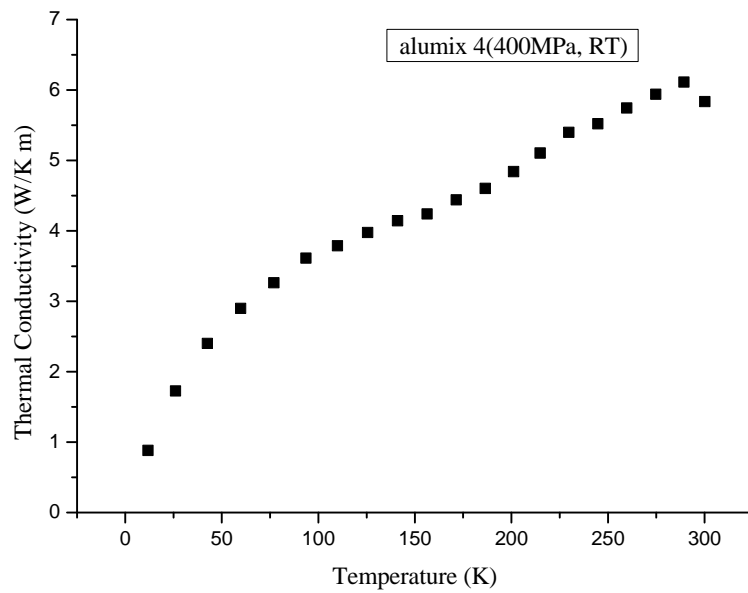


Figure 4.19. The Thermal Conductivity –Temperature graph of alumix(431) 4

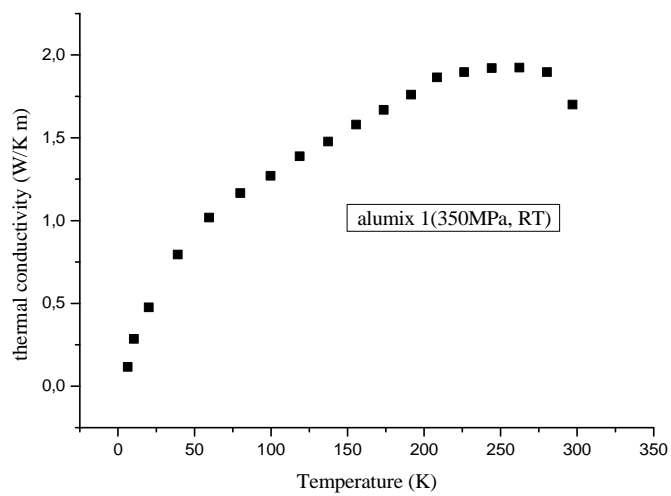


Figure 4.20. The Thermal Conductivity –Temperature graph of alumix(431) 1

4.6. Analysis of Seebeck Coefficient Results of Alumix(431) For 1, 2, 3, 4, 5, 6 Specimens

The Seebeck coefficient value is important physical property in reclaiming the potential performance of thermoelectric materials. The value is quite sensitive to the electronic structure and formulated by Mott's formula at a temperature T, for ordinary metals and semiconductors;

$$S(T) \propto T \left(\frac{\partial \ln \sigma(E)}{\partial E} \right)_{E_T = E_F} \quad (4.1)$$

Where σ_E is stated the electrical conductivity as a function of energy (Kuo, et al. 2012).

In alumix 1 sample, a change in transport feature is appeared as the sign and the magnitude of S(T) change rapidly, demonstrating charge carriers varies from n- to p-type in figure 4.19.

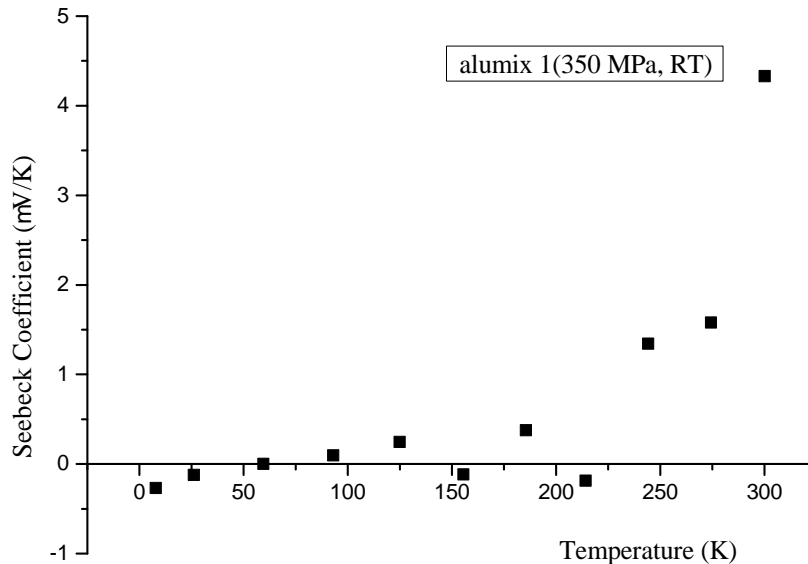


Figure 4.21. The Seebeck Coefficient –Temperature graph of alumix(431) 1

For alumix 1 (at various temperatures), alumix 2 (at 60K), alumix 3 (at 172K) alumix 6 (at 164.23 K), Seebeck coefficient values of the $0.09372 \mu\text{V/K}$, $0.0507 \mu\text{V/K}$, $0.00187 \mu\text{V/K}$, $0.0106 \mu\text{V/K}$ and respectively. Seebeck effect generated via both electrons and holes. Electrons and holes neutralize each other. The Fermi level can be offset from the lowest part of the pseudogap to a conduction band possessing a sharply increasing density of state (DOS) via electron doping in all the alumix 431 systems related on the rigid band model. After, the Seebeck coefficient increases as to Mott's equation. This equation proposes the Seebeck coefficient value is commensurate to the slope of the DOS at Fermi level. According to above equation, the negative effect of Seebeck coefficient is occurred via the increasing in the number of carriers, while the positive effect on the Seebeck coefficient is obtained from the increase in the slope of the DOS (figures 4.19-22) (Mikami et al., 2009).

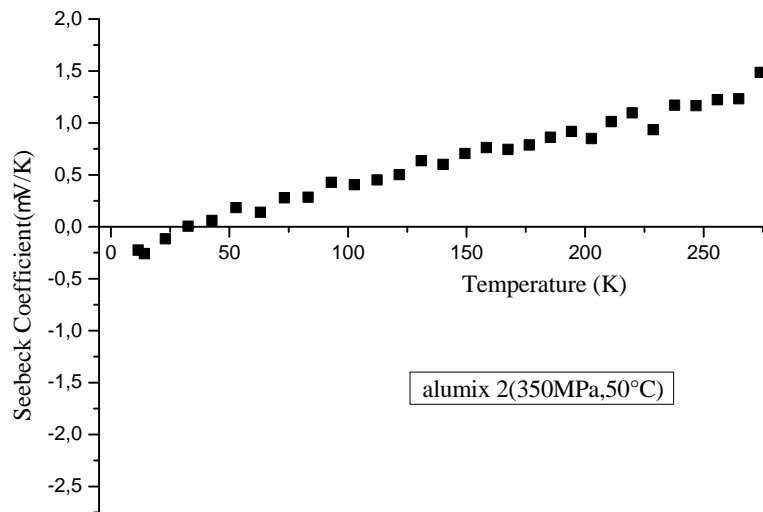


Figure 4.22. The Seebeck Coefficient –Temperature graph of alumix(431) 2

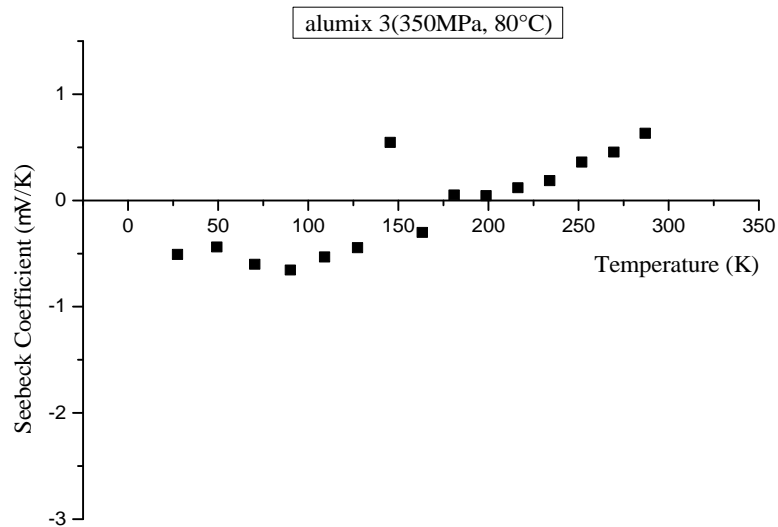


Figure 4.23. The Seebeck Coefficient –Temperature graph of alumix(431) 3

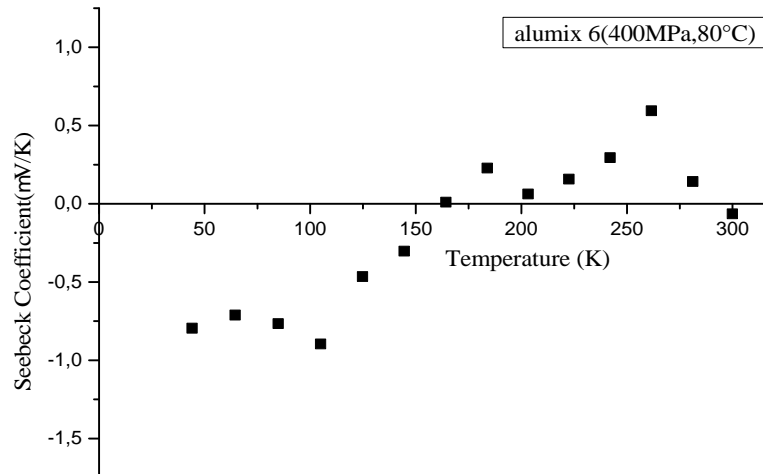


Figure 4.24. The Seebeck Coefficient –Temperature graph of alumix(431) 6

At alumix 3,4,6 specimens in figures 4.24, 4.27 and 4.28; a change of $S(T)$ sign says the existence of both positive (holes) and negative (electrons) types of carriers, this case show the multiband nature of the compounds. The positive contribution resulted from holes come from a powerful energy related to hole mobility, leading the positive TEP at higher temperatures. The figures exhibited that in the alumix systems, both the defects and dislocations increase. Also the extra scatter mechanism increases from both the impurity atoms and flaws and dislocations. This case induces to a increasing of the mean-free path of electron-hole pairs, and causes to positive effect on the TEP results (Özkurt et al., 2007).

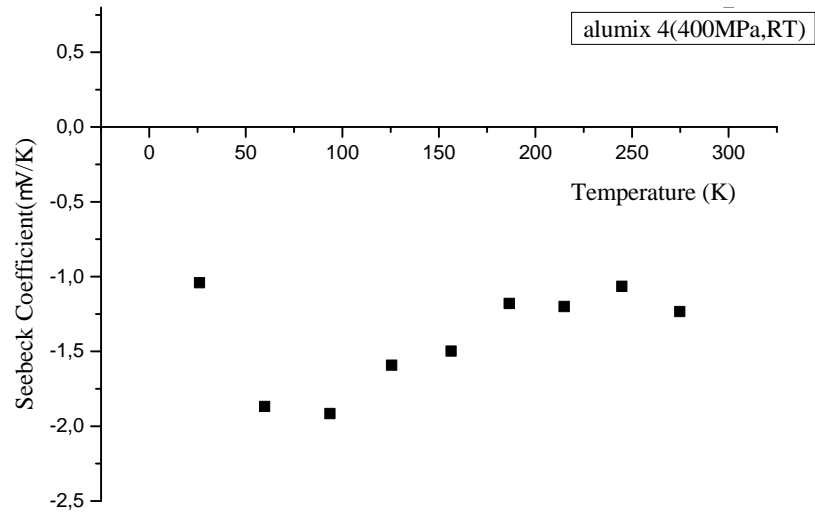


Figure 4.25. The Seebeck Coefficient –Temperature graph of alumix(431) 4

Alumix 4, 5, 6 samples, it is explained that around the Fermi level, the electronic band structure is qualified via a small coincide of alumix conduction band minimum, comprising electron carriers, with a valence band maximum increasing

For alumix 5 and 6 specimens, valleys, at 0-150K temperature range, is explained the larger influence in lowering and imperfection the transition properties (the valleys of Seebeck coefficients; for alumix 5 sample, is $-3.0657 \mu\text{V/K}$ at 90.82K, for alumix 6 sample, is $-0.895 \mu\text{V/K}$ at 105K; (Figure 4.22 and 4.24)

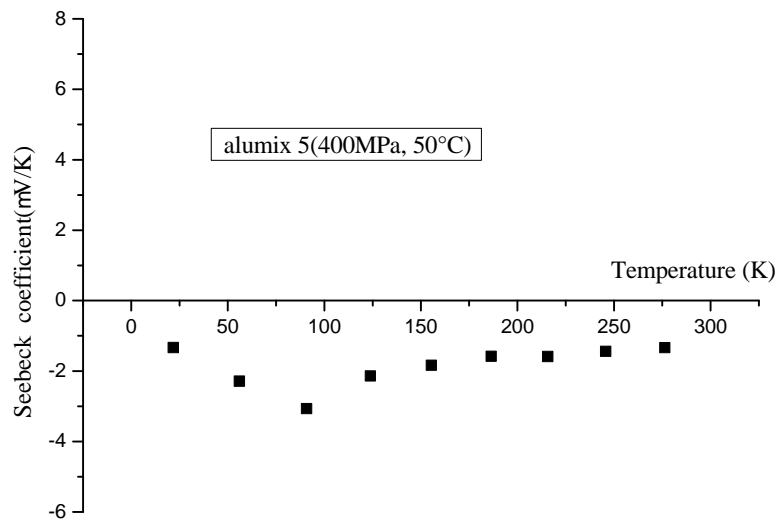


Figure 4.26. The Seebeck Coefficient –Temperature graph of alumix(431) 5

In alumix 6 sample graph exhibited as figure 4.20., Seebeck coefficient values of alumix 1 at temperature ranges between 150-200K and 200-300K are 0.228 $\mu\text{V/K}$ and 0.594 $\mu\text{V/K}$ respectively, for this reason, the samples show positive peak, at the same time it was observed that samples indicated the negative peak at 50-100 K temperature range. This case is explained through the Kondo Effect and crystal electric field, the second positive peak is showed the spin fluctuations on its ground state. As a known the Kondo effect is occurred to the appeared upturn the resistance at low temperatures (Kouwenhoven and Glazman,2001; Kuwai et al., 2006) .

In alumix 6 sample graph, the Seebeck coefficient sign indicates positive value at temperature from 50 K to room temperature due to the having the holes which are the major conductivity carriers. But, in alumix 2 and 5 samples, the sign of Seebeck coefficient shows negative value for measured temperature range. This case is also explained that the major conductivity carriers are electrons (Park et al.). Electrons are the prevailing charge carriers in alumix 2 and 5 samples, while holes the dominant charge carriers in alumix 6 specimen (Smontara et al.). Seebeck coefficient is increased, when the more acute spreading carriers as the temperature is increase. The negative peak compressed with increasing the heat treatment time. The decreasing of phonon heat current causes to a decrease in phonon-drag effect. This effect is electron transported momentum. Hence, the negative peak is referred to phonon-drag effect (Aksan and Yakıncı, 2007). And then, the Seebeck coefficient decreases because of a rapid increase in carrier concentration with the increasing of the temperature.

Higher Seebeck coefficient is succeeded in higher porosity specimen. On the Seebeck coefficient, the grain size possesses the effect. When the number of both impurities and point flaws within grains slant to increase through the decreasing of the grain boundaries, with the rising spreading of carriers resulted via impurities and flaws, Seebeck coefficient increase (He et al.2007).

As a result; at all alumix 431 samples (except sample 2) presents an increasing tendency with the measurement temperature range while alumix 2 sample exhibited in figure 4.20. showed the decreasing tendency with sintering temperature

of 250-300K. This case is resulted from the increasing of electron concentration because of anti-structural defects constitution.

4.7. Analysis of Figure of Merit Results of Alumix (431) For 1, 2, 3, 4, 5, 6 Specimens

The dimensionless figure of merit, ZT , sums up the thermoelectric properties. The value is an important factor in choosing materials for thermoelectric power generation. The dimensionless figure of merit is reckoned from the electrical conductivity, Seebeck coefficient and thermal conductivity measured.

All the ZT of alumix (431) specimens related to the thermal conductivity besides the power factor (Tani and Kido, 2008).

For alumix 1, 3, 5 sample graphs, the small values of ZT in such a manner that for alumix 3 sample, the value is 1.527×10^{-10} at 214K ; for alumix 4 samples the value is 3.803×10^{-8} at 21.8K; for alumix 6 sample, 2.121×10^{-10} at 63.4K, are resulted from very large thermopower, low thermal conductivity and very high the electrical resistivity. Also their carrier concentrations are optimized (figure 4.25-27) (Zhang et al.,2009; Søndergaard et al., 2013).

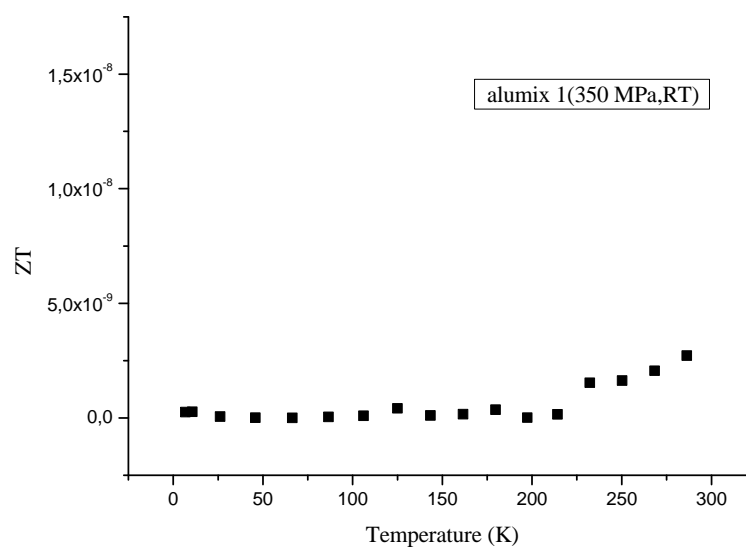


Figure 4.27. The ZT –Temperature graph of alumix(431) 3

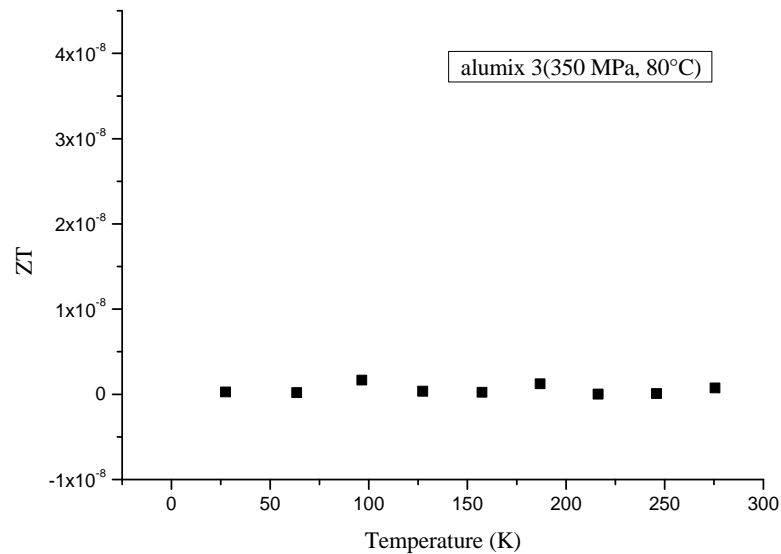


Figure 4.28. The ZT –Temperature graph of alumix(431) 3

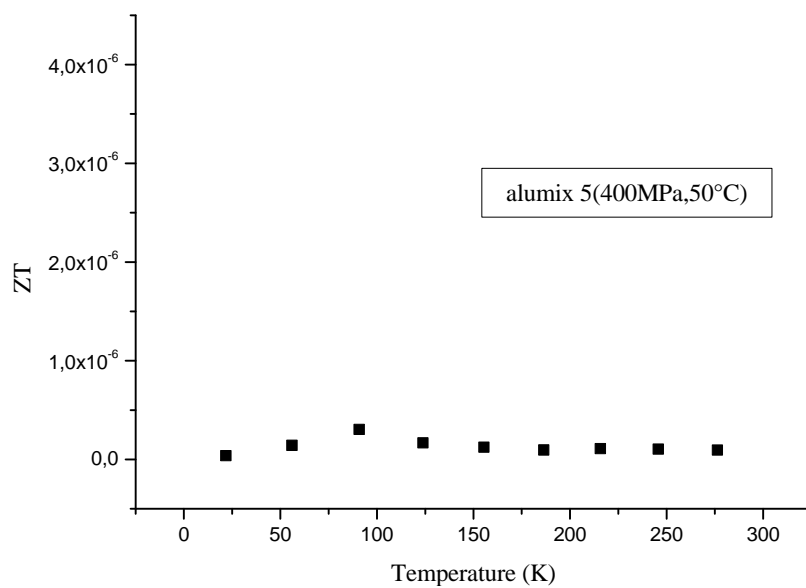


Figure 4.29. The ZT –Temperature graph of alumix(431) 3

In alumix 2 specimen graph (figure 4.28.); the enhancement of the thermoelectric features is commonly originated from improved phonon scattering, increasing of electrical conductivity and mostly its lower electrical resistivity (Wang et al.2011 and Ahmadpour et al. 2007). Lower thermal conductivity and much lower

Seebeck coefficient which is seriously defacer to ZT is observed in alumix 3 sample graph as shown in figure 4.26. (Carlini et al., 2014).

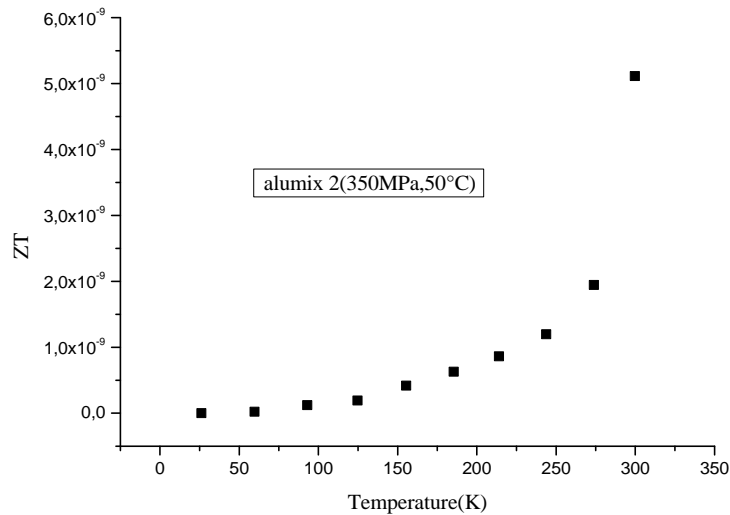


Figure 4.30. The ZT –Temperature graph of alumix(431) 2

In figures 4.30 and 4.31; for alumix 4 and 6 specimens, ZT decreases due to the increase of thermal conductivity and the highest ZT attains about 5.0×10^{-9} at 325 K by improvement of Seebeck coefficient (Han et al.). Samples show valleys at the temperature ranges 110-260K (for alumix 1) and 130-190K (for alumix 5) due to $\eta \rightarrow \eta'$ phase transition. Also, it is preponderated with various effects such as larger thermal conductivity, smaller Seebeck coefficient, though its electrical resistivity is improved. This enhancements in the thermoelectric properties of alumix 6 and 4 specimens, arise from the reduce in both the electrical resistivity and lattice thermal conductivity which can be attributed to the increased holes concentration and improved phonon scattering (Pan et al.2010).

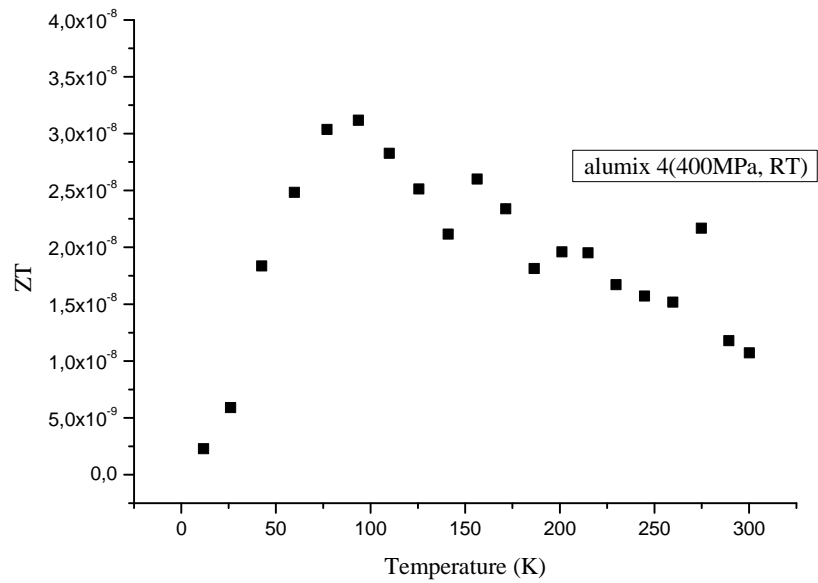


Figure 4.31. The ZT –Temperature graph of alumix(431) 4

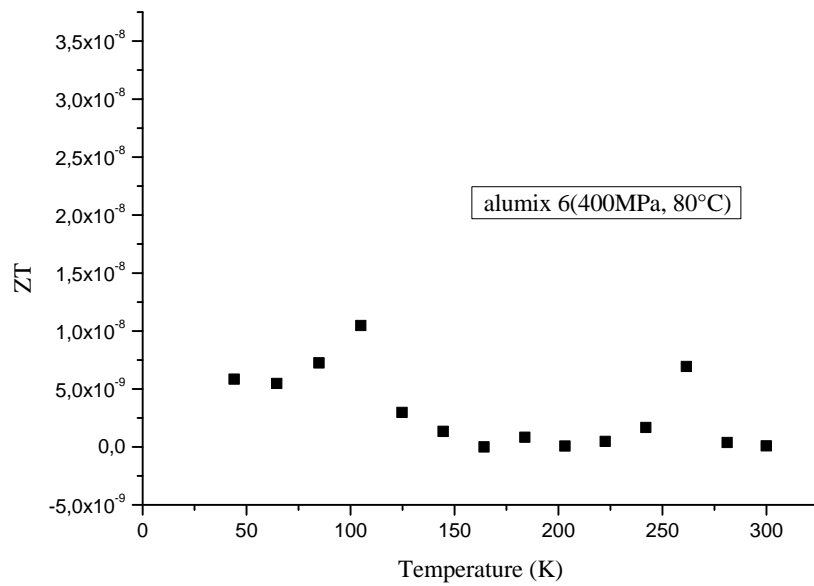


Figure 4.32. The ZT –Temperature graph of alumix(431) 6

5. CONCLUSION

Thermoelectric materials transform waste heat from industrial waste, automobile exhaust gases etc. to electricity energy using Seebeck effect. The effect is conversion of temperature changed directly and the devices worked with this effect are known as Seebeck generators. In the other words, the devices generate heat flow between coupling of two various types of material using Peltier effect. The devices occurring with the effect and applies to coolers, due to this reason the devices are referred the Peltier coolers.

A thermoelectric device consists of an element put between a heat source and heat sink. Heat transfer is occurred from the source to the sink via the carriers (or electrons) motion or lattices. The efficiency of thermoelectric devices is stated by dimensionless figure of merit (ZT) of thermoelectric materials. The figure of merit is determined calculating of electrical resistivity, thermal conductivity, Seebeck coefficient values.

A high quality thermoelectric material is necessitated for a high electrical conductivity, high thermopower and the low thermal conductivity, high ZT values these properties related to each other. In the Hall Effect, Seebeck coefficient and resistivity will be low so as to maximize ZT materials.

Thermoelectric materials are classified by the temperature rang of their implementation areas: Bi_2Te_3 alloys, PbTe based alloys and TAGS, SiGe alloys. The Fabrication Methods of the thermoelectric materials are; crystal growth methods, thin film methods, powder based methods.

In the previous study section, it reviewed the production methods of thermoelectric materials and the thermoelectric properties (electrical conductivity and resistivity) of Al7xxx materials. It wasn't studied about the Seebeck coefficient, figure of merit of Al 7xxx series alloys. In this study, it was investigated the thermoelectric properties with Seebeck coefficient and figure of merit of Alumix 431 material which is Al 7xxx alloy.

In this study Alumix 431 (Al-5.5Zn-2.5Mg-1.5Cu) prepared by conventional pres and sintering method on different pressure and temperatures. The structural

properties of Alumix 431 material was investigated on the light microscope(Leica DMRX) and SEM (LEO 1530 GEMINI) microscope images and density testing measurement was done by ARCHIMEDES Principle(water displacement technique Precisa 320XT series for analytical and precision balances in Gazi University's Mechanical Research Laboratory in Ankara, Turkey. The thermoelectric properties of Alumix 431 materials was measured by Model 6000 Physical Property Measured System at 5-300 K in İnönü University's Scientific and Technology Center in Malatya , Turkey.

The obtained experimental results show that at temperature range of 285-295 K, the maximum electrical resistivity and electrical conductivity were acquired 0.161Ωm(350 MPa, RT) (Alumix 1) and 24.96W/Km(400 MPa, 80°C) (Alumix 6), respectively, and the Seebeck Coefficient values changed mostly negative sign to positive sign due to dominate from carriers. Also, it was determined as 5.65×10^{-6} of the maximum figure of merit at 300K temperature(400MPa, RT)(Alumix 4).

REFERENCES

- BLACK J.T., KOHSER R.A., 2008, Degarmo's Materials And Processes In Manufacturing, Tenth Edition, John Wiley & Sons., Courier/Westford.
- RAMAKHRISNAN P., 1980., History of Powder Metallurgy, Indian Journal of History Of Science, 18(1): 109-114
- BHUIYAN M.H., KIM T.S., KOO J.M., HONG S.J., 2011. Microstructural Behavior of the Heat Treated n-type 95% Bi₂Te₃-5% Bi₂Se₃ gas Atomized Thermoelectric Powders. Journal of Alloys and Compounds, Vol. 509, 1722-1728.
- LIM C.H., KIM K.T., KIM Y.H., LEE Y.S., LEE C.H., CHO D.C., LEE C.H., 2006. Effect of Powder Mixing on Thermoelectric Properties in Bi₂Te₃ Based Sintered Compounds. Intermetallics, Vol. 14 (10-11), 1370-1374.
- YANG F., ZHAO J., AI X., YUAN X., 2009. Effect of Medium Temperature on the Dispersion of WC/ZrO₂/VC Composite Powders. Journal of Materials Processing Technology, Vol. 209, 2161-2166.
- XU B., LIU L., LIM H., QIAO Y., CHEN X., 2012. Harvesting Energy from Low-grade Heat Based on Nanofluids, Rapid Communication, Nano Energy 1, 805-811
- RUBI C.S., GOWTHAMAN S., RENGANATHAN N.G., 2014. Role of Nanostructured Materials in Recent Developments of Thermoelectric Nanocomposites, Depharma Chemica 6(1):7-13
- TRITT T.M., M.A. SUBRAMANIAN M.A., BÖTTNER H., CAILLAT T., CHEN G., FUNAHASHI R., JI X. KANATZIDIS M., KOUMOTO K., NOLAS G.S., POON J., RAO A.M., Thermoelectric Materials, Phenomena, and Applications: A Bird's Eye View, Mrs Bulletin, Volume 31
- SNYDER G. J., TOBERER E.S., 2008. Complex Thermoelectric Materials, nature materials vol.7
- RUOHO M., 2011. Nanostructured Thermoelectric Materials, MSc Thesis, Aalto University

- RADOUSKY H.B., LIANG H., 2012, Energy Harvesting: An Integrated View Of Materials, Devices And Applications, Nanotechnology 23 502001 (35pp)
- XIE M., GRUEN D.M., 2010, Potential Impact of $ZT = 4$ Thermoelectric Materials on Solar Thermal Energy Conversion Technologies, J. Phys. Chem. B 114: 14339–14342
- CALLISTER W.D., RETWISCH D.G., 2012, Fundamentals of Materials Science and Engineering an Integrated Approach, 4th ed. John Wiley & Sons, Inc
- KIM H.J., SKUZA J.R., PARK Y., KING G.C., CHOI S.H., NAGAVALLI A. 2012., System to Measure Thermal Conductivity and Seebeck Coefficient for Thermoelectrics, NASA/TM--217791
- DU C.-Y., WEN C.-D., 2011. Experimental Investigation and Numerical Analysis For One-Stage Thermoelectric Cooler Considering Thomson Effect, International Journal of Heat and Mass Transfer 54: 4875–4884
- WOOD C., 1988. Materials for Thermoelectric Energy Conversion, Rep. Prog. Phys. 51: 459-539.
- ZHENG J.C., 2008. Recent Advances on Thermoelectric Materials, Front. Phys. China, 3(3): 269-279
- DMITRIEV A.V., ZVYAGIN I.P., 2010. Current Trends in the Physics of Thermoelectric Materials, Physics- Uspekhi 53 (8) :789 ± 803.
- ALAM H., RAMAKRISHNA S., 2013, A Review on the Enhancement of Figure of Merit From Bulk to Nano Thermoelectric Materials, Nano Energy 2: 190-212
- FERGUS J.W., 2012. Review, Oxide Materials for High Temperature Thermoelectric Energy Conversion, Journal of the European Ceramic Society 32: 525–540
- TRITT T.M., 2002. Thermoelectric Materials: Principles, Structure, Properties, and Applications, Encyclopedia of Materials: Science and Technology, pp. 1–11,
- VINING C.B., 2009. An Inconvenient Truth About Thermoelectrics, Nature Materials, Vol. 8
- DUGHAISH Z.H., 2002. Lead Telluride as a Thermoelectric Material for Thermoelectric Power Generation, Physica B 322 : 205–223

- QUINTANA H.A., SONG E., WANG G.T., MARTINEZ J.A., 2013 Heat Transport in Novel Nanostructured Materials and Their Thermoelectric Applications, Chem Eng Process Tech 1: 1008:1-5
- HONEYWELL, Micro Switch Sensing and Control, Hall Effect Sensing And Application Catalog Brochure
URL: www.honeywell.com/sensing
- GRUBBS W.J. 1959.Hall Effect Devices, The Bell System Technical Journal, 853-876
- ROHM, Semiconductor, Applications for Hall Effect IC Switches in Portable Applications Hall Effect ICs in Portable Electronics, catalog Brochure
- VAN DER PAUW L.J, 1958. A Method of Measuring Specific Resistivity and Hall Effect Of Discs of Arbitrary Shape, Phillips res. Repts. 13, 1-9
- PAGAVA T.A., CHKHARTISHVILI L.S., Oscillatory Dependence Of Electron Hall Mobility On The Annealing Temperature For Irradiated Silicon, Ukr. J. Phys. 2004. V. 49, N 10
- WAGNER-REETZ M., CARDOSO-GIL R., PROTS Y., SCHNELLE W., GRIN Y., 2014. Thermoelectric Properties of Single- and Polycrystalline RuGa₃, Solid State Sciences 32:56-60,
- ZHU W., DENG Y.,WANG Y., LUO B., CAO L., 2014. Preferential Growth Transformation of Bi_{0.5}Sb_{1.5}Te₃ Films Induced by Facile Post-Annealing Process: Enhanced Thermoelectric Performance with Layered Structure, Thin Solid Films 556: 270–276
- ZHENG Z.-H., FAN P., LIU P.J., LUO J.-T., CAI X.-M., LIANG G.-X., ZHANG D.-P., YE F., LI Y.Z., LIN Q.-Y., 2014, Enhanced Thermoelectric Properties Of Mixed Zinc Antimonide Thin films Via Phase Optimization, Applied Surface Science 292: 823– 827
- LEE H.J., PARK H.S., HAN S., KIM J.Y., 2012. Thermoelectric Properties of n-type Bi–Te Thin Films with Deposition Conditions Using RF Magnetron Co-Sputtering. Thermochimica Acta, Vol. 542, 57-61.

- CASTRO M.V., CERQUEIRA M.F., REBOUTA L., ALPUIM P., GARCIA C.B., JÚNIOR G.L., TAVARES C.J., 2014. Influence of Hydrogen Plasma Thermal Treatment on the Properties of ZnO:Al Thin Films Prepared by DC Magnetron Sputtering, *Vacuum* 107: 145-154
- LU M.P., LIAO C.N., 2013. Mechanical and Thermal Processing Effects on Crystal Defects and Thermoelectric Transport Properties of Bi₂(Se,Te)₃ Compounds. *Journal of Alloys and Compounds*, Vol. 571, 178-182.
- LIM C.H., KIM K.T., KIM Y.H., LEE Y.S., LEE C.H., CHO D.C., LEE C.H., 2006. Effect of Powder Mixing on Thermoelectric Properties in Bi₂Te₃ Based Sintered Compounds. *Intermetallics*, Vol. 14 (10-11), 1370-1374.
- NAVRÁTIL J., STARÝ Z., PLECHÁČEK T., 1996. Thermoelectric Properties of p-type Antimony Bismuth Telluride Alloys Prepared by Cold Pressing. *Materials Research Bulletin*, Vol. 31, 1559-1566.
- UENO K., YAMAMOTO A., NOGUCHI T., INOUE T., SODEOKA S., OBARA H., 2005. Optimization of Hot-Press Conditions of Zn₄Sb₃ for High Thermoelectric Performance III. Effect of Starting Particle Size On Thermoelectric And Mechanical Properties, *Journal of Alloys and Compounds* 392: 295–299
- SHEN J.J., ZHANG S.N., YANG S.H., YIN Z.Z., ZHU T.J., ZHAO X.B., 2011. Thermoelectric and Thermomechanical Properties of the Hot Pressed Polycrystalline Bi_{0.5}Sb_{1.5}Te₃ alloys. *Journal of Alloys and Compounds*, Vol. 509, 161-164.
- SRIDHAR K., CHATTOPADHYAY K., 1998. Synthesis by Mechanical Alloying and Thermoelectric Properties of Cu₂Te. *Journal of Alloys and Compounds*, Vol. 264, 293-298.
- SCHILZ J., RIFFEL M., PIXIUS K., MEYER H.J., 1999. Synthesis of Thermoelectric Materials by Mechanical Alloying in Planetary Ball Mills. *Powder Technology*, Vol. 105, 149-154.
- LI J., TAN Q., LI J.F., 2013. Synthesis and Property Evaluation of CuFeS_{2-x} as Earth-Abundant and Environmentally-Friendly Thermoelectric Materials. *Journal of Alloys and Compounds*, Vol. 551, 143-149.

- SURYANARAYANA C., 2001. Mechanical Alloying and Milling. Progress in Materials Science, Vol. 46, 1-184.
- YANG J.Y., AIZAWA T., YAMAMOTO A., OHTA T., 2000. Thermoelectric Properties of n-type $(\text{Bi}_2\text{Se}_3)_x(\text{Bi}_2\text{Te}_3)_{1-x}$ Prepared by Bulk Mechanical Alloying and Hot Pressing. Journal of Alloys and Compounds, Vol. 312, 326-330.
- KATSUYAMA S., KISHIDA A., ITO M., 2006. Synthesis of $\text{Na}_x\text{Co}_2\text{O}_4$ by the Hydrothermal Hot-Pressing and its Thermoelectric Properties. Journal of Alloys and Compounds, Vol. 414, 215-220.
- CHEN X., LIU L., DONG Y., WANG L., CHEN L., JIANG W., 2012. Preparation of Nano-Sized Bi_2Te_3 Thermoelectric Material Powders by Cryogenic Grinding. Progress in Natural Science: Materials International, Vol. 22, 201-206.
- LIAO C. N., WU L.C., LEE J.S., 2010. Thermoelectric Properties of Bi–Sb–Te Materials Prepared by Electric Current Stressing. Journal of Alloys and Compounds, Vol. 490, 468-471.
- WANG Y., FAN H.J., 2011. $\text{Sr}_{1-x}\text{La}_x\text{TiO}_3$ Nanoparticles: Synthesis, Characterization and Enhanced Thermoelectric Response. Scripta Materialia, Vol. 65, 190-193.
- HAN Y., LV S., HAO C., DING F., ZHANG Y., 2012. Thermal Conductivity Enhancement of BN/silicone Composites Cured under Electric Field: Stacking of Shape, Thermal Conductivity, and Particle Packing Structure Anisotropies. Thermochimica Acta, Vol. 529, 68-73.
- KUO C.H., CHIEN H.S., HWANG C.S., CHOU Y.W., JENG M.S., YOSHIMURA M., 2011. Thermoelectric Properties of Fine-Grained PbTe Bulk Materials Fabricated by Cryomilling and Spark Plasma Sintering. Materials Transactions, Vol. 52, 795-801.
- ALLENO E., ZEHANI E., ROULEAU O., 2013. Metallurgical and Thermoelectric Properties in $\text{Co}_{1-x}\text{PdxSb}_3$ and $\text{Co}_{1-x}\text{NixSb}_3$ Revisited. Journal of Alloys and Compounds, Vol. 572, 43-48.

- FANG S.F., WANG M.P., SONG M., 2009. An Approach for the Aging Process Optimization of Al–Zn–Mg–Cu Series Alloys. *Materials and Design*, Vol. 30, 2460-2467.
- JIA Y., CAO F., NING Z., GUO S., MA P., SUN J., 2012. Influence of Second Phases on Mechanical Properties of Spray Deposited Al–Zn–Mg–Cu Alloy. *Materials and Design*, Vol. 40, 536-540.
- LIU Y., JIANG D., LI B., YANG W., HU J., 2014. Effect of Cooling Aging on Microstructure and Mechanical Properties of an Al–Zn–Mg–Cu Alloy. *Materials and Design*, Vol. 57, 79-86.
- DIXIT M., MISHRA R.S., SANKARAN K.K., 2008. Structure–Property Correlations in Al 7050 and Al 7055 high-Strength Aluminum Alloys. *Materials Science and Engineering: A*, Vol. 478, 163-172.
- KVERNELAND A., HANSEN V., THORKILDSEN G., LARSEN H.B. PATTISON P., LI X.Z., GJØNNES J., 2011. Transformations and Structures in the Al–Zn–Mg Alloy System: A Diffraction Study Using Synchrotron Radiation and Electron Precession. *Materials Science and Engineering: A*, Vol. 528, 880-887.
- STARINK M.J., LI X.M., 2003. A model for the Electrical Conductivity of Peak Aged and Over Aged Al-Zn-Mg-Cu Alloys. *Metallurgical and Materials Transactions A*, Vol. 34A, 899-911.
- ZHANG F.P., LU Q.M., ZHANG J.X., 2009. Synthesis and High Temperature Thermoelectric Properties of $Ba_xAg_yCa_{3-x-y}Co_4O_9$ Compounds. *Journal of Alloys and Compounds*, Vol. 484, 550-554.
- WATERLOO G., HANSEN V., GJONNES J., SKJERVOLD S.R., 2001. Effect of Predeformation and Preaging at Room Temperature in Al-Zn-Mg-(Cu, Zr) Alloys. *Material science and Engineering A*, Vol. 303, 226-233.
- ZHANG Y., B. MILKEREIT B., O. KESSLER O., C. SCHICK C., P.A. ROMETSCH P.A., 2014. Development of Continuous Cooling Precipitation Diagrams for Aluminium Alloys AA7150 and AA7020, *Journal of Alloys and Compounds* 584: 581–589.

- ZHAO D., ZUO M., LENG J., GENG H., 2013. Synthesis and Thermoelectric Properties of CoSb₃/WO₃ Thermoelectric Composites. *Intermetallics*, Vol. 40, 71-75.
- SHARMA C., DWIVEDI D.K., KUMAR P., 2013, Effect of Post Weld Heat Treatments on Microstructure and Mechanical Properties of Friction Stir Welded Joints of Al-Zn-Mg alloy AA7039, *Materials and Design* 43: 134-143,
- ZANDER J., SANDSTRÖM R., 2008. One Parameter Model for Strength Properties of Hardenable Aluminum alloys. *Materials and Design*, Vol. 29, 1540-1548.
- GUYOT P., COTTIGNIES L., 1996. Precipitation Kinetics, Mechanical Strength and Electrical Conductivity of AlZnMgCu Alloys. *Acta Materialia*, Vol. 44, 4161, 4167.
- SALAZAR-GUAPURICHE M.A., ZHAO Y.Y., PITMAN A., GREENE A., 2006. Correlation of Strength with Hardness and Electrical Conductivity for Aluminum Alloy 7010. *Materials Science Forum*, Vol. 519-521, 853-858.
- FENG C., LIU Z.Y., NING A.L., LIU Y.B., ZENG S.M., 2006. Retrogression and Re-Aging Treatment of Al-9.99%Zn-1.72%Cu-2.5%Mg-0.13%Zr Aluminum Alloy. *Transactions of Nonferrous Metals Society of China*, Vol. 16, 1163-1170.
- LI Z., XIONG B., ZHANG Y., ZHU B., WANG F., LIU H., 2009. Investigation on Strength, Toughness and Microstructure of an Al-Zn-Mg-Cu Alloy Pre-Stretched Thick Plates in Various Ageing Tempers. *Journal of Materials Processing Technology*, Vol. 209, 2021-2027.
- ZAID H.R., HATAB A.M., IBRAHIM A.M.A., 2011. Properties Enhancement of Al-Zn-Mg Alloy by Retrogression and Re-Aging Heat Treatment. *J. Min. Metall. Sect. B-Metall.*, Vol. 47 (1) B, 31-35.
- ZANG J-XIN, ZHANG K., RAI S-IONG, 2012. Precipitation behavior and properties of a new high strength Al-Zn-Mg-Cu alloy. *Transactions of Nonferrous Metals Society of China*, Vol. 22, 2638-2644.

- LIU D., XIONG B., BIAN F., LI Z., LI X., ZHANG Y., WANG F., LIU H., 2014. In Situ Studies of Microstructure Evolution and Properties of an Al-7.5Zn-1.7Mg-1.4Cu-0.12Zr Alloy during Retrogression and Reaging. *Materials and Design*, Vol. 56, 1020-1024.
- GAOSONG W., ZHIHAO Z., QIANG G., JIANZHONG C., 2014. Effect of Homogenizing Treatment on Microstructure and Conductivity Of 7075 Aluminum Alloy Prepared by Low Frequency Electromagnetic Casting. *Research and development*, Vol. 11, 39-45.
- FERRAGUT R., SOMOZA A., TOLLEY A., 1999. Microstructural Evolution of 7012 Alloy during the Early Stages of Artificial Ageing. *Acta Materialia*, Vol. 47 No. 17, 4355-4364.
- FERRAGUT R., SOMOZA A., TORRIANI I., 2002. Pre-Precipitation Study in the 7012 Al-Zn-Mg-Cu Alloy by Electrical Resistivity. *Materials Science and Engineering: A*, Vol. 334, 1-5.
- ARCHAMBAULT P., GODARD D., 2000. High Temperature Precipitation Kinetics and ttt Curve of a 7xxx Alloy by In-Situ Electrical Resistivity Measurements and Differential Calorimetry. *Scripta Materialia*, Vol. 42, 675-680.
- DELLAH M., BOURNANE M., RAGAB KH.A., SADAOUY Y., SIRENKO A.F., 2013. Early Decomposition of Supersaturated Solid Solutions of Al-Zn-Mg Casting Alloys. *Materials and Design*, Vol. 50, 606-612.
- EKŞİ A., VELTL G., PETZOLDT F., LIPP K., SONSINO C.M., 2004, Tensile and Fatigue properties of Cold and Warm compacted Alumix 431 alloy, *Powder Metallurgy*, 200A, Vol.47 No.1
- FENG W., BAIQING X., YONGAN Z., HONGWEI L., XIAOQING H., 2009, Microstructural Development of Spray-deposited Al-Zn-Mg-Cu Alloy During Subsequent Porosity, *Journal of Alloys and Compounds* 477:, 616-621
- XUE W., WANG C., TIAN H., LAI Y., 2007, Corrosion Behaviours and Galvanic Studies of Microscopic Oxidation Films on Al-Zn-Mg-Cu Alloy, *Surface and Coatings Technology* 201: 8695-8701

- MOLA R. 2013, Fabrication and Microstructural Characterization of Al/Zn-Enriched Layers on Pure Magnesium, *Materials Characterization* 78, 121-128
- İYENEN O., 2009. The Influence Of Sintering And Shot Peening Processes On Alumix 431 Powder Materials, Master Thesis, Çukurova University
- DİLEK M., 2006. Mechanical Properties Of Different Aluminum Alloys Joined By Friction Stir Welding, Master Thesis, Çukurova University
- MUKHOPADHYAY S.M., 2013, Sample Preparation for Microscopic and Spectroscopic Characterization of Solid Surfaces and Films, (Sample Preparation in Analytical Chemistry, Mitra S., Mukhopadhyay S.M., , DOI: 10.1002/1047)
- GAFNER A., 2006, Construction of NMR equipment to be used in the Physical Properties Measurement System
- Physical Property Measurement System, Thermal Transport Option User's Manual, October 2002, Quantum Design, Part Number 1684-10013
- HAI-GEN J., FENG J., KANG W., LONG J., HON-FENG H., LI LI W., 2009, Fatigue Fracture of High-Strength Al-Zn-Mg-Cu Alloy, *Trans. Nonferrous Mat. Soc. China* 19, 1031-1036
- MAZZER E.M., AFONSO C.R.M., GALANO M., KIMINAMI C.S., BOLFARINI C., 2013, Microstructure Evolution and Mechanical Properties of Al-Zn-Mg-Cu Alloy Reprocessed by Spray-Forming and Heat Treated at Peak Aged Condition, *Journal of Alloys and Compounds* 579: 169-173
- ROUT P. K., GHOSH M. M., GHOSH K.S., 2014, Effect of Solution Ph on Electrochemical and Stress Corrosion Cracking Behaviour of a 7150 Al-Zn-Mg-Cu Alloy, *Materials Science and Engineering A604*: 156-165
- AKSAN M.A., ALTIN S., BALCI Y., YAKINCI M.E., 2007, Structural Characterization and Transport Properties of the HT_c $Bi_2Sr_2(Ca,Cd)Cu_2O_{8+\delta}$ Glass-Ceramic Rods, *Materials Chemistry and Physics* 106: 428-436
- AKSAN M.A., GÜLDESTE A., BALCI Y., YAKINCI M.E., 2006. Degradation of Superconducting Properties in MgB_2 by Cu addition, *Solid State Communications* 137: 320-325

- SMONTARA A., SMILJANIĆ I., A. BILU ŠIĆ A., JAGLIČIĆ Z., KLANJŠEK M., ROITSCH S., DOLINŠEK J., FEUERBACHER M., 2007. Electrical, Magnetic, Thermal And Thermoelectric Properties Of The “Bergman Phase” $Mg_{32}(Al,Zn)_{49}$ Complex Metallic Alloy, *Journal of Alloys and Compounds* 430: 29–38
- CARLINI R., MARRÉ D., PALLECHI I., RICCIARDI R., ZANICHI G., 2014, Thermoelectric Properties of Zn_4Sb_3 Intermetallic Compound doped with Aluminum and Silver Intermetallics 45: 60-64
- TSUJII N., , ROUDEBUSH J.H., ZEVALKINK A., COX-UVAROV C.A., G. SNYDER J., KAUZLARICH S.M., 2011. Phase Stability and Chemical Composition Dependence of the Thermoelectric Properties of the type-I Clathrate $Ba_8Al_xSi_{46-x}$ ($8 \leq x \leq 15$), *Journal of Solid State Chemistry* 184: 1293–1303
- GORMANI M.A., RAZA S.M.,* FAROOQUI N., M. ASHFAQ AHMED M.A., 1995, On Thermally Activated Electrical Resistivity In Metallic Glasses, *Solid State Communications*, Vol. 95, No. 5., pp 329-333
- SUZUKI R.O., KYANO T., 2004, Thermoelectric Properties of Fe_2TiAl Heusler Alloys, *Journal of Alloys and Compounds* 377: 38-42
- HE Z., PLATZEK D., STIEWE C., CHEN H., KARPINSKI G., MÜLLER E., 2007, Thermoelectric properties of hot-pressed Al- and Co-doped iron disilicide materials, *Journal of Alloys and Compounds* 438: 303–309
- MIKAMI M., TANAKA S., KABAYASHI K., 2009, Thermoelectric properties of Sb-doped Heusler Fe_2VAl Alloy, *Journal of Alloys and Compounds* 484: 444-448
- PAN L., QIN X.Y., XIN H.X., SONG C.J., WANG Q.Q., SUN J.H., SUN R.R., 2010, Effect of Silicon Condition on Thermoelectric Properties of Bulk Zn_4Sb_3 at Low Temperatures, *Solid State Science* 12: 1511-1515
- KUO Y.K., LUE C. S., HSU G., HUANG J.Y. HSIEH H. L., 2012, Investigation of Al Substitution on the Thermoelectric of $SrSi_2$, *Materials Chemistry And Physics* 137: 604-607

- ÖZKURT B., ÖZÇELİK B., KIYMAÇ K., AKSAN M.A., YAKINCI M.E., 2007, Thermoelectric Power and Thermal Conduction Studies On the Nd Substituted BPSCO(2234) Superconductors, *Physica C.*, 467:112-119
- AKSAN M.A., KIZILASLAN O., AKSAN E.N., YAKINCI M.E., 2012, Thermoelectric Power and Thermal Conductivity Study of the $Y_3Ba_5Cu_8O_x$ System, *Physica B*407: 2820-2824
- KOWENHOVEN L., GLAZMAN L., 2001. Revival Of The Kondo Effect, *Physical World*, 33-38
- KUWAI T., SUN P., SUGIHARA T., SUZUKI H., TAKEUSHI M., MIZUSHIMA T., MITSUDA A., ISIKAWA Y., FUKUHARA T., 2006. Thermoelectric Properties of $Ce(Ni, Pd)_2Ge_2$ at Low Temperatures below 1K , *Physica B*378-380: 146-147
- PARK K., YO K.Y., SEONG J.K., NAHM S., 2007, Microstructure and High-Temperature Thermoelectric Properties of Polycrystalline $CuAl_{1-x}Mg_xO_2$ Ceramics, *Journal of European Ceramic Society* 27, 3735-3738
- AKSAN M.A., YAKINCI M.E., 2007, Effect of Mo substitution on the Structural and Transport Properties of $Bi_2Sr_2Ca_2Cu_{3-x}Mo_xO_{10+y}$ System, *Journal of Alloys and Compounds* 433: 22-32
- TANI J.-I., KIDO H., 2008, Thermoelectric Properties of Al-doped $Mg_2Si_{1-x}Sn_x(x \leq 0.1)$ *Journal of Alloys and Compounds* 466: 335-340
- ZHANG K.X., QIN X.Y., XIN H.X., LI H.J., ZHANG J., 2009, Transport and Thermoelectric Properties Of Nanocrystal Substitutional Semiconductor Alloys ($Mg_{1-x}Cd_x$) $_3Sb_2$ Doped With Ag, *Journal of Alloys and Compounds* 484: 498-504
- SØNDERGAARD M., BØJESEN E. D., BORUP K. A., CHRISTENSEN S., CHRISTENSEN M., IVERSEN B.B., 2013. Sintering and Annealing Effects on ZnO Microstructure and Thermoelectric Properties, *Acta Materialia* 61 (2013) 3314–3323
- WANG Y., FAN H.J., 2011. $Sr_{1-x}La_xTiO_3$ Nanoparticles: Synthesis, Characterization and Enhanced Thermoelectric Response. *Scripta Materialia*, Vol. 65, 190-193.

AHMADPOUR F., KOLODIAZHNYI T., MOZHARIVSKYIJ Y., 2007, Structural and Physical Properties of $\text{Mg}_{3-x}\text{Zn}_x\text{Sb}_2$ ($x=0-1,3,4$), Journal of Solid State Chemistry, 180: 2420-2428

CIRRICULUM VITAE

Ayşe Nur Acar was born on April 01, 1986 in Emet, Kütahya, Turkey. In 2003, she graduated from Kılıçarslan High School, and enrolled in Ceramic Engineering Department of Dumlupınar University. In 2009, she graduated with a Bachelor of Science degree in ceramic engineering from the Department of Ceramic Engineering. She also completed the undergraduate program of Mechanical Engineering with double major in the 2011. She began her MSc education at the Department of Mechanical Engineering of Çukurova University in 2011. She has worked as a research assistant since August 2011.